FOCUSSED MICROWAVE HEATING USING DEGENERATE AND NON-DEGENERATE CAVITY MODES

Mr Keith Ian Sinclair *MPhil, BEng*

Submitted for the degree of Doctor of Philosophy

Heriot-Watt University
School of Engineering and Physical Sciences

May 2009

Abstract

Microwave ovens have long been recognised as a means of reducing heating times versus conventional convection ovens. The principle design feature is based on the procurement of uniform heating within any material placed in the interior of the microwave cavity oven. Materials within the oven are subjected to a degree of heating dependent on their electromagnetic properties. For many applications, it is desirable to maintain control over the distribution of heat deposition. This can be achieved through focussing of the electromagnetic field within the cavity. Two new mechanisms are identified where an increased level of control over the heating pattern and its location could be advantageous.

The research described within this thesis aims to improve heating selectivity in microwave cavity ovens by the identification and enhanced control of modal patterns in degenerate and non-degenerate resonators. This is achieved through the analysis of two novel oven arrangements. The first of these addresses the requirement for highly selective heating in hyperthermia treatment. It is demonstrated that proper selection of a forced degenerate mode set can lead to an enhancement in field focussing within the centre of the cavity through constructive and destructive interference of the fields in each mode pattern. It is found that a highly selective peak of field can be produced within the centre of a large cylindrical waveguide cavity for the purpose of hyperthermia treatment. The peak is produced using a quasi degenerate mode set excited at approximately 1.3GHz.

The second example presents an open oven design for the curing of epoxy and encapsulant materials within the micro-electronics packaging industry. It is intended that the oven be placed on the arm of a precision alignment machine such that the curing and placement stages of production be combined, suggesting an increase in production efficiency. Two excitation schemes are presented based on the coupling of quasi degenerate mode sets through a wide frequency range and the excitation of a single high order mode enabling uniform field distribution for heating of encapsulant material and increased selective heating through spatial alignment of modal field peaks, respectively.

Experimental results demonstrate the viability of the open-ended microwave oven for curing. Both proposed excitation methods within the open oven design are investigated with results presented. Optimisation of the heating fields is achieved through inclusion of low-loss materials within the oven. Curing of an encapsulant material covering a commercial chip package is achieved and the overall design validated.

Acknowledgement

I would like to thank Professor Alan Sangster for his help, guidance and patience during the construction of this thesis. He has been a significant source of encouragement and advice during the course of my research activities.

I would like to express my appreciation to my colleagues, Professor Jiasheng Hong and Dr. George Goussetis, for their assistance and encouragement. I would also like to acknowledge my research colleagues from the University of Greenwich who have contributed to the modelling of the FAMOBS applicator and the dissemination of many of the findings.

A large number of models have been fabricated by the workshop technicians at Heriot-Watt University. I am grateful for their time and effort.

I would like to thank the Engineering and Physical Sciences Research Council (EPSRC) through the Innovative *electronics* Manufacturing Research Centre (IeMRC) for funding the main body of research. My gratitude goes to Professor Marc Desmulliez for employing me as a Research Associate at Heriot-Watt University. His knowledge of Polymer Curing and Micro-Engineering has been the main catalyst for the bulk of this work.

Finally, my sincerest appreciation goes to my family for their continued support throughout my research career. I would like to give a special mention to my wife, Emily, for her unwavering encouragement and patience.

Declaration

ACADEMIC REGISTRY
Research Thesis Submission

Name*:*	Keith Ian Sinclair		
School/PGI:	Engineering and Physical Sciences		
Version: *(i.e. First, Resubmission, Final)*	FINAL	Degree Sought (Award and Subject area)	PhD Microwave Heating

Declaration

In accordance with the appropriate regulations I hereby submit my thesis and I declare that:

1) the thesis embodies the results of my own work and has been composed by myself
2) where appropriate, I have made acknowledgement of the work of others and have made reference to work carried out in collaboration with other persons
3) the thesis is the correct version of the thesis for submission and is the same version as any electronic versions submitted*.
4) my thesis for the award referred to, deposited in the Heriot-Watt University Library, should be made available for loan or photocopying and be available via the Institutional Repository, subject to such conditions as the Librarian may require
5) I understand that as a student of the University I am required to abide by the Regulations of the University and to conform to its discipline.

* *Please note that it is the responsibility of the candidate to ensure that the correct version of the thesis is submitted.*

Signature of Candidate*:*		Date:	

Submission

Submitted By *(name in capitals):*	KEITH IAN SINCLAIR
Signature of Individual Submitting:	
Date Submitted:	

For Completion in Academic Registry

Received in the Academic Registry by *(name in capitals):*			
Method of Submission *(Handed in to Academic Registry; posted through internal/external mail):*			
*E-thesis Submitted (**mandatory from November 2008**)*			
Signature:		Date:	

Table of Contents

List of Figures

List of Tables

CHAPTER ONE

INTRODUCTION

1.1 Overview

This thesis presents two novel applicators for microwave heating of lossy materials within waveguide cavities. The principle design element is based on the use of degenerate, quasi degenerate and non-degenerate modes for the control and manipulation of the electromagnetic field patterns within the cavity interior. The analysis is placed in the context of microwave heating for hyperthermia and electronics packaging applications.

1.1.1 Multi-Mode Degenerate Mode Heating

Current cancer treatments involve the removal or extermination of malignant cells while leaving surrounding healthy cells undamaged. The relative success or failure of the treatments are based on the ratio of the number of malignant cells removed to the amount of healthy tissue left undamaged. A number of treatment regimes are currently prescribed for the treatment of malignant cells. Surgery involves the physical removal of cancerous cells from the body using surgical techniques. The downside to this method of treatment is that the healthy tissue or organs cannot be removed from the body. A further complication may involve the location of the malignant cells. Radiation treatment involves exposing the body to lethal doses of X-ray radiation. Anti-cancer drugs act by killing the malignant cells. Localised hyperthermia (as opposed to focussed hyperthermia) involves the heating of malignant cells using microwave frequency emissions. The emissions have low enough photon energy such that ionisation does not occur. Radiation, anti-cancer drugs and localised hyperthermia treatments are all severely limited by the response of the healthy tissue surrounding the malignant cells. Phased array technology, originally intended for radar jamming during the Cold War, could be adapted to provide a means of

focusing microwave energy into cancer cells within the human body [2].

Microwave hyperthermia is a therapeutic procedure in which the temperature of cancerous tumours embedded in healthy tissue is elevated above $42°$C [3] using microwave energy. For efficient hyperthermia treatment, maximum power density should be delivered to the target area (where the tumour is located) with minimal heating within the surrounding healthy tissue. This treatment effect can be achieved through using an antenna array [4]. A useful characteristic of hyperthermia treatment is that tumours have higher water content (they comprise approximately 80% water) than healthy tissue (which contains approximately 20% - 60% water). This allows tumours to absorb more microwave energy than the surrounding healthy tissue, which causes increased heating in the tumour.

The treatment of illness through increased temperatures is hardly a new phenomenon and dates back as far as the Ancient Greeks and Romans. They were primarily interested with the increased temperatures associated with fevers and the connection between the fever and healing. Towards the turn of the 19^{th} century many physicians noticed the beneficial properties of hyperthermia treatments [5]. In 1898, Westermark placed a cistern filled with circulating hot water into advanced carcinomas of the uterus and found shedding of some tumours. In 1910, Keating-Hart and Doyen introduced electrocoagulation of tumours.

While hyperthermia treatments themselves cause killing of malignant cells, perhaps the most attractive feature of this type of treatment comes when it is combined with radiation therapy. Combining both treatments enhances the effectiveness of X-ray radiation treatment. Hahn [6] suggested the cytotoxicity of X-rays increased when the malignant cells were exposed to increased temperatures before and after radiation treatment. Hahn concluded that a 30% lower X-ray dose could procure a given degree of cancer eradication when heat is used in conjunction with normal X-ray radiation.

The antenna (more commonly known as an applicator) may be invasive or non-invasive. A limiting factor in the use of microwave energy in the treatment of tumours is due to the complex physical properties of the tissue within the human body. The electromagnetic field cannot penetrate deep inside of the body if the frequency is too high. If the frequency is too low then the focusing ability deteriorates. In addition, as the human body is a complex heterogeneous medium, the electric field is subject to many different complex dielectric changes that cannot be determined accurately. Instead, each material (e.g.

muscle, fat, bone, skin) must be approximated so that homogenous models can be created in order to predict heating behaviour which, in turn, suggests a decrease in overall accuracy. If the decrease in accuracy of the predicated pattern is represented by a decrease in the selectivity of the focussed field pattern, then the source power must be increased in order to maintain similar field magnitudes as to the *ideal* distribution. An increase in source power coupled with a decrease in field pattern selectivity has the obvious effect of increasing the absorbed power within healthy areas where heating should be minimised.

Instead of using antenna array type applicators (where high selectivity requires large impractical arrays if a penetrative frequency were to be used), it is proposed that a high order degenerate mode waveguide cavity be utilised where a combination of modes excite a 'localised hot-spot' of electromagnetic energy. This type of applicator may provide a means of bypassing the field penetration problem associated with high frequency electromagnetic waves directed at biological tissue. Instead of using a propagating electromagnetic wave from an array antenna, a standing wave within waveguide cavity is utilised allowing for volumetric heating.

Through using the principle of wave interference, it is proposed that a cavity be constructed where a known number of modes are excited at a single frequency such that the electromagnetic field distribution describes a sharp peak of field within the centre of the volume. It is within this field peak that the tumour or cancerous cells will be aligned. The mode set consists of resonances that are degenerate or can be forced into degeneracy through appropriate levels of tuning. Any requirement for multiple sources to couple multiple modes at different frequencies is removed.

1.1.2 Quasi Degenerate Mode Heating

Currently the vast majority of adhesive materials used in electronic product assembly and packaging are bonded using infra-red, UV-curing or convection heating. These conventional thermal processing steps (especially convection heating) can take up to several hours to perform and result in slow throughput and an increased cost of packaging. They are also inadequate for devices and materials that require a low thermal power budget like organic light emitting polymers diodes (OLEDs). With the demand for lighter, faster, and smaller electronic devices, there is a need for innovative material processing techniques to reduce the cost of packaging. One such technique is variable frequency microwave (VFM) curing, which can perform in minutes some of the same functions as conventional

thermal processing [7]. Conventional VFM technology uses a closed oven cavity and, as such, does not incorporate an in-situ alignment bonding capability during curing. If such a technology were to be placed on the arm of a high precision alignment machine, further costs savings could be achieved by allowing for the simultaneous placement and curing of the components during assembly as suggested in Figure 1 [7].

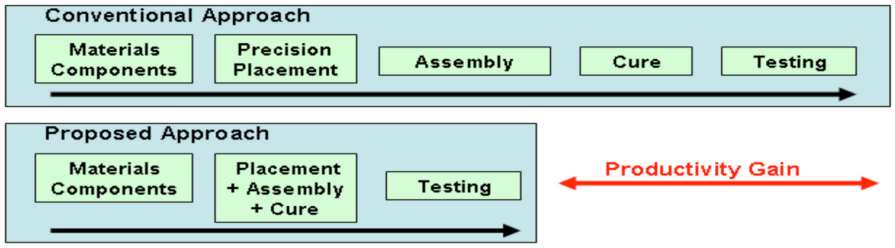

Figure 1: Influence of the proposed open cavity oven at the assembly stage.

As of late 2008, the market opportunities for the exploitation of such a technology were potentially very large in both microelectroncis assembly and disassembly production. The electronics industry in Europe is a major contributor to the economical strength of the European economy. Manufacture of high value added electrical machinery and apparatus in the *EU 25* is about 225 billion euro per year. Assembly based on conductive adhesives in microelectronics represent 15% of the 23 million wafers (200mm equivalent) in 2007. The open oven technology opens up 40% of this market in terms of wafer volume due to the lower reflow temperature offered by the proposed technology for lead-free solder. The proposed technology fits applications in the following sectors, 2005 revenue (billions of U. S. dollars) in brackets: micro-components (55.5), optical semi-conductors (15.9), sensor / actuator integrated circuits (2). It is well documented that the cost of packaging in microelectronics is around 30% of total production costs, but this is rising due to the increasing consumer demand for smaller and smarter portable electronic devices. In microsystems, the cost of packaging can be up to 80% of total production costs. Technological advances to reduce packaging costs are therefore of pivotal importance to maintain a competitive edge for assembly companies. By applying the open oven technology, it is estimated that packaging costs could be reduced by 20% and overall production time by 30%. These packaging costs are estimated at 140 million pounds per annum worldwide.

With the exodus of high volume packaging and assembly companies to low-wage countries such as China and India, the manufacturing industry in Europe needs to revitalise itself by encouraging design and innovation that will allow European companies to produce assembly equipment and materials of tomorrow that will feed into the Asian mar-

ket. The WEEE [8] and RoHS [9] directives are making many companies think carefully about product disassembly at the early design stage for recycling and also rework. This is a large and growing market.

VFM heating can reduce curing times by as much as ten to twenty times, as compared to conventional oven heating depending on the application [10]. This technology utilises a microwave source that varies rapidly in frequency (unlike a conventional microwave oven that operates at a fixed frequency of 2.45GHz) to irradiate materials under processing. VFM heating has two main advantages over conventional microwave heating. Rapid frequency sweeping through a wide bandwidth produces a uniform heating distribution through the oven chamber as a result of the heavy electromagnetic field overmoding. Also, the rapid sweeping of frequency (in the order of 100ms) reduces the likelihood of arcing, thus allowing microwave heating of metals and semiconductor without any damage. At high powers, arcing appears when excessive charge build up occurs at, for example, a sharp point on a high conductivity material. However, in VFM oven operation, the changing position of the electric field magnitude peaks [due to modal scintillation] does not allow significant charge build up over time reducing the possibility of arcing.

There are currently several limitations in conventional VFM processing, including: lack of reliable temperature measurement techniques, uncertain process characterisation methods, poor assessment of the required thermal budget, incomplete understanding of the interactions between microwaves and materials and a lack of control over the various physico-chemical processes occurring during bonding. Current VFM cure of polymer materials in electronic packaging also bulk heats the entire package or substrate. The deposition of heat is primarily controlled through the difference in the dielectric loss tangent of each material within the oven. Higher loss materials will encourage greater heat deposition for a given electric field. Moreover, VFM processing cannot be performed today simultaneously with fine placement or alignment of the die or wafer onto the board (Figure 1).

A novel applicator is proposed that achieves radio frequency (RF) curing of adhesives used in microelectronics, optoelectronics and medical devices through using a novel open cavity arrangement that permits simultaneous micron-alignment and bonding of devices with the option of using VFM technology. The open oven cavity can be fitted directly onto a flip-chip or wafer scale bonder. The invention therefore combines:

1. RF-curing of adhesives used in microelectronics,

2. MEMS, optoelectronics and medical devices packaging, especially for flip-chip, wafer-scale bonding and encapsulation,

3. simultaneous micron-alignment accuracy bonding of the devices onto wafer or PCBs,

4. an open ended over-moded dielectric filled waveguide cavity resonator, and

5. novel magnetic or impedance walls providing both closed cavity resonant mode field patterns within the dielectric filled portion of the oven and high field penetration into the open end (Chapter 6).

It is intended that the applicator be excited by either a swept source that encourages a highly overmoded cavity through excitation of many degenerate mode *sets*, or by a single high order non-degenerate mode. The selectivity of heat deposition can be increased if the electric field peaks of a modal pattern are spatially aligned with the bump on a chip package. Removing (or at least minimising) heat deposition within materials where no curing occurs will increase the reliability and life time of the package due to a decrease in mechanical stresses caused by the cooling process. On the other hand, the uniform field distribution produced by VFM excitation is ideal for the curing of encapsulant or underfill reflow.

1.2 Thesis Outline

Degenerate and non-degenerate mode heating is investigated through the analysis of two novel cavity geometries based on the hyperthermic heating of cancerous cells and the curing of epoxy and encapsulant materials within the micro-electronics manufacturing industry, respectively. A number of numerical models are created in order to analyse the electromagnetic field distribution within both cavities. Both the hyperthermic applicator and open-ended oven for curing can be excited at frequencies promoting coupling of very high order modes within the interior volume. It was found that current commercially available electromagnetic analysis software was limited in producing accurate solutions of the waveguide models due to the intensive computational demands placed upon the computer hardware. In order to investigate very high order models, it was concluded that a numerical solution be found based on the summation of modal fields.

The thesis begins by introducing a review of research literature within the area of focussed microwave heating and in particular the interaction of electromagnetic waves with biological tissue and polymer materials within the micro-electronics industry. The relationship between VFM excitation methods and the curing of electrically conductive adhesives (ECA's), non-conductive epoxies, underfill materials and encapsulants is investigated. The topic of hyperthermia treatment using microwaves is presented and a number of applicators described including current commercial phased array applicators. The measurement of the dielectric properties of epoxy resins versus temperature and frequency is described.

The electromagnetic theory used throughout the thesis is presented within Chapter 3. An outline is provided covering a historical summary of waveguide as a viable means of power transmission. The field relations within differing waveguide geometries and the associated propagation parameters are introduced. Quality Factor and its effect of modal degeneracy is discussed. Methods of coupling electromagnetic waves into waveguide cavities and cavity perturbation are highlighted.

Chapter 4 describes a proposed hyperthermia treatment applicator based on degenerate mode summation within an overmoded resonant waveguide cavity resonator. Through using the basic principle of constructive and destructive wave interference, it is proposed that a peak of electric field can be produced within the centre of a waveguide cavity through proper selection of a number of degenerate modes. This electric field peak would be used to selectively heat cancerous cells within the human body while minimising any heat deposition within healthy tissue (located within an electric field null). A hypothesis is presented outlining the functionality of the oven. A mode interference model is applied to both rectangular and cylindrical cavities.

An investigation into focussed microwave heating using the evanescent fringing fields of a high order mode within a waveguide cavity is presented within Chapter 5. A novel microwave oven design is described and is applied to the curing of polymer materials within electronic packaging technologies. The conditions for resonance within the geometry are presented and a plane wave analysis technique used to determine the optimum conditions for resonance of a high order mode. The dependance of the absorbed power within a sample to the evanescent fringing field within the heating region is described. Various design trade-offs are highlighted. Further analysis of the electromagnetic fields for two different excitation routines is investigated.

A design requirement found during the investigation of the novel oven design in Chapter 5 is the need to maximise the electromagnetic fringing fields within the heating region. Chapter 6 presents a means of optimising the electromagnetic fringing fields within the microwave oven through inclusion of low loss dielectric material. Adjustment of the length of the dielectric insert allows for control of the reflection phase at the heating region boundary. A figure of merit is introduced to allow for a comparison of various oven design permutations. An eigenmode solution for a lossless, multi-section oven design is utilised. An eigenmode solution provides a means of calculating the resonant frequency of each design variation. Furthermore, both a plane-wave analysis and transmission line analysis are used to calculate the reflection phase from the material boundary of interest. Finally, a full wave simulation is obtained in order to investigate the change in the dielectric power density within a lossy target sample placed within the heating region of both optimised and non-optimised cavities.

Chapter 7 introduces an experimental investigation into degenerate and non-degenerate mode heating within the novel microwave oven design presented within Chapter 5 and Chapter 6. Various excitation parameters are defined to support degenerate and non-degenerate mode heating. It is hypothesised that a single high order non-degenerate mode resonance will allow for electric field peak alignment with ECA bumps (for example) thus reduces unwanted heating within other regions of the package. Degenerate mode heating is introduced through a VFM excitation that maintains a heavily overmoded cavity. A closed loop feedback routine is implemented allowing the temperature within the test sample to be controlled. The optimisation of the heating fringing field, as suggested in Chapter 6, is experimentally validated for a non-degenerate excitation. A curing trial based on encapsulation of an op-amp package validates the proposed technology. The complex permittivity of an encapsulant paste is characterised versus frequency and temperature.

Chapter 8 delivers the conclusion of the thesis. In addition, areas of future research are described.

CHAPTER TWO

REVIEW OF LITERATURE

2.1 Introduction

This chapter contains a review of journal and conference papers that hold relevance to the content within this thesis and seeks to provide a description of previous work conducted within a number of research areas.

Focussed microwave heating is discussed in the context of electromagnetic field interaction with biological tissue and polymer materials. General medical considerations are highlighted with various cancer treatments discussed. Particular attention is given to the use of microwave radiation for the heating of cancerous cells. A design feature within hyperthermia applicators is that the electric field should maximise in the region of the body where the cancerous cells are located while minimising within surrounding healthy tissue. Curing of electrically conductive adhesives (ECA's), epoxy, encapsulant and underfill polymer materials using microwave energy is presented.

Focused heating mechanisms for hyperthermia treatment are discussed. A number of commercially available hyperthermia treatment devices are introduced based around phase array technology. Measurement of the complex permittivity of polymer materials is described. The dielectric complex properties vary with temperature, degree of cure and frequency. Finally, the perturbation of resonant modes within waveguide cavities is presented.

2.2 Focussed Electromagnetic Wave Heating

2.2.1 Medical Considerations

Electromagnetic radiation can be categorised as either ionising or non-ionising. Ionising radiation has enough photon energy to break atomic bonds within a material by removing one or more electrons and creating a charged atomic particle. Non-ionising radiation does not have enough photon energy to achieve this result. The behaviour of non-ionising electromagnetic fields within a biological medium can be classified as thermal and non-thermal (or athermal) [11].

Thermal effects arise directly from the absorption of electromagnetic power within a lossy medium. This is largely due to the motion of water particles and dissolved ions. Absorbed power within biological tissue occurs principally through the electric field component. Other factors that effect heat deposition are frequency, modulation characteristics and modulation frequency of the applied field [12]. According to De Salles [11], a large number of factors affect the amount of heat generated by an electric field within biological tissue. These include the thermoregulatory system, physiological conditions, environment and, under certain circumstances, vascularisation. (Vascularisation describes the bodys ability to remove heat through blood flow). The main risk of thermal damage in the body exists in the places where blood flow is at a minimum. An example being the lens of the eye. The lens is made from a protein similar to that found in the white of an egg. It goes white when the temperature is raised causing potentially harmful cataracts. This effect is of particular importance to a variety of hand-held antenna devices, where the antenna may be held in close proximity to the head. Non-thermal effects are not attributed to an increase in heat but to the interaction of the applied field at molecular level. Charged particles will seek to align themselves with the electric field potentially causing distortion of biological molecules and hence long term damage.

Non-thermal effects are still generally not well understood, but a number of reports exist describing such effects as changes in the nervous, immune and cardiovascular systems due to biochemical and electrophysical effects [11], [13]-[16]. Non-thermal effects are reported to occur at lower power levels than observable thermal effects.

An important area of consideration is the health risk posed by prolonged exposure to electromagnetic fields especially due to cellular phones and base stations. Much research

has taken place in an effort to describe appropriate (safe) exposure levels. Lin [17] states,

> "If a specified RF exposure produces a biological effect, the effect must be evaluated for its potential as a hazard to humans. The fact that a biological change is observed or suspected to occur in humans does not, by itself, indicate that the factor that produces the change is hazardous."

The fact that an organism responds to an external stimulus does not immediately mean damage is being done. In other words, the organism should be able to maintain some sort of equilibrium and return to the original state once the external stimulus is been withdrawn. However, if the stimulus is so strong as to affect that organism's ability to function then the "effect" can be said to be "hazardous" [17]. It is for this reason that many agencies publish guidelines or standards for electromagnetic exposure. These standards usually recommend different exposure levels based the type of environment in which the electromagnetic waves will predominantly radiate. "Controlled environments" describe places where the energy levels can be accurately measured and exposure time can be controlled (for example, a workplace). Personnel working within the area will have been expected to have been informed of the levels of radiation and, if need be, provided with the appropriate protective clothing. "Uncontrolled environments" describe places open to the public where it would be assumed that those within that area did not have prior knowledge of any increase in electromagnetic activity. These may include people of greater risk such as small children, pregnant women or cardio pacemaker wearers [11].

Several agencies have published standards describing appropriate radiation exposure levels. The most popular recommendations are the ANSI / IEEE [18] and the ICNIRP / CENELEC [19] guidelines. The guidelines in [18] and [19] are still only concerned with thermal effects and do not consider non-thermal effects.

Determining the electromagnetic field distribution within a human body exposed to radio waves from a focussed applicator is an extremely difficult task due to the complex properties of the various biological materials. Dielectric properties are inherently heterogeneous within a body but should be described as accurately as possible if the absorption and propagation of electromagnetic fields through the body are to be modelled with any degree of precision. This problem can be overcome by describing artificial tissues or phantom materials where regions of heterogeneous tissue are substituted for simplified homogeneous phantoms. It can be difficult to obtain realistic power distributions within phantom models of the human body and gelling agents are often used in order to act as a

more effective body substitute [20], [21].

Much has been reported on the characterisation of human biological materials at microwave frequencies [20]-[24]. Liu *et. al.* [22], described a technique for the precise measurement and characterisation of dielectric materials at higher frequencies. In [22], the recipes from Hartsgrove *et. al.* [23], were modified in order to obtain simulated materials over the frequency range of 5GHz to 20GHz. Previously Hartsgrove *et. al.*, had been successful in producing a phantom gelling agent which produced accurate results over a frequency range of 100MHz to 1000MHz. The gelling agent had been based on the components of muscle material; sodium chloride (NaCl), sucrose and water. Liu *et. al.*, used similar materials based on Hartsgrove *et. al.*, but varied the quantity of each ingredient such that performance was extended through the desired frequency range. They found that the concentration of sucrose was the determining factor in achieving proper phantom performance since the sucrose molecules have a significant effect on the water structure at higher frequencies. Also, the formulas used by Liu *et. al.*, were based on the dielectric properties of water.

A number of realistic human heterogeneous models have been developed and are used within computer simulations [24], [25]. Material characteristics are obtained from magnetic resonance imaging (MRI), computed tomography (CT) and anatomical images from both male and female cadavers. Data is stored in the form of voxels taken from each slice of the body. Each image slice consists of 256 x 256 pixel array. Each pixel consists of a 12 bit gray tone. The data is then processed by geometric transformations in order to match images of the body from the different image sources. Further more, thresholding algorithms are used to identify different tissues on the basis of voxel characteristics [26].

The HUGO anatomy model [27] is based on the information provided by The Visible Human Project of The National Library of Medicine. The male dataset consists of axial MRI images of the head and neck taken at 4mm intervals and longitudinal sections of the remainder of the body at 4mm intervals. The CT data consists of axial CT scans of the entire body taken at 1mm intervals at a resolution of 512 pixels by 512 pixels where each pixel is made up of 12 bits of grey tone. The axial anatomical images are 2048 pixels by 1216 pixels where each pixel is defined by 24 bits of colour. The anatomical cross-sections are also at 1mm intervals and coincide with the CT axial images. Gjonaj *et. al.* [26], used the HUGO model for the analysis of electromagnetic energy distribution in the human head due to high frequency mobile phone emissions and the electromagnetic

energy and temperature distribution for regional hyperthermia therapy. The induced specific absorption rate (SAR) within the human head was calculated for heterogeneous and homogeneous HUGO models. They concluded that the discrepancy in their result concerning the location of the temperature peak and average SAR values showed that a high resolution model was required in order to achieve accurate results.

An analysis of heat transfer through living tissue has been presented by Habash [28]. A one-dimensional bio-heat transfer equation was used to optimise a non-invasive hyperthermia treatment. It was concluded that the only method available for deep heating in the human body would be through focussing the energy at the region of interest due to high attenuation through muscle.

2.2.2 Microwave Curing of Polymer Materials

The investigation into microwave curing of epoxy and encapsulant resins is well documented. Early publications include investigations into the heating of epoxy resins using waveguides [29], [30] and multi-mode waveguide cavity ovens [31], [32]. Gourdenne [29] used a TE_{01} mode waveguide to study the effect of temperature versus time curing profiles for different net power flow intensities. Goudeene concluded that higher power gave faster polymerisation and steeper temperature gradients.

Karmazsin and Satre [30] also employed waveguide to investigate temperature versus time curing profiles for epoxy but for a pulsed input source. Wilson and Salerno [31] investigated two epoxy curing agents in a conventional microwave oven at a frequency of 2.45GHz and for differing power intensites. Their method allowed for comparisons to be made between the temperature versus time profiles of the two materials.

Strand [32] compared the curing temperature versus time profiles for epoxy resins heated within a convection oven and a conventional microwave oven operating at a fixed frequency. He found that rapid microwave heating initiated the quick increase in temperature slope at a lower temperature. Heat produced by the exothermic curing reaction significantly increased the temperature slope. Strand concluded that the cure time of epoxy was much less when heated by a microwave oven as compared to a convection oven. Strand also found that during microwave heating, the energy directly heated the polymer, whereas during thermal heating, the energy heated the substrate first before transferring heat into the polymer. It was shown that microwave curing provided a capability of ensur-

ing faster cure times and high efficiencies when compared to a conventional convection heating.

Variable frequency microwave (VFM) heating is an alternative method of curing epoxy materials. It has been reported that, in principle, VFM heating can reduce curing times by as much as 6 - 10 times (depending on the application) as compared to a convection oven [32]. VFM technology utilises a microwave source which varies rapidly in frequency (unlike a conventional microwave oven that operates at a fixed frequency of 2.45GHz) to irradiate materials under processing. VFM heating has two main advantages over conventional microwave oven heating [33]. Rapid frequency sweeping through a wide bandwidth produces a uniform energy distribution through the oven chamber as a result of the heavy overmoding. Sweeping the frequency (typically in the order of 100ms) reduces the likelihood of arcing thus allowing microwave heating of metals and semiconductor without any damage.

At high powers arcing will occur when excessive charge build up occurs, for example, at a sharp point on a high conductivity material placed within the volume of the cavity. However, in VFM oven operation, the changing position of the electric field magnitude peaks (due to modal scintillation) does not allow significant charge build up at a sharp point over time, thus avoiding arcing. The sweep bandwidth is determined by average frequency and cavity size [33].

Despite the aforementioned advantages, there are concerns that excessive build up of charge could cause electro-static discharge (ESD) damage to sensitive integrated circuits. Research has shown no significant difference in the post cure performance of CMOS logic chips having been irradiated by VFM heating system [34].

Materials with low dielectric loss characteristics remain at lower temperatures compared to high loss materials due to the selective nature of VFM energy absorption. Fundamentally, this characteristic reduces the thermal expansion mismatch between carrier and die allowing curing to be conducted in the presence of thermally sensitive components. As a consequence, it is possible to increase (or a least not decrease) the life time of the product before the lifetime starts [35].

Wei *et. al.* [36], demonstrated improved heating rates of chip-on-board (COB) glob top encapsulants using VFM technology while maintaining the same cure quality as com-

pared to convection heating methods. They reported that the VFM process / curing cycle was fifteen minutes less as compared to a two hour thermal cure cycle within a convection oven. No specific modification of the encapsulant was required in order to take advantage of the VFM curing process. VFM yield was equivalent when comparing cure, glass transition temperature T_g and coefficient of thermal expansion (CTE) properties. Wei *et. al.*, reported that the VFM curing process had no adverse effect of the functionality of the electronic components.

The microwave curing of silver filled epoxy adhesives [37], [38] has been characterised by focussing on the effect of the percentage of particles within an electrically conductive adhesive (ECA), the geometry and shape of the particles as well as the heating parameters of the VFM oven. Heating is characterised through a theoretical combination of microwave power absorption (due to the dielectric properties) and heat transfer equations. Wang *et. al.*, concluded that the heating rate is closely linked to the dielectric properties of the polymer. An increased heating rate does not directly transfer to an increased curing reaction rate. The relationship is not only a function of absorbed power, but also the properties of the curing agent within the polymer. Wang *et. al.*, identified a combination of a lower cross-linking reaction temperature and a high reaction speed would be a suitable choice. Small metal fillers were more beneficial than larger particles for improving the heating rate. Conductive losses decreased when the physical size of the silver particles exceeded the skin depth at that particular frequency. It was found that the output power was the dominant parameter affecting the heating rate of the VFM heating profile.

Rapid VFM curing of polymer dielectrics has been proposed [39]-[41]. Two commercially negative tone photosensitive polyimides were analysed in the hope that VFM curing would significantly reduce the curing cycle while maintaining comparable post cure electrical, mechanical and chemical properties with convection curing. Bidstrup-Allan *et. al.* [41], used a variety of experimental techniques for characterising the mechanical, electrical and chemical properties of the films for both VFM and thermal cure cycles. Residual stresses were determined by measuring the changes in curvature of silicon wafers as a result of deposition and curing of the polymer film. CTE and biaxial modulus parameters were determined by calculating the slope of the stress versus temperature curves for identical film on both silicon and gallium arsenide wafers. Tensile properties were measured by lifting film strips off the wafer substrate by immersing the sample in hydrofluoric acid. This process etches the native oxide on the silicon wafer and releases

the polymer strips. Each strip was then pulled to determine the point of failure. Youngs modulus was determined from the low strain region of the stress-strain curve. Electrical properties were measured using a parallel plate capacitor arrangement with the polymer film as the substrate. Capacitance and conductance measurements were made and used to calculate the permittivity and loss tangent. The chemical changes within the sample during condensational reaction and as percent conversion as a function of cure was monitered using Fourier transform infared spectroscopy (FTIR) [41]. The FTIR analysis showed that VFM curing of photosensitive polybenzoxazoles leads to identical post cure propeties as compared to conventiocal thermal curing.

An investigation of flip-chip underfill encapsulants was presented by Mead *et. al.* [42]. T_g, CTE and the elastic modulus were measured and compared to conventional thermal heating processes. T_g and CTE were measured using a thermo-mechanical analyser (TMA). Samples were cut into small strips and the elastic modulus analysed using a rheometrics solids analyser. Mead *et. al.*, concluded that VFM processing of encapsulant underfills offered faster curing times and comparable post-cure material properties, when compared to thermal cure processing. The complex heating environment of the flip-chip structures produced small frozen stresses within the samples. These residual stresses were removed by exposure to a temperature cycle sufficient to induce relaxation of the frozen stresses.

Li and Liu [43] presented results describing microwave heating using a single mode for the curing of epoxy based adhesives. Specifically, the authors investigated the effects of different curing agents, the amounts of curing agent required and the effect of the addition of carbon black on the curing rate. The exposure to microwave radiation was performed with a single mode applicator operating at a frequency of 2.45GHz with a maximum continuous output power of 300W. Diglycidyl ether of bisphenol F-based epoxy adhesives were formulated to investigate the curing mechanism. Carbon fibre and carbon black were introduced into the polymer based epoxy in order to increase the dielectric material properties. Li and Lui concluded that the curing rate increased as the proportion of Imidazole I increased. The effect of increasing the amount of carbon fibre and carbon black amounted to an enhancement in the curing rate.

A thermal-electromagnetic coupled computation solver was presented by Glinski and Bailey [44] based on heat flow by conduction and Maxwell's equations. The computational model was applied to the curing of adhesives and underfills on a chip assembly

where transient internal temperatures were calculated within each component. Particular interest was given to the critical region between chip and substrate. The results presented by Glinski and Bailey showed that the heating properties of the adhesive material was not the most significant factor due to the difference between the small quantity of the adhesive and the comparably large quantity of substrate and chip assembly.

Wang and Lui [43] investigated the relationship between microwave transmission through an ECA and the resulting heat generation and transfer within the ECA. In addition, the microwave heating rate was calculated. It was shown that the penetration depth of the skin effect in the metal filler was significantly less than a bulk metal material. The conduction losses within the metal filler were found to be negliable due to the large electrical conductivity. For this reason, the heat generation due to microwave loss can be confined to the adhesive flux. In addition, the thermal equilibrium between the metal filler and surrounding adhesive was reached within one nanosecond due to the high thermal conductivity. The temperature distribution within the ECA sample was approximately uniform due to the microwave power lost within the adhesive minus the heat radiation from the sample surface. The theoretical model was validated using experimental data and was found to be in good agreement.

Lead-free soldering of interconnects using VFM technology was presented by Moon *et. al.* [45], [46]. Melting of solder paste and the wetting on metal pads was achieved through VFM heating of the organic flux vehicle. Heat was deposited from the flux vehicle to solder through normal thermal conduction. Solder joints, formed through the conventional reflow methods, were compared to joints formed by VFM using the Lambda Technologies MicroCure 2100 VFM Oven [47]. Peak temperatures in the reflow and VFM ovens were varied while the preheat temperature, ramping rate and whole reflow process remained static. The solder joints from both these processes were then compared and their intermetallic compounds (IMC) analysed. It was found that VFM deposited more heat energy into the solder paste as compared to conventional reflow at similar peak temperatures due to the uniform heating effect. Temperature gradients in the test boards were reduced indicating that the overall peak temperature could be reduced through the use of VFM.

Noh *et. al.*, presented a novel wafer bonding technique, using VFM heating, for the bonding of parylene intermediate layers [48]. A variety of substrate materials with varying coefficients of thermal expansion were bonded using the presented method. Heat was

primarily deposited within the parylene layer, reducing the stresses caused by thermal expansion mismatches. In addition, the presented method reported a uniform, rapid, low temperature, chemically stable approach to wafer bonding. Noh *et. al.*, found that the novel approach required a slightly higher tensile bonding strength as compared to other bonding techniques reported in the literature.

A coupled heat transfer and cure kinetic finite element simulation model was presented by Liu *et. al.* [49], [50]. Temperature distribution inside underfill due to VFM heating was calculated (using the anisotropic heat conduction equation) including the internal heat generation due to exothermic chemical reactions. The cure kinetic parameters were obtained by non-isothermal method from results of temperature scans using differential scanning calorimeter (DSC). Simulated results of isothermal and non-isothermal cure models were in good agreement with measured results. Longer curing times were required for lower input powers. Liu *et. al.*, concluded the VFM oven process of underfills produced uniform heating and conversion.

Yi *et. al.* [51], presented a three dimensional, finite element method, for investigating curing methods applied to underfills within a microwave cavity. The curing behaviours and mechanical properties of each underfill were measured experimentally for both VFM and thermal cures before being compared to modelled results. Results showed that the position of the underfill and the size of the sweep bandwidth had an effect of the uniformity of the cure. A greater amount of natural resonant modes (coupled within the oven) produced a greater uniformity in energy distribution.

Fontana *et. al.* [52], presented investigations into the VFM curing of die attach and underfill materials. Doping levels, die attach adhesive and underfill material comparisons (for a number of VFM experiment configurations) were conducted and the effect of polymerisation, voids in the cured material and moisture absorption recorded. It was reported that doped dies coupled to VFM energy and assisted in adhesive curing while un-doped dies did not demonstrate "full VFM capability". Fontana *et. al.*, presented an electrical loss comparison between doped and un-doped dies in the form of resistivity versus doping concentration. An increase in die doping level will increase conductivity, thus allowing for an increase in tan δ [38], [53]. It was concluded that VFM did not change the functionality of the chip and the carrier temperature decreased with distance from the die. Two silver filled, high thermal adhesives were used in the analysis. It is reported that there was little effect on the number of detected voids within the material and the

maximum cure temperature. However, using the analysis of variance (ANOVA) analysis, they found a,

> "statistically significant relationship between the temperature slope and voids at 99% confidence level."

An optimum value for the temperature slope of around $0.4°$C/s was reported. A stepped temperature versus time relationship was found to reduce the overall curing time of the system for similar output results. Finally, one underfill and two non-filled capillary underfills were tested. The no-filled materials performed better than the filled materials due to longer dwell and curing times.

Jiang *et. al.* [54], presented investigations into the synthesis of silver particles based on a polyol process and VFM curing method. The reactions between the VFM method and conventional thermal heating methods were compared. The effects of sliver nitrate and poly(N-vinylpyrrolidone) (PVP) concentration, reaction times and reactions temperature effect on particle size were analysed. VFM heating produced a faster reaction (as compared to convection heating) leading to a higher concentration of Ag nanoparticles with the same temperature exposure and heating time. It was concluded that VFM heating had a significant effect on the yield of the nanoparticles with no effect on the particle growth leading to a narrower distribution of Ag nanoparticles.

2.3 Focussed Heating Mechanisms

2.3.1 Minimally Invasive Medical Applications

A technique for providing microwave hyperthermia treatment consists of locating a number of antenna array elements around the body and on the same plane as the tumour. Devices configured in this manner are commonly referred to as annular phased arrays (APAs) [55]-[65]. A bolus (filled with de-ionised water) is placed in direct contact between the antenna elements and the body. A bolus of this type not only aids in impedance matching, but also provides a cooling mechanism to counteract superficial heating of the skin. An energy deposition maxima can be placed at a variety of points within the treatment region through adjustment of the excitation amplitude and phase at each antenna element. However, non-invasive monitoring of the temperature distribution is difficult as the materials within the treatment region are heterogeneous in nature and vary from patient to patient leading to complex real-time calculations. It is possible to insert a small

probe or antenna into the tumour region [62], [66]-[68] in order to either heat the tumour or provide a coherent source for the APA excitation calculation. This arrangement is often undesirable due to tumour location or the possibility of patient discomfort. Improper choice of excitation coefficients may lead to undesirable *hot-spots* within the treatment region leading to an increased risk of damage to surrounding healthy tissue [69]. It is often the case that the maximum energy deposition does not coincide with the maximum temperature disposition due to the complex nature of the biological materials within the human body.

A method for determining the excitation amplitude and phase of antenna array elements for an electromagnetic multi-applicator system was proposed by Boag and Leviatan [56]. An effective procedure was described for optimising the electromagnetic power absorbed by a deep-seated tumour region within the human body. Boag and Leviatan employed a similar optimisation routine to the general optimisation routine proposed by Harrington [57]. Excitation coefficients were found by maximising a dimensionless performance index for use within an eigenvalue matrix equation. Simulations were conducted on a tumour seated deep within a 2-D cylindrical body model consisting of five different homogenous regions. The optimisation routine contributed to an overall decrease in the heating of healthy homogenous regions when compared to a uniform excitation. Sawyer *et. al.* [58], [59], proposed controlling the excitation of an antenna array through using retro-focusing. The principle of the experiment was derived from Loane *et. al.* [66], where an interstitial antenna, placed in the tumour region, would act as a coherent source. An antenna array outside of the body receives the signal from the inserted antenna. The phase delay from the source is measured allowing for the excitation of the array elements to be adjusted accordingly. Sawyer *et al.*, used the incoherent thermal emissions from the tumour as a source for retro-focusing.

A method for finding the optimal surface distribution on a spherical high water-content phantom was proposed by Rappaport and Pereira [60] for the delivery of maximum power to an arbitrary located, deep-seated tumour. An optimisation routine used spherical field harmonics, centred on the tumour region, summed with complex weighting variables in order to minimise surface power. Once the optimisation of the surface power is complete, the current element coefficients, which produce the surface distribution, are calculated. The calculated current coefficients represent the theoretical ideal that would produce maximum deep heating at the tumour. It was acknowledged that, in practice, no physical applicator would be able to produce similar results. The optimisation routine

represented a "benchmark" that applicators could be measured against in order to analyse focusing ability. Rappaport and Pereiras work was extended by Dunn *et. al.* [62]. A Finite Difference Time Domain (FDTD) analysis was conducted on a human head phantom in order to investigate focused target heating. The MRI-scanned human head model was excited by the spherical source distribution as suggested by Rappaport and Pereira. They concluded that, even with no optimisation to account for the inhomogeneities of the human head, reasonable focusing ability at depth was possible. It was observed that changing the type of bolus had a noticeable effect on focusing precision. A muscle-type bolus was preferred over a bone-type bolus, as the former yielded a sharper focus.

Jacobsen *et. al.* [63], presented a dual mode microwave antenna capable of heating superficial tissue while, at the same time, monitoring the temperature of the tissue using radiometric techniques. The radiometric signal sensitivity was increased by a factor of two by proper placement of the receiving antenna when compared to previous designs. Kowalski *et. al.* [64], [65], described a temperature based feedback control system for use with an APA. By using temperature as a basis for the control of the excitation coefficients, the system provided conpensation for local blood perfusions rates and other factors that could significantly change the treatment region parameters. The hybrid control system made use of the proportional-integral (PI) in time and maximisation of the performance index in space. Electromagnetic field modelling was achieved using the FDTD method and temperature deposition modelling achieved using the biological heat transfer equation (BHTE).

Nikawa *et. al.* [70], described a waveguide type applicator for depositing microwave energy inside the human body at a frequency of 430MHz. This type of applicator is commonly known as a lens applicator. Moveable metal plates were placed inside the aperture of the waveguide to allow the depth of the electric field maxima to varied. The plates have the effect of changing the phase velocity of the wave travelling through the aperture, such that the spatial peak of the electric field appears inside the dissipative medium. The concave shape of the aperture ensured proper contact between the biological body and the actual unit itself. Measurements were conducted in a lossy medium. Nikawa's *et. al.*, results suggested that a maximum electric field could be produced [within a lossy medium] instead of at the surface through adjustment of the moveable metal plates within the applicator unit.

Another type of microwave hyperthermia applicator, which has received some attention

in the literature, is the reflector applicator [71]-[73]. Underwood *et. al.* [71], described an applicator where a partial sphere cavity was used to excite an array of slots. Through using a reflector applicator, it was possible to focus the energy deposition by varying the number of the slots of the array. A unique feature, reported by the authors, is that the applicator conforms to both spherical surfaces (such as the head) and to planar surfaces. A maximum heating depth of 3cm is reported at an operating frequency of 2450MHz; a factor of 1.8 times greater than the maximum heating depth of conventional waveguide applicators. Sabaeriego *et. al.* [73], proposed an APA type applicator surrounded by a semi-circular reflector. The reflector increases the penetration and focalisation of energy in malignant cells. The proposed technique applied method of moments (MoM) to form a model of the problem. Synthesis of the excitation coefficients was performed using conjugate field matching (CFM) and near field power maximisation (NFPM) techniques. It was demonstrated that focussing of electromagnetic energy was achieved in the tumour phantom. However, reaching the deepest regions was not possible due to power losses within the model.

Kanai *et. al.* [74], analysed focused hyperthermia treatment in a re-entrant resonant cavity where the time dependent electromagnetic-heat transfer equations were solved. A torso shaped phantom (representing a human body) was placed in the high field region within the re-entrant cavity, and the electromagnetic-heat transfer calculations performed. It was found that, through loading the phantom with suitably shaped cylindrical conductors, electromagnetic energy could be directed towards the centre of the cavity.

2.3.2 Phased Array Technologies

Commercial hyperthermia treatments are quite advanced; in particular, the use of phased arrays to focus microwave energy to a specific treatment region. Two companies in particular have produced commercially available solutions. BSD Medical Corporation [75] have hyperthermia treatment solution based on the use of a phased array solutions called *BSD-2000*. A paper describing the technology used in the BSD system was first published by Fenn *et. al.* [61]. The BSD-2000 / 3D [76] contains twenty four dipole radiators that maximise the 3-D energy convergence at the targeted treatment location and incorporates dynamic 3-D control and steering of the heating pattern size, shape, depth and position. The phased array section of the BSD-2000 / 3D is known as *Sigma Eye*.

Sigma Eye can achieve a central focus of approximately 9cm (approximately a third of

the wavelength of the diseased tissue). This focusing ability enables deep tumours to be non-invasively treated by the *Sigma Eye* applicator. The 3-D electronic steering capability of *Sigma Eye* can position and shape the energy focus in the long body axis as well as the axial cross-section.

The BSD-2000 / 3D / MR [77] enables MRI as an interface with the BSD-2000 / 3D. The development of MRI treatment monitoring has been an advancement in hypothermic oncology. Among the many benefits, MRI treatment monitoring opens the way for the application of MRI monitored hyperthermia for better treatment of new cancer sites, using non-invasive imaging (including temperature monitoring) of tumours during therapy. BSD Medical has received FDA approval for all versions of the BSD-2000.

Another company dedicated to producing hyperthermia solutions is Celsion [78]. Celsion was created in 1997 with the acquisition of the commercial rights to Massachusetts Institute of Technology's (MIT) adaptive phased array thermotherapy technology for cancer and other medical treatments. Celsion was founded in 1982 under the name Cheung Laboratories Inc., to pursue a vision of using heat to kill cancer and treat other diseases. The concept of heat-based treatment systems was viable but, as with many endeavours in medical science, ahead of its time. The then available technology simply could not deliver adequate results. In 1997, the company was renamed Celsion Corporation, and was reorganised around achievable goals with an emphasis on benign prostatic hyperplasia (BPH) and breast cancer treatment systems. Since that time, and in addition to moving forward in the areas of BPH and breast cancer, Celsion has expanded the development of other modalities, including drugs and gene-based biological modifiers, which may be rendered more effective by using heat in their application.

Celsion is investigating four complementary treatments: adaptive phased array (APA) heat treatment, benign pro-static hyperplasia treatment, heat-activated liposomes and heat-activated gene based cancer repair inhibitor. In 1994, Fenn *et. al.* [4], produced an early indicator on the possibly of phased array control. Celsion has worked closely with Fenn to adapt technology initially for the defence industry, into hyperthermia treatments for killing cancer cells while simultaneously avoiding damage to healthy tissue. The company has applied this technology in two trials for the treatment of breast cancer [79]. In this treatment, a focusing probe is inserted into the centre of the tumour. Microwave energy is then directed at it from applicators positioned on either side of the compressed breast. The microwaves generate volumetric heat, killing cancer cells in the tumour and

its margins. Additionally, since microwaves are most effective at heating tissues with high water content, they preferentially heat cancer cells, and spare the microwave-inert fatty tissues in the breast. A disadvantage of this particular solution is that it is minimally invasive.

Fenn *et. al.* [80], proposed a monopole adaptive phased array for deep tumour treatment. Stray radiation along the longitudinal axis was identified as a limiting factor in the use of APAs. Radiating monopoles were placed within a cylindrical waveguide cavity thus increasing patient safety and eliminating the need for radiation shielding of sensitive equipment within the treatment room. The design consists of eight equally spaced monopole radiators placed in a ring configuration. Source signals are weighted such that the radiated power, within the treatment area, is at a maximum. An elliptical aperture is placed in the centre of the transverse plane for receiving the body. Although the design in non-invasive, a small electric field sensitive probe is placed on the surface of the body in order to detect radiation from the monopoles. The controlling circuitry, attached to the electric field probe, calculates the amplitude and phase of the signals fed to the monopole radiators such that one or more nulls are formed on the surface of the body while maintaining maximum electric field magnitude in the treatment area [61]. The null areas penetrate the skin such that the likelihood of skin trauma is reduced. An elliptical acrylic ring is placed in the waveguide cavity aperture enabling the cavity to be filled with water. The patient treatment area is within the aperture ring. A flexible, cooled water bolus was used to aid in the transfer of energy into the body and to cool the surrounding skin further reducing the likelihood of damage. Results showed a single peak of electromagnetic energy within the treatment area indicating the desired performance was achieved.

2.4 Complex Permittivity Measurements of Epoxy Resin

Epoxy resins are used within many applications such as printed circuit board manufacturing, adhesives and surface coatings [81]. Research into the curing of epoxy and other thermosetting resins is at an advanced stage. Of interest is the requirement to monitor the degree of cure within epoxy adhesives and encapsulants using thermal heating processes [82]. Investigation of the degree of cure within epoxy resins can be achieved using waveguides [29], [30] and multi-mode microwave ovens [31], [32]. Several measurements of epoxy dielectric properties have been detailed at frequencies between 0.1Hz and 10MHz using electrodes [83], microelectrodes [84], [85] and low frequency spectrum analysers

[86]. Also, dielectric measurements have been made within the microwave frequency range using waveguides [87] and transmission lines [31].

Dielectric property measurements play a highly critical role in characterisation of materials for different applications. Many techniques have been employed and developed for measuring the complex permittivity and permeability of materials [88]. One technique for measuring the complex permittivity at high frequencies is through utilising a high Q resonant cavity. However, the major disadvantage of this technique is that only a narrow frequency range can be analysed [89]. To measure the complex permittivity over a wider range of frequencies, transmission line methods may be used [90].

Elkhazmi *et. al.* [91], explored a method of improving the measurement of complex permittivity using a coaxial line test cell. The measurements were performed using numerous methods employing various sample sizes and shapes [92]. The permittivity of the sample was calculated from the reflection data obtained from measurements in either the frequency or time domains. Elkhazmi *et. al.*, examined the need to develop this method to measure the complex permittivity of plastic moulding materials. The coaxial line method enabled the permittivity to be measured over a very wide frequency range. However, it also posed several problems. These included the difficulty of constructing a coaxial test cell with a diameter that would not interfere with network analyser and the accurate measurement of low dielectric losses. The results of the mixed time and frequency domain method concluded that the use of coaxial line reflection methods were successful in measuring accurate resistance losses of the test cell.

Hoang *et. al.* [93], presented an open ended coaxial method to measure the complex permittivity of polymers in the microwave band. The standard behaviour of polymers was observed: the permittivity decreased and the conductivity increased as the frequency increased. The technique presented in the paper showed the open ended coaxial method produced accurate values of complex permittivity in the microwave frequency range. Another aspect of this method is that, due to its non destructive nature, it could used as a sensor for complex permittivity measurement under high temperature conditions.

Whispering gallery modes can be used for very accurate complex permittivity measurements of both isotropic and uniaxially anisotropic dielectric materials. Krupka *et. al.* [94], discussed using whispering gallery modes to measure real permittivity and temperature coefficients before calculating the relationship between the complex permittivity,

resonant frequency and the dimensions of the resonant frequency using a mode matching technique. They concluded that whispering gallery modes were an accurate method of determining the complex permittivity and unique for measurements of extremely small dielectric loss tangents. Although the whispering gallery mode technique has difficulties (such as mode identification) it can be used at frequencies up to 100GHz. Mazierska *et. al.* [95], attempted to identify a similar technique to the whispering gallery method for measurement the complex permittivity of low loss dielectric substrates at variable temperatures. They found no suitable equivalent of the whispering gallery technique for application to planar dielectrics. The low loss dielectrics could best be characterised using the split post dielectric and spilt cavity resonators. The split post resonator proved to be a useful technique for microwave characterisation of low loss planar dielectrics in a temperature range of 20K to 400K. Mazierska *et. al.*, concluded that measurements of the real part of the permittivity could be calculated with only a small degree of uncertainty and with a very low resolution of loss tangent.

Colpitts [96] reported a temperature sensitivity discussion of coaxial probes in complex permittivity measurements. Colpitts conducted tests over a large frequency range and at various temperatures. The coaxial probe is used extensively in non-destructive measurements of complex permittivity due to its small size and transverse electromagnetic (TEM) operation. Small probe dimensions make the procedure of measuring the complex permittivity at high temperatures very sensitive to deformation of the probe geometrically. The two greatest sources of errors occur due to differing thermal expansion coefficients of the dielectric and conductor and also the hysteresis from the friction between the conductor and dielectric. As Colpits acknowledged that it was common when making measurements of this nature that the samples were not always at the same temperature as the probe. A typical semi-rigid cable is formed from a copper outer conductor, a Teflon dielectric, and a silvered copper covered steel inner conductor. Each of these materials has a different thermal expansion coefficient, with Teflon having the largest. This can cause the dielectric to expand beyond the conductor when hot and recede when cooled. This change in the probe can cause large errors in the measured permittivity. Colpits concluded that the dielectric filled semi-rigid coaxial probe was very sensitive to temperature when used to measure complex permittivity. He found that even though the accuracy was very good when the probe was calibrated, it decreased significantly when the probe was heated and cooled beyond calibration temperature.

Jow *et. al.* [82], investigated the use of a single mode resonant cavity in conjunction with

temperature measurements to process epoxy. A single mode resonant cavity was utilised such that material cavity perturbation theory could be employed to analyse the loaded and unloaded cavities. The results concluded that the dielectric properties of epoxy were functions of the extent of the cure, temperature, composition and frequency. The experiments also showed that the dielectric properties of epoxy decrease with an increase in the degree of cure and decreasing the temperature.

A method was proposed by Marand *et. al.* [97], to monitor the changes in the dielectric and epoxy material as they were cured by microwave and thermal energy. The dielectric constant was periodically measured while cure occurred within the waveguide volume. Resonant frequency and Q for a loaded and unloaded cavity were also measured. The complex permittivity was then calculated using the perturbation method. Marand *et. al.*, also presented the idea of monitoring the molecular changes in the epoxy using the Fourier transform. This was achieved through inserting a small fibre-optic cable into the sample which allowed the extent of the reaction to be observed for a variety of temperatures. Results showed that microwave radiation accelerates the curing reaction at the beginning of the process but due to rigid molecular structure, the cure was actually of a lower degree. It also highlighted that the rigid molecular structure in the epoxy occurred at a much higher rate when cured by microwave radiation rather than thermally. This result was only for a single type of epoxy and it was conceeded that different molecular systems may exhibit alternative behaviour.

CHAPTER THREE

THE THEORY OF WAVEGUIDE CAVITY RESONATORS

3.1 Introduction

An understanding of the electromagnetic conditions required to achieve wave propagation and resonance within a waveguide structure is essential for the preparation and analysis of the applicator systems described within this thesis. This chapter provides an outline the theoretical topics surrounding the analysis of waveguide cavities.

A brief summary of the historical background as to the invention of waveguide is provided. Maxwell's equations are defined and related to the physical electromagnetic properties of a medium. The boundary conditions are defined for an interface between two differing mediums: a perfect conducting wall and a perfect magnetic wall. The boundary conditions are then applied to a Helmholtz solution of Maxwell's equations to give the electric and magnetic field in terms of their x, y and z components for both transverse magnetic (TM) and transverse electric (TE) modes within rectangular and cylindrical waveguide cavity. In addition, a number of propagation parameters are defined.

The Quality Factor within a lossy waveguide cavity and the influence of the Quality Factor on quasi degenerate modes is discussed. Evanescent fields within below cut-off waveguide are described in terms of the rate of attenuation of the field. Methods of coupling energy into the waveguide cavity resonator are highlighted and the associated benefits and drawbacks of each method described. Cavity perturbation is introduced in terms of the inclusion of tuning screws within the volume of the cavity for tuning of the resonant frequency.

3.2 A Brief History of Electromagnetic Waveguide

The field of electromagnetic analysis and microwave engineering is now considered a mature subject. The fundamental roots of the subject were developed by James Clerk Maxwell [98] in 1873 where he hypothesised electromagnetic propagation and the notion that light was a form of electromagnetic wave. Around 1886, Oliver Heaviside went on to develop much as what is considered as the modern form of Maxwell's equations. Although Heaviside had considered the possibility of wave propagation within a hollow metal tube, he rejected the idea believing that two conductors were required to facilitate electromagnetic wave propagation [99].

At this time J. J. Thompson gave a theoretical analysis of the electric field within a conducting cavity of finite length [100]. He concluded that the permissible modes were a function of the radius of the cylindrical cavity. Later, J. Lamor [101] conducted a similar analysis to that of Thompson, investigating resonant structures such as coaxial metallic cylinders and a single dielectric slab.

However, it was Lord Rayleigh who, in 1897, gave the definitive mathematical description of propagating electromagnetic waves within the conducting hollow tube [102]. Rayleigh is credited with proving that, not only could a metal tube propagate an electromagnetic wave, but also the energy that existed within the structure was that of well-defined normal modes. Furthermore, the waves created had either a component of the electric field in the longitudinal direction only or a component of the magnetic field in the longitudinal direction only. Both cases produce transverse electric and magnetic field components. He also proved that the frequency at which these waves existed must be greater than a lower limit dictated by the physical dimensions of the structure [103].

It was not until 1936 that two men independently rediscovered the possibility of propagation through waveguide. George C. Southworth and W. L. Barrow presented papers providing the experimental confirmation of electromagnetic wave propagation using waveguide [104].

3.3 Waveguide Cavity Resonators

A waveguide cavity resonator can be described as a transmission line of finite length with reflecting boundaries in the direction of propagation. While the purpose of a transmission line is to transmit power from one point to another, a resonator cavity will store energy at a rate dependent on the properties of the structure and excitation. Reflection of the propagating wave will occur through the placement of a short-circuit or open-circuit boundary conditions in the direction of propagation. In practice, a suitable open-circuit condition is difficult to achieve due to a small [but significant] radiation loss from the open aperture. Radiation loss gives rise to a *real* component of the impedance of the termination and is the source of the loss. For this reason, waveguide cavity resonators are normally formed with short-circuits at each end of the waveguide forming a closed box. Electric and magnetic energy can then be *physically* enclosed within the cavity structure. Power is coupled into the cavity through the use of probe, loop or slot feeds.

A resonant waveguide cavity has many advantages and uses at microwave frequencies. Microwave resonators are integrated into many applications such as filters, oscillators, frequency meters and tuned amplifiers. Cavities can have a very high Quality Factor (Q) and can be built to handle relatively large amounts of power. Cavities with a Q value in excess of 3x10^5 are not uncommon. The high Q gives these devices a narrow bandpass and allows for very accurate tuning. Simple, rugged construction is an additional advantage. Waveguide cavity resonators may be built for many different frequency ranges and applications and can have a variety of shapes.

3.3.1 Maxwell's Equations

Maxwell's equations are well documented within the literature. However, for completeness, they are replicated within this thesis. If a linear media is assumed then Maxwell's equations can be written in phasor form [105] as,

$$\nabla \times \vec{E} = -j\omega\mu\vec{H} - \vec{M} \tag{3.1}$$

$$\nabla \times \vec{H} = j\omega\varepsilon\vec{E} + \vec{J}_s \tag{3.2}$$

$$\nabla \times \vec{D} = \rho_s \tag{3.3}$$

$$\nabla \times \vec{B} = 0 \tag{3.4}$$

where $\vec{E}$ is the electric field (V/m), $\vec{H}$ is the magnetic field (A/m), $\vec{M}$ is the (fictitious) magnetic current density (V/m^2), $\vec{D}$ and $\vec{B}$ are the electric (Coul/m^2) and magnetic flux density (Wb/m^2), respectively. ρ_s and $\vec{J}_s$ are the electric charge density (Coul/m^3) and electric current density (A/m^2), respectively. The electric and magnetic field are related to the flux density through the constitutive relations [106],

$$\vec{D} = \varepsilon\vec{E} \tag{3.5}$$

$$\vec{B} = \mu\vec{H} \tag{3.6}$$

where the permeability μ and permittivity ε are complex and describe the electromagnetic properties of the medium.

$$\mu = (\mu' - j\mu'') = \mu_o(\mu'_r - j\mu''_r) \tag{3.7}$$

$$\varepsilon = (\varepsilon' - j\varepsilon'') = \varepsilon_o(\varepsilon'_r - j\varepsilon''_r) \tag{3.8}$$

Relative quantities are often used to describe the electromagnetic properties of a material and are given by,

$$\mu_r = (\mu/\mu_o) \tag{3.9}$$

$$\varepsilon_r = (\varepsilon/\varepsilon_o) \tag{3.10}$$

where μ_o and ε_o are the free-space constants for the permittivity and permeability, respectively. The real part of permittivity ε' is a measure of the energy storage potential of the material exposed to an electric field and is commonly referred to as the *dielectric constant*. The imaginary part of permittivity ε'' describes the loss factor and includes the effects of both dielectric and conductive losses within the material. The real part of the complex permeability μ' represents the energy storage potential within the material in the presence of a magnetic field, while the imaginary component μ'' represents the energy loss term. Materials such as iron (ferrites), cobalt, nickel, and their alloys have appreciable magnetic properties; however, many materials are non-magnetic, resulting in the complex permeability being very close to the permeability of free space ($\mu_r \approx 1$). All

materials have dielectric properties greater than the permittivity of free-space ($\varepsilon_r > 1$).

The losses within dielectric materials are characterised by a quantity called the loss tangent *tan* δ. A low loss tangent implies loss low within the material. The loss tangent is related to the Q factor by [1],

$$\tan\delta = \frac{1}{Q} \tag{3.11}$$

and can be found by taking the ratio of the real and imaginary parts of the permittivity of the medium.

$$\tan\delta = \frac{\omega\varepsilon^{''} + \sigma}{\omega\varepsilon^{'}} \tag{3.12}$$

The loss tangent is a function of frequency, conductivity and permittivity. If the medium is considered a very good dielectric then the conductivity σ tends to zero and (3.12) becomes,

$$\tan\delta = \frac{\varepsilon^{''}}{\varepsilon^{'}} = \frac{\varepsilon_r^{''}}{\varepsilon_r^{'}} \tag{3.13}$$

3.3.2 Boundary Conditions

Three common boundary conditions are described: the interface between two dielectric materials with differing permittivity, the interface with a perfect electric wall and the interface with a perfect magnetic wall. The boundary conditions determine the propagation parameters and the distribution of the electric and magnetic fields within the waveguide.

The fields between two dielectric materials are determined through,

$$\vec{n} \cdot \vec{D}_1 = \vec{n} \cdot \vec{D}_2 \tag{3.14}$$

$$\vec{n} \cdot \vec{B}_1 = \vec{n} \cdot \vec{B}_2 \tag{3.15}$$

$$\vec{n} \times \vec{E}_1 = \vec{n} \times \vec{E}_2 \tag{3.16}$$

$$\vec{n} \times \vec{H}_1 = \vec{n} \times \vec{H}_2 \tag{3.17}$$

Equations (3.14)-(3.17) state that the normal electric flux density, normal magnetic flux density and the tangential electric and magnetic field components are all continuous through the material interface. The boundary conditions associated with a perfectly conducting surface are,

$$\vec{n} \cdot \vec{D} = \rho_s \tag{3.18}$$

$$\vec{n} \cdot \vec{B} = 0 \tag{3.19}$$

$$\vec{n} \times \vec{E} = 0 \tag{3.20}$$

$$\vec{n} \times \vec{H} = \vec{J}_s \tag{3.21}$$

Equation (3.20) indicates that the tangential electric field is zero at the surface of the perfect conductor (as is the normal magnetic flux density). Finally, the boundary conditions associated with a perfect magnetic boundary condition (open-circuit) are given by,

$$\vec{n} \cdot \vec{D} = 0 \tag{3.22}$$

$$\vec{n} \cdot \vec{B} = 0 \tag{3.23}$$

$$\vec{n} \times \vec{E} = -\vec{M}_s \tag{3.24}$$

$$\vec{n} \times \vec{H} = 0 \tag{3.25}$$

3.3.3 Wave Propagation

If a time harmonic field with $e^{j\omega t}$ time dependence is assumed, then the propagating fields along the z-axis can be written as,

$$\vec{E}(x,y,z) = [\vec{e}(x,y) + z\vec{e}(x,y)]e^{-j\beta z} \tag{3.26}$$

$$\vec{H}(x,y,z) = [\vec{h}(x,y) + z\vec{h}(x,y)]e^{-j\beta z} \tag{3.27}$$

Equations (3.26) and (3.27) are valid for a lossless medium. Within a lossy medium, the propagating wave will attenuate in the direction of travel and β is substituded by γ,

$$\gamma = (\alpha - j\beta) \tag{3.28}$$

where γ is the complex propagation constant and α is the attenuation constant. If the region or transmission line is source free then Maxwell's equations can be expressed as,

$$\nabla \times \vec{E} = -j\omega\mu\vec{H} \tag{3.29}$$

$$\nabla \times \vec{H} = -j\omega\varepsilon\vec{E} \tag{3.30}$$

Solving (3.29) and (3.30) gives four transverse field equation in terms of the longitudinal field component [107],

$$H_x = \frac{j}{k_c^2}\left(\omega\varepsilon\frac{\partial E_z}{\partial y} - \beta\frac{\partial H_z}{\partial x}\right) \tag{3.31}$$

$$H_y = -\frac{j}{k_c^2}\left(\omega\varepsilon\frac{\partial E_z}{\partial x} + \beta\frac{\partial H_z}{\partial y}\right) \tag{3.32}$$

$$E_x = -\frac{j}{k_c^2}\left(\beta\frac{\partial E_z}{\partial x} + \omega\mu\frac{\partial H_z}{\partial y}\right) \tag{3.33}$$

$$E_y = \frac{j}{k_c^2}\left(-\beta\frac{\partial E_z}{\partial y} + \omega\mu\frac{\partial H_z}{\partial x}\right) \tag{3.34}$$

where,

$$\beta = \sqrt{k^2 - k_c^2} \tag{3.35}$$

and k_c is the cut-off wavenumber. k is the wavenumber of the material filling the transmission line or medium. The wavenumber is a function of the frequency of excitation and the material properties within the waveguide.

$$k = \omega\sqrt{\mu\varepsilon} = \frac{2\pi}{\lambda} \tag{3.36}$$

3.3.4 Propagation Parameters

Unlike a two wire transmission line, a waveguide transmission line does not support a transverse electromagnetic (TEM) wave. Waveguide consisting of a single hollow conductor will support a transverse electric (TE) wave or transverse magnetic (TM) wave.

The relationship between TE waves and TM waves is characterised by the presence of a longitudinal magnetic or electric field component, respectively. Both TE and TM modes have a cut-off frequency below which no propagation occurs. Generally, the fundamental (lowest order) TE or TM mode is often the mode of choice for propagation. Discontinuities within the guide will often excite higher order modes. Excitation at frequencies well below the cut-off frequency of the [spurious] higher order modes eliminates the likelihood of the these unwanted modes propagating through the waveguide system since the high order modes are evanescent and attenuate in the direction of propagation confining them to the locality of the discontinuity.

TE modes are defined as modes for which $E_z = 0$ and $H_z \neq 0$, while TM modes are defined as modes for which $E_z \neq 0$ and $H_z = 0$.

Electric and magnetic field distribution within waveguide cavity geometries are found through solving the Helmholtz equation [108],

$$(\nabla^2 + k^2)\vec{A} = 0 \tag{3.37}$$

where ∇^2 is the Laplacian operator, k is the wavenumber and $\vec{A}$ is an unknown function $\vec{A}(x, y, z)$ in a 3-D space. For electromagnetic analysis within waveguide, the unknown function A is either the electric field or magnetic field depending on whether the solution is based around a TM or TE mode. The general solution of the TE wave is characterised by $E_z = 0$ and $H_z \neq 0$. Equation (3.37) is simplified resulting in the reduced wave equation for a two dimensional wave (partial differential equation),

$$\left(\frac{\partial}{\partial x^2} + \frac{\partial}{\partial y^2} + k_c^2\right) h_z = 0 \tag{3.38}$$

since $\vec{H}_z(x, y, z) = h_z(x, y)e^{-j\beta z}$ and $k_c^2 = k^2 - \beta^2$. Equation (3.38) is then solved using appropriate boundary conditions for the specific waveguide geometry. A similar analysis can be conducted for TM waves characterised by $E_z \neq 0$ and $H_z = 0$. Equations (3.31)-(3.34) are simplified for each transverse field component of the electric and magnetic field in terms of either the longitudinal magnetic field component (for TE waves) or the longitudinal electric field component (for TM waves).

3.3.5 Power Flow and Evanescent Mode Attenuation

In order for an electromagnetic wave to propagate within waveguide (and set-up a standing wave within a cavity), β must be real and non-zero. However, it is not strictly the case that absolutely no field exists for non-real β within cut-off waveguide. At the cut-off frequency, $\beta = 0$ and the mode will attenuate in the direction of propagation.

The attenuation of the power flow in below cut-off waveguide is finite and is only infinite when the excitation frequency is equal to zero. The presence of finite conductivity within the conducting walls allows for coupling between the electric and magnetic fields. The propagation of a mode does not stop at a particular frequency; there are a range of frequencies at which the transition of the propagating mode to a more highly attenuated mode occurs. The attenuation α of a non-propagating [evanescent] mode within a below cut-off waveguide [109] is given by,

$$\alpha = \beta_o \sqrt{\left(\frac{\lambda_o}{\lambda_c}\right)^2 - 1} \tag{3.39}$$

where β_o is the phase constant in an unbounded medium, λ_o is the wavelength in an unbounded medium and λ_c is the cut-off wavelength of the waveguide. Equation (3.39) is valid for a waveguide fully filled by a dielectric material. The attenuation is measured in nepers per metre and is converted to decibels per metre through applying a multiplication factor. The phase constant for an unbounded medium is found through applying,

$$\beta_o = \frac{2\pi}{\lambda_o} = \frac{w}{c} \tag{3.40}$$

where ω is the angular frequency of excitation and c is the speed of light in a vacuum. For completeness, it should be pointed out that no net power flow exists within a resonating cavity. Rather the fields can be described through the stored energy due to the presence electric and magnetic fields. However, a propagating wave must first exist in order to set up a resonating mode.

3.3.6 Waveguide Cavities

The boundary conditions (3.14)-(3.25) are applied in order to find a solution to the unknown variable in (3.38). H_z is substituted into (3.31)-(3.34) to produce the transverse

electric and magnetic field equations with appropriate boundary conditions. Applying the boundary conditions for a perfect conductor (often referred to as an electric wall or short-circuit) to the reduced wave equation (3.38) for TE and TM waves [110] provides the electric and magnetic field equations for both rectangular and cylindrical cavity geometries.

A full description of the formulation of TE / TM mode electric and magnetic field equations for both rectangular and cylindrical waveguide can be found within the literature [111]-[114].

TE Mode (rectangular coordinates)

$$E_z = 0 \tag{3.41}$$

$$E_x = \frac{j\omega\mu n\pi}{k_c^2 b} A_{mnl} \cos\frac{m\pi x}{a} \sin\frac{n\pi y}{b} \sin\frac{l\pi z}{d} e^{j\omega t} \tag{3.42}$$

$$E_y = -\frac{j\omega\mu m\pi}{k_c^2 a} A_{mnl} \sin\frac{m\pi x}{a} \cos\frac{n\pi y}{b} \sin\frac{l\pi z}{d} e^{j\omega t} \tag{3.43}$$

$$H_x = \frac{j\beta m\pi}{k_c^2 a} A_{mnl} \sin\frac{m\pi x}{a} \cos\frac{n\pi y}{b} \cos\frac{l\pi z}{d} e^{j\omega t} \tag{3.44}$$

$$H_y = \frac{j\beta n\pi}{k_c^2 b} A_{mnl} \cos\frac{m\pi x}{a} \sin\frac{n\pi y}{b} \cos\frac{l\pi z}{d} e^{j\omega t} \tag{3.45}$$

$$H_z = A_{mnl} \cos\frac{m\pi x}{a} \cos\frac{n\pi y}{b} \sin\frac{l\pi z}{d} e^{j\omega t} \tag{3.46}$$

TM Mode (rectangular coordinates)

$$E_z = A_{mnl} \sin\frac{m\pi x}{a} \sin\frac{n\pi y}{b} \cos\frac{l\pi z}{d} e^{j\omega t} \tag{3.47}$$

$$E_x = -\frac{j\beta m\pi}{k_c^2 a} A_{mnl} \cos\frac{m\pi x}{a} \sin\frac{n\pi y}{b} \sin\frac{l\pi z}{d} e^{j\omega t} \tag{3.48}$$

$$E_y = -\frac{j\beta n\pi}{k_c^2 b} A_{mnl} \sin\frac{m\pi x}{a} \cos\frac{n\pi y}{b} \sin\frac{l\pi z}{d} e^{j\omega t} \tag{3.49}$$

$$H_z = 0 \tag{3.50}$$

$$H_x = \frac{j\omega\varepsilon n\pi}{k_c^2 b} A_{mnl} \sin\frac{m\pi x}{a} \cos\frac{n\pi y}{b} \cos\frac{l\pi z}{d} e^{j\omega t} \tag{3.51}$$

$$H_y = -\frac{j\omega\varepsilon m\pi}{k_c^2 a} A_{mnl} \cos\frac{m\pi x}{a} \sin\frac{n\pi y}{b} \cos\frac{l\pi z}{d} e^{j\omega t} \tag{3.52}$$

TE Mode (cylindrical coordinates)

$$E_z = 0 \tag{3.53}$$

$$E_\rho = -\frac{j\omega n\mu}{k_c^2\rho}(A\cos n\phi - B\sin n\phi)J_n(k_c\rho)\sin\frac{l\pi z}{d}e^{j\omega t} \tag{3.54}$$

$$E_\phi = \frac{j\omega\mu}{k_c}(A\cos n\phi + B\sin n\phi)J_n^{'}(k_c\rho)\sin\frac{l\pi z}{d}e^{j\omega t} \tag{3.55}$$

$$H_z = (A\cos n\phi + B\sin n\phi)J_n(k_c\rho)\sin\frac{l\pi z}{d}e^{j\omega t} \tag{3.56}$$

$$H_\phi = -\frac{j\beta n}{k_c^2}(A\cos n\phi - B\sin n\phi)J_n(k_c\rho)\cos\frac{l\pi z}{d}e^{j\omega t} \tag{3.57}$$

$$H_\rho = -\frac{j\beta}{k_c}(A\cos n\phi + B\sin n\phi)J_n^{'}(k_c\rho)\cos\frac{l\pi z}{d}e^{j\omega t} \tag{3.58}$$

TM Mode (cylindrical coordinates)

$$E_z = (A\cos n\phi + B\sin n\phi)J_n(k_c\rho)\cos\frac{l\pi z}{d}e^{j\omega t} \tag{3.59}$$

$$E_\rho = -\frac{j\beta}{k_c}(A\cos n\phi + B\sin n\phi)J_n^{'}(k_c\rho)\sin\frac{l\pi z}{d}e^{j\omega t} \tag{3.60}$$

$$E_\phi = -\frac{j\beta n}{k_c^2\rho}(A\cos n\phi - B\sin n\phi)J_n(k_c\rho)\sin\frac{l\pi z}{d}e^{j\omega t} \tag{3.61}$$

$$H_z = 0 \tag{3.62}$$

$$H_\phi = -\frac{j\omega\varepsilon}{k_c}(A\cos n\phi + B\sin n\phi)J_n^{'}(k_c\rho)\cos\frac{l\pi z}{d}e^{j\omega t} \tag{3.63}$$

$$H_\rho = \frac{j\omega\varepsilon n}{k_c^2\rho}(A\cos n\phi - B\sin n\phi)J_n(k_c\rho)\cos\frac{l\pi z}{d}e^{j\omega t} \tag{3.64}$$

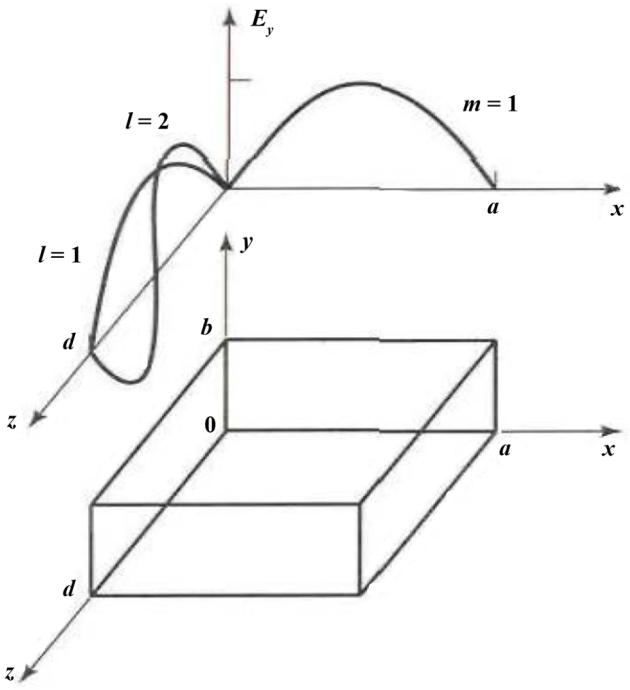

Figure 2: Diagram of x, y, z geometry in a rectangular waveguide cavity showing field variation for TE_{101} and TE_{102} [1].

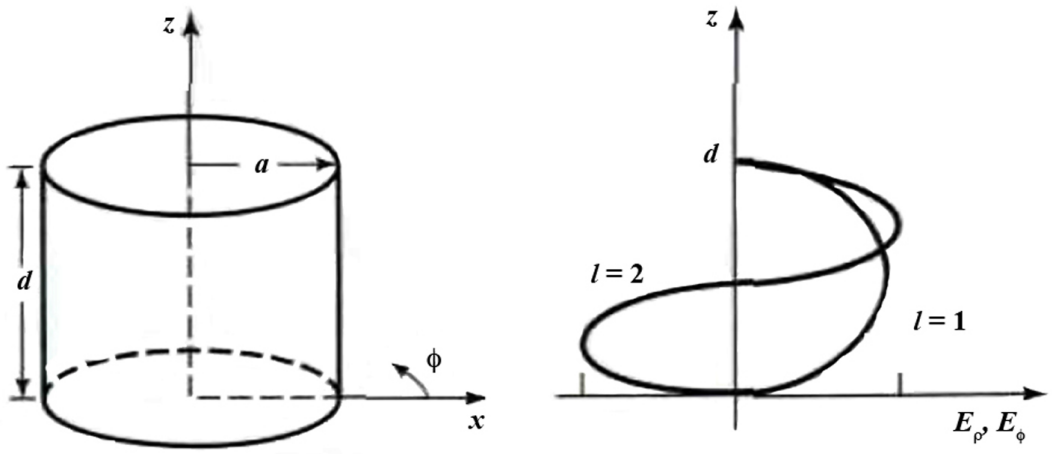

Figure 3: Diagram of ρ, ϕ, z geometry in a cylindrical waveguide cavity [1].

The field patterns within the rectangular waveguide take the form of a sinusoidal distribution as seen within Figure 2. Each field component is an integer number of sinusoidal variations through the axis (represented by m, n and l) with the field maxima scaled accordingly. The magnitude the field component in the direction of propagation (z-axis) is very much greater than the transverse fields and has a phase difference of ninety degrees. The field equations for cylindrical waveguide contain two constants, A and B which independently control the amplitude of the $\sin(n\phi)$ and $\cos(n\phi)$ terms. Because of the symmetrical nature of the azimuthal plane both the $\sin(n\phi)$ and $\cos(n\phi)$ can be considered valid solutions [115]. The magnitude of A and B are determined by the location of the coupling mechanism within the cavity.

A number of propagation parameters are required in order to characterise the propagation within the waveguide (and therefore the resonant properties of a cavity). These parameters can be defined for both TE and TM modes. The cut-off wavenumber within a rectangular waveguide cavity is defined as,

$$k_{mnl} = \sqrt{\left(\frac{m\pi}{a}\right)^2 + \left(\frac{n\pi}{b}\right)^2 + \left(\frac{l\pi}{d}\right)^2} \tag{3.65}$$

where a, b and d are the dimensions of the cavity in the x, y and z direction, respectively. m, n and l are the number of field variations through each axis. A mode will resonate within a cavity at a particular frequency based on the mode order, the physical size of the cavity and the electromagnetic properties of a material within the cavity. The resonant frequency of a TE or TM mode within a rectangular cavity is,

$$f_{TE,TM} = \frac{c}{2\pi\sqrt{\mu_r \varepsilon_r}} \sqrt{\left(\frac{m\pi}{a}\right)^2 + \left(\frac{n\pi}{b}\right)^2 + \left(\frac{l\pi}{d}\right)^2} \tag{3.66}$$

The lowest order resonant mode for a rectangular cavity is the TE_{101} mode. The lowest order mode for the TM wave is the TM_{110} mode. Unlike an infinite length of waveguide (where propagation of a mode will occur at any frequency above the cut-off frequency) the modal resonance inside the cavity theoretically occurs at a single frequency. In practice, resonance occurs over a frequency bandwidth determined by the Q of the resonating mode.

A cylindrical waveguide cavity is constructed in a similar manner as the rectangular cavity. The cut-off number for the TE mode within a cylindrical cavity is,

$$k_c = \frac{p'_{mn}}{a} \tag{3.67}$$

For the TM mode,

$$k_c = \frac{p_{mn}}{a} \tag{3.68}$$

The subscripts m, n and l describe the field variations through the ρ, ϕ and z axis respectively. p'_{mn} are the roots of the derivative of the Bessel function J_o of the first kind of order zero with respect to its argument and p_{nm} are the roots of the Bessel function J_o of the first kind of order zero [116]. The propagation constant is described by (3.35). Therefore, the resonance frequency of a TE_{mnl} mode within a cylindrical waveguide is,

$$f_c = \frac{c}{2\pi\sqrt{\mu_r \varepsilon_r}} \sqrt{\left(\frac{p'_{nm}}{a}\right)^2 + \left(\frac{l\pi}{d}\right)^2} \tag{3.69}$$

The resonance frequency of a TM_{mnl} mode within a cylindrical waveguide is,

$$f_c = \frac{c}{2\pi\sqrt{\mu_r \varepsilon_r}} \sqrt{\left(\frac{p_{nm}}{a}\right)^2 + \left(\frac{l\pi}{d}\right)^2} \tag{3.70}$$

Increasing the permittivity of the material within the cavity decreases the frequency at which a given mode resonates. It is therefore possible, in principle, to increase the order of the mode for a given frequency by filling in the cavity with a high permittivity material. Depending on the specification of a design, there is generally a balance to be achieved between the physical size of cavity, the excitation frequency range, the physical properties of the material contained within the cavity and the order of the resonating mode that is possible to excite within the cavity.

3.3.7 Quality Factor

A useful parameter in the design of resonators is the *Quality Factor* (Q). Q is a measure of the ability of a resonator to store energy and has a significant impact in the coupling of modes within the cavity. A high Q implies a low loss structure while a low Q implies a lossy structure. A perfectly lossless resonator will have infinite Q. Many applications (filters) often require cavities with a very high Q. Sources of loss within a cavity include power dissipated within the cavity walls due to conduction losses, dielectric losses within a material within the cavity volume (especially if the loss tangent is large), radiation losses from a non-radiating gap within the cavity wall and, in certain situations, evanescent losses.

Using Maxwell's equations and assuming $\vec{H} = \vec{H}_v$ (where v is the v^{th} mode resonant within the cavity) [117],

$$\nabla \times \vec{E} = -j\omega\mu\vec{H}_v = -jk_oZ_o\vec{H}_v \tag{3.71}$$

$$\nabla \times \vec{H}_v = j\omega\varepsilon\vec{E}_v \tag{3.72}$$

$$\nabla \times \nabla \times \vec{H}_v = k_o^2\vec{H}_v = k_v^2\vec{H}_v \tag{3.73}$$

where $k_o^2 = k_c^2$ at resonance for the v^{th} mode within the cavity. An $e^{j\omega t}$ time dependence has been assumed but is omitted for simplicity. The stored electric energy for the v^{th} mode can be calculated using,

$$W_e = \frac{\varepsilon}{4}\int_V \vec{E}\cdot\vec{E}^* dV \tag{3.74}$$

where ε is the permittivity. The stored magnetic energy W_m is given by,

$$W_m = \frac{\mu}{4} \int_V \vec{H} \cdot \vec{H}^* dV \tag{3.75}$$

where the permeability μ is a real, non zero, scalar quantity. At resonance,

$$W_e = W_m \tag{3.76}$$

The electric field $\vec{E_v}$ and magnetic field $\vec{H_v}$ are real functions. Maxwell's equations dictate that the electric field be ninety degrees out of phase with the magnetic field. The magnetic currents on the conducting walls of the cavity are found through,

$$\vec{J_s} = \vec{n} \times \vec{H} = \vec{n} \times \vec{H_v} \tag{3.77}$$

The absorbed power within the conducting walls is,

$$\begin{aligned} P_w &= \frac{R_s}{2} \oint_S \vec{J_s} \cdot \vec{J_s^*} dS \\ &= \frac{R_s}{2} \oint_S \left| n \times \vec{H_v} \right|^2 dS \end{aligned} \tag{3.78}$$

where the surface resistivity R_s is given by,

$$R_s = \sqrt{\frac{\omega \mu_o}{2\sigma}} \tag{3.79}$$

The absorbed power within a dielectric material located within the cavity volume is,

$$\begin{aligned} P_d &= \frac{1}{2} \int_V \vec{E} \cdot \vec{J^*} dV \\ &= \frac{\sigma}{2} \int_V \vec{E} \cdot \vec{E^*} dV \\ &= \frac{\omega \varepsilon_o \varepsilon_r \tan\delta}{2} \int_V \vec{E} \cdot \vec{E^*} dV \end{aligned} \tag{3.80}$$

If energy conservation is to be satisfied then the average stored energy must be equal to the total absorbed power [117] hence,

$$-\frac{dW}{dt} = P_L \tag{3.81}$$

where W is the total stored energy of the electric and magnetic fields. From (3.75), (3.78) and (3.80), it can be seen that the absorbed power within the cavity walls and dielectric and the average energy stored are proportional to the square of the field. The absorbed power at any instant of time is proportional to the stored energy. This implies,

$$P_L = 2\alpha W \tag{3.82}$$

A solution to (3.82) is,

$$W = W_o e^{-2\alpha t} \tag{3.83}$$

where,

$$\alpha = \frac{P_L}{2W} \tag{3.84}$$

and W_o is the stored energy at $t = 0$. The field decays according to $e^{-2\alpha t}$, hence the electric field within a cavity at resonant frequency ω_v will have the following time dependence,

$$\vec{E_v} \propto e^{j\omega_v t - \alpha t} \tag{3.85}$$

According to (3.76), the energy stored within the electric field [at resonance] will equal the energy stored in the magnetic field which implies,

$$Q = 2\omega \left(\frac{W_m}{P_w + P_d} \right) \tag{3.86}$$

where P_w and P_d represent the absorbed power in the walls and the absorbed power in the dielectric, respectively.

Therefore, the Q of a cavity can be calculated through substituting (3.75), (3.78) and (3.80) into (3.86) to give,

$$Q = \omega \frac{\mu \int_V \vec{H} \cdot \vec{H}^* dV}{\sqrt{\frac{\omega\mu_o}{2\sigma}} \oint_S |\vec{n} \times \vec{H}|^2 dS + \omega\varepsilon_o\varepsilon_r \tan\delta \int_V \vec{E} \cdot \vec{E}^* dV} \tag{3.87}$$

For the v^{th} resonant mode, the decay in the field magnitude is related to the Q of the cavity through,

$$\alpha_v = \frac{\omega_v}{2Q_v} \tag{3.88}$$

If an infinite Q is assumed then α_v is zero and the cavity is lossless. Modal resonance will occur at a single theoretical frequency. Modes that resonate at exactly the same frequency are said to be *naturally degenerate*. Degenerate modes can occur within rectangular waveguide with square cross-section. By making the cross -section slightly rectangular, orthogonal modes (for example, the TE_{536} and TE_{356} modes) that were once naturally degenerate will become non-degenerate.

The Q of the cavity will decrease as the cavity loss increases. As a result, the frequency response of the resonator (sometimes referred to as the *Q-curve*) will widen, encompassing a greater range of frequencies for which it is possible to couple energy into a mode. If a frequency sweep were to be taken through a typical frequency response of a single resonant mode then the magnitude of the electric and magnetic fields within the cavity would increase from zero to a maximum value (corresponding to maximum coupling) and then back to zero. The position of the electric and magnetic field peaks and nulls within the cavity will remain constant with only the field strength varying. The sharpness of the resonant dip will increase for higher Q cavities. It is possible to maintain frequency separation of near-by resonant modes. Such a feature is useful in the tuning of filter application, for example.

As the Q of the cavity reduces even further, Q-curves that were once completely separate for a high Q modes will start to blend into each one another. At this point the resonant

modes may become quasi degenerate depending on the degree of loss within the cavity and the proximity of each theoretical resonant frequency. The blending of each modal frequency response is represented by differing degrees of coupling through the frequency range. A strongly coupled mode will have a stronger field magntiude within the cavity versus a weakly coupled mode. Multiple modes that are loosely coupled into the cavity can be defined as quasi degenerate. They may become fully degenerate if maximum coupling of each mode occurs at the same frequency. The total field within the cavity is a summation of all coupled modes resonant at the excitation frequency. Exciting the cavity at the frequency mid-way between the Q-curve maxima of each mode (where the coupling for each mode is equal) the overall field distribution will be an equal summation of the electric and magnetic field distributions of each mode.

3.3.8 Waveguide Cavity Excitation

Energy is typically coupled into waveguide cavity resonant modes through either an aperture (fed by waveguide) or a probe / loop arrangement (fed by coaxial cable). The choice of coupling mechanism is generally dependent on the constraints of the design. Multiple slots placed on the walls of a [feed] waveguide such that they intersect paths of magnetic field allow for coupling to be controlled. The length of the slot dictates at which frequency maximum coupling will occur. Very wideband coupling can be achieved through introduction of multiple coupling slots with different lengths corresponding to optimised coupling at specific frequencies as is the case with waveguide directional couplers [118].

On the other hand, probe or loop coupling using coaxial cable are more narrowband but allow for a greater flexibility in the physical geometry or layout of the design. It is possible to introduce multiple coupling probes into a waveguide cavity and optimise the length and position of the probe such that maximum coupling at specific frequencies (excitation of specific modes or range of modes) is obtained. The location of the coupling element will also determine which modes are coupled. Maximum coupling of a mode will occur when the probe is located within the electric field maxima position and aligned parallel to the electric field vector. If the probe is positioned within an electric field null, then no coupling of the mode will occur. The coupling loop antenna acts much in the same manner except the location must correspond with the magnetic field maxima and be located normally to the magnetic field vector.

The purpose of the coupling mechanism is to ensure maximum coupling between feed

line (whether this be waveguide, coaxial cable or some other transmission line) and cavity resonator. The cavity and feed transmission line impedance should be *matched* in order to ensure maximum coupling. The input impedance of the cavity should be equal to characteristic impedance of the transmission line. If this is the case then the cavity is critically coupled to the feed transmission line. The input impedance of the cavity is dictated by the physical size of the cavity, the electromagnetic properties of the materials within the cavity, the type, location and physical properties of the coupling mechanism.

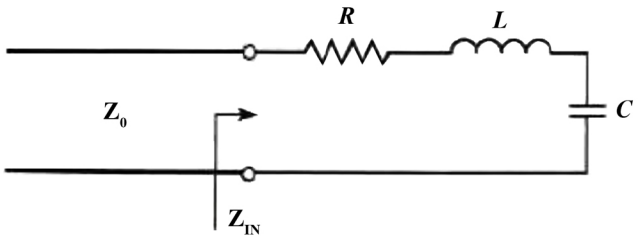

Figure 4: Series resonant circuit with feed line.

The input impedance of the series resonant circuit in Figure 4 [115] is,

$$\begin{aligned} Z_{IN} &= R + jL\Delta\omega \\ &= R + j\frac{2RQ\Delta\omega}{\omega} \end{aligned} \tag{3.89}$$

The unloaded Q at resonance is found using,

$$Q = \frac{\omega_o L}{R} \tag{3.90}$$

The resistance component of the series resonant circuit is equal to the input impedance Z_{IN} at resonance. As such, in order to satisfy this criteria,

$$R = Z_o \tag{3.91}$$

Substituting the result from (3.90) into (3.91) gives the unloaded Q within the resonator as,

$$Q = \frac{\omega_o L}{Z_o} \tag{3.92}$$

Adding in external circuitry or a lossy material to the resonator has the effect of lowering the Q. In terms of the series resonant circuit, this can be represented by an addition of load resistance R_L to the transmission line model. However, if the resonator is matched to the transmission line then,

$$Q = \frac{\omega_o L}{(R + R_L)} = \frac{\omega L}{Z_o} \tag{3.93}$$

which implies that the loaded and unloaded Q of the resonator are equal under impedance match conditions. The resonator is said to be *critically coupled*.

3.3.9 Cavity Tuning

Degeneracy (or quasi-degeneracy if appropriate) can be forced by changing or tuning of the resonant frequency of a particular mode. This can be achieved through inclusion of small tuning screws or inclusion of material inserts within the volume of the cavity. In addition, it is also possible to change the physical shape of the cavity by utilising a movable conducting walls. These approaches can be described through a cavity perturbation technique where the resonant frequency of a mode is perturbed by some means. The perturbation method assumes that the fields of the perturbed cavity do not differ significantly from the field distribution of the unperturturbed cavity.

An alternative use for the cavity perturbation technique is in measuring of the material properties of an object within the cavity by observing the change in frequency between loaded and unloaded cavities. The dielectric constant of the material is calculated by measuring the shift in resonant frequency. The dielectric sample or object should be small in relation to the volume of the unloaded cavity for the perturbation method to be valid. Any increase in permittivity or permeability of an object or sample within the cavity will result in a reduction of the resonant frequency.

Tuning screws are the simplest and most flexible method of altering the resonant frequency of a mode within a waveguide cavity without significantly changing the field distribution. In effect, by altering the length of the screw, the user reduces the volume of the cavity and therefore causes a reduction in the resonant frequency of the design mode. The length of the screw should lie normal to the electric field and be located within an

electric field maximum for maximum perturbation to be achieved. If the screw were to be located tangential to the electric field or within an electric field null the perturbation effect would be minimised. (In theory, there would be no perturbation of the resonant frequency). The theory behind cavity shape perturbation is treated extensively in the literature [117], [119].

CHAPTER FOUR

DEGENERATE MODE HEATING: HYPERTHERMIA APPLICATOR

4.1 Introduction

This chapter describes a proposed hyperthermia treatment applicator based on degenerate mode summation within an *overmoded* resonant waveguide cavity resonator [120]. It is proposed that a *hot-spot* of electric field can be formed in the centre of the cavity volume, with minimal electric field at other locations, through proper selection of a combination of resonant cavity modes and through using the principle of constructive and destructive wave interference. Lossy materials placed within the electric field peak will experience higher degrees of heating compared to the same material placed within the electric field nulls (or areas with minimal electric field). Alignment of the electric field peak with the location of a tumour (or region containing cancerous cells) allows heating to be focussed with minimal heating of the surrounding healthy tissue.

A hypothesis is presented outlining the functionality of the oven. The design is based around excitation of a waveguide cavity resonator resulting in a heavily *overmoded* structure. The resonant modes should be degenerate (or at the very least, quasi degenerate), and of sufficient number and order to secure sufficient field enhancement at a single excitation frequency.

A mode interference model is presented and applied to the rectangular waveguide cavity. A number of amplitude variations are investigated. Theoretical mode distributions are compared to a practical mode set. The analysis is repeated for a cylindrical geometry.

4.2 Applicator Design and Implementation

A schematic of the proposed non-invasive cavity based on a focused hyperthermia system is shown in Figure 5. The patient will lie on an adjustable table, with the region of the body that requires treatment, enclosed within the cavity. For simplicity, a rectangular cavity has been suggested, however, cylindrically (Figure 5) or elliptically shaped cavities could equally be envisaged. The proposed cavity will be large enough to sustain a large number of high order modes, closely spaced in frequency. In order to force a selection of suitable modes to become degenerate, a certain amount of tuning may be required. This would be achieved by inserting metal tuning posts into the cavity thus reducing the volume causing a decrease the resonant frequency of the affected modes. On the other hand, placing small, non-radiating, slots in the cavity walls will have the effect of electrically enlarging the cavity, resulting in an increase in the resonant frequency of the affected modes.

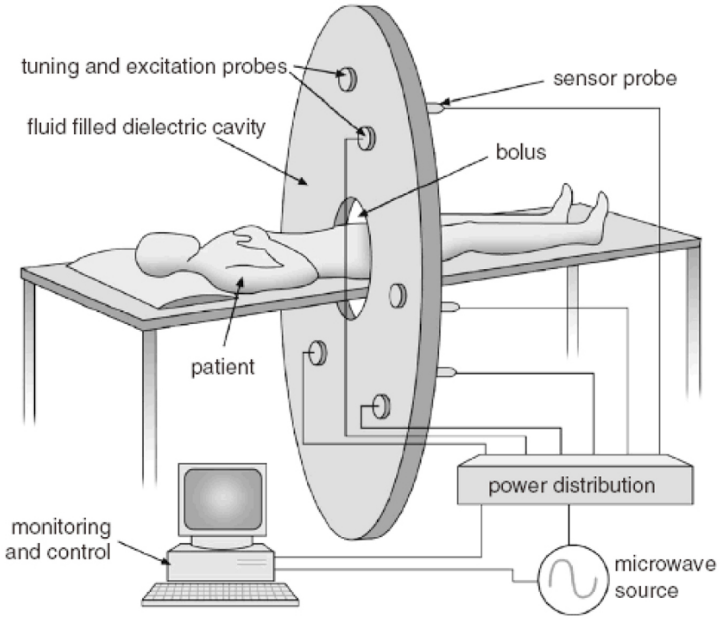

Figure 5: Schematic representation of the proposed hyperthermia system based on a degenerate mode / multimode fluid-filled system.

The amount of perturbation required is determined by the length and position of each tuning element. The location of the tuning elements will also determine which modes are perturbed. It is well known that placing a *capacitive* tuning element in the null of a electric field of the mode leads to minimal perturbation of the resonant frequency while placing such a tuning element in the field maxima of the pattern leads to maximum perturbation. By careful placement and tuning length selection, it is proposed that several modes can

be perturbed such that each is forced to become degenerate. By controlling the magnitudes and phases of these degenerate modes, constructive interaction between the modes can be developed such that maximum microwave power is delivered to the treatment area.

Coupling of power into the cavity will be made through either probe or loop feeds depending on whether TE modes or TM modes are required. Feed placement will also determine which modes are excited. Sampling probes placed at points within the cavity will allow for adaptive adjustment of the tuning element length and the amplitude and phase of the input signals controlled by the central processing unit (CPU).

A fluid filled bolus is required between the cavity and patient and serves two primary functions. Firstly, the bolus acts as protection from any increase in temperature of the skin surface. Water (or other suitable liquid) can be continually flushed though the bolus and can increase patient comfort [61], [80]. Secondly, the permittivity of the liquid should be chosen to match the average permittivity of the patient's treatment area. The total volume of the cavity will be filled with materials that are as homogeneous as possible with minimal variation in relative dielectric constant. If this requirement is not met then the body placed within the cavity will significantly perturb the resonant frequency of the mode set. If a uniform permittivity is assumed within the cavity volume then the perturbation will be minimised thus decreasing the requirement of complex simulation tools to enable the prediction in the change of individual mode resonance within the loaded cavity.

4.3 Definitions

It is proposed that a *hot-spot* or maxima of electric field can be formed in the centre of a multi-mode cavity through utilising the principle of constructive and destructive wave interference. By proper selection of the multiple modes within the cavity, it is suggested that the electric field will constructively interfere at the 'treatment region' while destructively interfering at all other regions. Through using higher order modes (defined as modes whose resonant frequency is very much higher than the fundamental mode), the maxima will tend to sharpen thus leading to higher selectivity and a minimisation of the electric field in the areas surrounding the hot-spot.

For simplicity, and in order to clearly illustrate the modal superposition process of the theoretical model, it is assumed that the selected modes are wholly degenerate at this

stage. That is, it is assumed that, by cavity perturbation, the selected modes could be made degenerate, although the theoretical cavity is unperturbed. Calculations have been carried out on both a rectangular waveguide cavity and a cylindrical cavity in order to investigate pattern superposition. The cavity sizes relate to operating frequencies in the MHz frequency range, and to cavities containing biological medium typically having relative permittivity of the order of $\varepsilon_r \approx 45$ and dielectric loss tangents of the order of $\tan\delta \approx 0.5$ at the frequencies of interest.

The specific absorption rate (SAR) is defined as the rate of energy absorption per unit mass and gives an indication of the amount of energy that is absorbed by a material or body and is expressed as watts per kilogram.

$$SAR = \frac{|E|^2\sigma}{\rho} \tag{4.1}$$

where E is the electric field, σ is the conductivity and ρ is the density of the medium. Two parameters are defined in order to analyse the theoretical results. A *minor lobe ratio*, $\mathrm{L_R}$ (dB), defines the selectivity of the electric field maxima and is calculated by taking the logarithmic ratio of the magnitude of the nearest off centre electric field peak and the magnitude of the centre electric field maxima.

$$\mathrm{L_R} = 20\log_{10}\left(\frac{|E_{lobe}|}{|E_{peak}|}\right) \tag{4.2}$$

$|E_{lobe}|$ and $|E_{peak}|$ are the magnitudes of the electric field of the principle lobe and peak, respectively. A *principal lobe width*, $\mathrm{L_W}$ (%), is defined in (4.3) and gives a means of comparing the width of the electric field maxima for a variety of theoretical results. The width of the peak is measured at the point where the magnitude of $|E_T|^2$ is 3dB less than the maximum value and is expressed as a percentage of the length of the cavity axis,

$$\mathrm{L_W} = \left(\frac{width(-3dB)}{d}\right)\% \tag{4.3}$$

where d is the length of the cavity axis.

4.4 Degenerate Mode Model: Theoretical Analysis for Rectangular Waveguide Cavity

4.4.1 Frequency Deviation within a Degenerate Mode Set

In order to illustrate the concept of the electric field *hot-spot* formation in a cavity using multiple degenerate modes, an initial analysis is presented which, for simplicity, makes use of the $l = 0$, TM$_{mnl}$ modes, within a rectangular waveguide cavity [120]. This simplification is convenient but not necessary. Since there is no standing wave variation in the z direction ($l = 0$), the electric field will takes the form of a *column* of constant field intensity along the z-axis while varying sinusoidally in the x and y directions according to the boundary conditions set out in Chapter 3.

Consider a multiple number of orthogonal TM$_{mn0}$ modes within a lossless rectangular cavity where m and n are odd integers and $m = n$. The electric field component E_z within rectangular waveguide (3.47) for this mode set is,

$$E_{z_{mn0}} = B_{mn0} e^{j\phi_{mn0}} \sin\frac{m\pi x}{a} \sin\frac{n\pi y}{b} e^{j\omega_{mn0}t} \tag{4.4}$$

where a and b denote the dimensions of the cavity in the x and y directions respectively. B_{mn0} and ϕ_{mn0} represent the magnitude and phase of the TM$_{mn0}$ mode while ω_{mn0} is the modal resonant frequency. For modes in a rectangular cavity, the resonant frequency is determined from,

$$\varepsilon_r k_o^2 = \left(\frac{m\pi}{a}\right)^2 + \left(\frac{n\pi}{b}\right)^2 + \left(\frac{l\pi}{d}\right)^2 \tag{4.5}$$

For the TM$_{mn0}$ modes and for a cavity for which $a = b$, mode degeneracy requires,

$$m^2 + n^2 = H \tag{4.6}$$

where H is a constant. Therefore, for modes to be degenerate within the cavity then,

$$n = \sqrt{H - m^2} \tag{4.7}$$

The total z-directed electric field distribution within the cavity for N modes can be expressed as,

$$|E_T| = \sum_{m=1}^{N} B_{mn0} \sin \frac{m\pi x}{a} \sin \frac{\pi y \sqrt{H - m^2}}{a} e^{j\omega t} e^{j\phi} \tag{4.8}$$

If all the N modes are degenerate (all ω values are equal) and excited in phase (all ϕ values the same), (4.8) reduces to,

$$|E_T| = \sum_{m=1}^{N} B_{mn0} \sin \frac{m\pi x}{a} \sin \frac{\pi y \sqrt{H - m^2}}{a} \tag{4.9}$$

At the centre of the cavity where $x = a/2$ and $y = b/2$, this implies,

$$|E_T| = \left(\sum_{m=1}^{N} B_{mn0} \right)^2 \tag{4.10}$$

This applies only for the odd values of m and n. For a low height, square cavity, designed to resonate in the $TM_{19,19,0}$ mode (for example), (4.6) and (4.7) demonstrate the extent to which nearby odd-order modes deviate from degeneracy with the $TM_{19,19,0}$ mode. The results are tabulated in Table 1, where $n^{'} = \sqrt{722 - m^2}$. The table indicates that quite moderate levels of selective tuning will be sufficient to make most of these modes fully degenerate, although this is only necessary in very high Q cavities. The simple analysis presented within this section describes the magnitude of the electric field in the centre of the x-y plane. At this location, the squared total of the z-directed electric field is simply the sum of the amplitudes of the odd modes in the selected range of modes. The maximum value of the squared electric field magnitude is used in the normalisation of the field patterns.

4.4.2 Quality Factor and Degeneracy

If a very high Q cavity is assumed then it is likely that individual modes will require moderate amounts of tuning in order to allow for the degenerate heating effect. The resonant *dip* within the Q-curve (frequency response) of a mode within a high Q structure has a

Table 1: High order mode degeneracy.

m	n'	n	**Frequency Deviation %**
9	25.318	25	-1.1142
11	24.515	25	1.6485
13	23.516	23	-1.6761
15	22.294	23	2.1920
17	20.809	21	0.5525
19	19.000	19	0
21	16.763	17	0.5525
23	13.892	13	-1.6761
25	9.8490	9	-1.1142

very narrow bandwidth resulting in a steep or sharp frequency gradient. Coupling to the desired mode occurs over a short range of frequencies reducing the likelihood of coupling to nearby modes with similar resonant frequencies. As the Q of the resonant mode reduces, the width of the frequency response widens to encompasses a greater range of frequencies. In this case, nearby modes can now be loosley coupled into the cavity with the weighting of the quasi degenerate mode being determined by the level of coupling. Within the lower Q cavity, the ability of the resonant structure to store energy is reduced as the attenuation of energy with time increases [according to (3.88)]. Sufficiently low levels of Q may ensure the mode set described in Table 1 is quasi degenerate.

The principle of quasi degeneracy is demonstrated using a full-wave simulation solver (HFSS) on a cavity whose cross section is nearly square. A *driven solution* is used within the solver which allows for the input impedance and scattering parameters to be solved at a user-defined port with incident wave power of 1W. In addition, an *eigen solver* solution enables the eigenfrequencies and eigenmodes to be solved for a resoannt structure. Perturbing the shape of the cavity has the effect of separating the orthogonal modes that would be naturally degenerate for the cavity with square cross-section. A similar effect could be achieved through inclusion of a tuning screw located on one side wall within the square cavity. The orientation of the screw should be such that modes whose electric field is locate longitudinally to the length of the screw will be perturbed with adjustments to the length of the tuning screw. The degree of perturbation is increased as the screw is inserted further into the cavity volume.

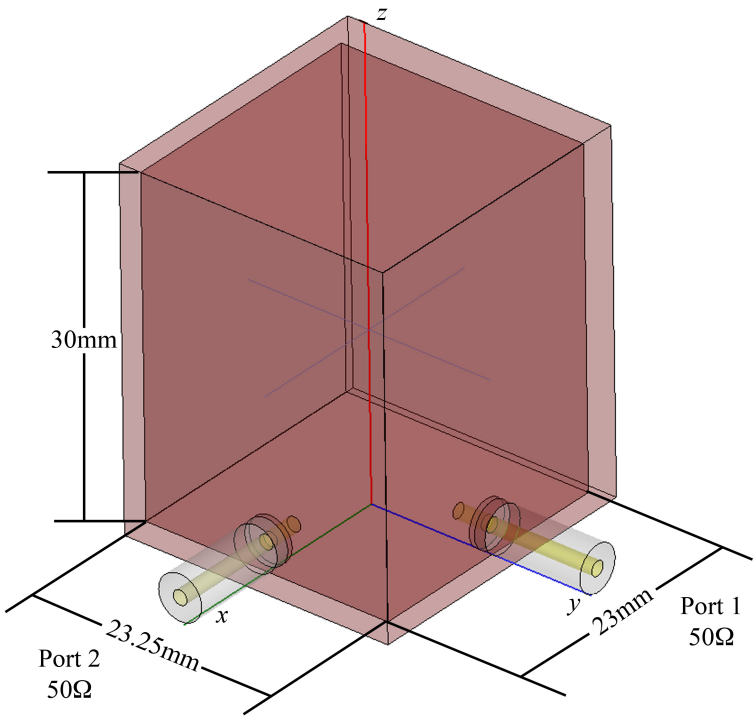

Figure 6: Schematic of two port quasi degenerate cavity.

Figure 6 displays the layout of the *almost* square cavity. The inner dimensions are 23mm x 23.25mm x 30mm with the cavity fully filled with a material with a fictitious dielectric constant of 3. The outer material is brass with a conductivity σ of $15\text{x}10^6$S/m. Two coupling probes are placed adjacent to each other such that both the TE_{101} and TE_{011} modes can be independently coupled into the cavity at their respective resonant frequency. Coupling of each mode is achieved through the use of the coaxial coupling probe. Each probe consists of a circular length of teflon ($\varepsilon_r = 2.2$) with diameter of 4.1mm and an inner conductor consisting of gold with diameter of 1.3mm. The dimensions and properties equate to a characteristic impedance of 50Ω. Port 1 is located within the centre of the y axis and is 13mm below the mid-point of the cavity through the z axis. Likewise, Port 2 is located within the centre of the x axis. The length of the central conductor protruding into the cavity interior has been optimised to give equal coupling of the modes. The structure is simulated with the *driven solution* within HFSS using a mesh size of approximately 10,000 tetrahedra.

In order to observe degeneracy, two values of tan δ are simulated (Table 2) within the HFSS design environment. The *lower* loss material has a loss tangent of $5\text{x}10^{-5}$ while the *high* loss material has a loss tangent of $5\text{x}10^{-3}$. The frequency response of the cavity, having been connected to a matched power splitter, is shown in Figure 7. Power

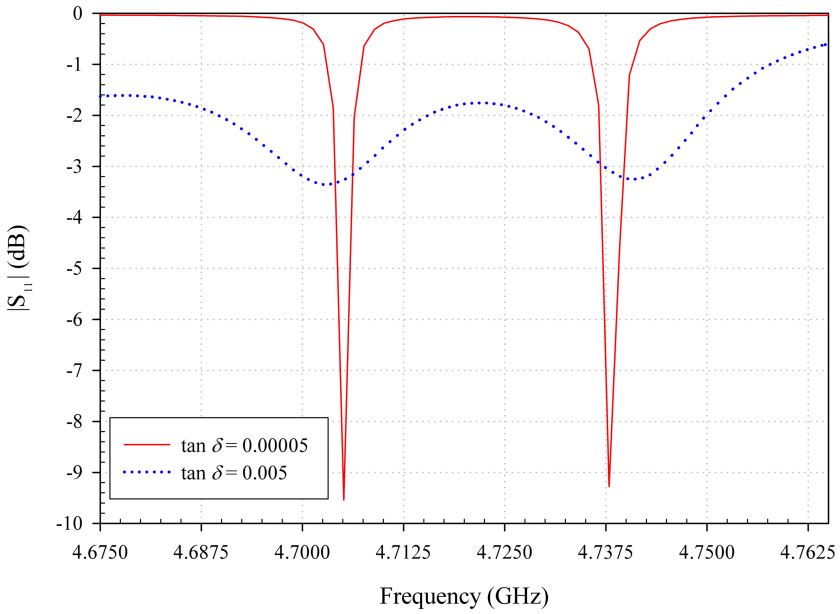

Figure 7: Frequency response of the two port cavity with low (tan $\delta = 5\text{x}10^{-5}$) and high (tan $\delta = 5\text{x}10^{-3}$) loss filling materials, fed from a matched T-junction power divider.

Table 2: Simulated (HFSS) Quality Factor for the TE_{101} and TE_{011} modes.

tan δ	**Q_{101}**	**Q_{011}**
$5\text{x}10^{-5}$	3499.0	3502.2
$5\text{x}10^{-3}$	183.4	183.7

incident at the input of the splitter is evenly distributed to Ports 1 and 2 of the cavity. The magnitude of S_{11} at the splitter input versus frequency gives an indication as to how the coupling from feed line into the cavity varies with frequency (and for each resonant mode). The coupling probes located on the cavity walls are optimised using HFSS such that maximum coupling is achieved at the TE_{101} and TE_{011} resonant frequencies. The coupling probes have equal length and extend 2.6mm into the cavity. Table 2 shows the simulated Q, calculated using (3.87), for both the *low* and *high* loss cavities and for each mode. Q for both the TE_{101} and TE_{011} modes reduces from approximately 3500 to 183 as the loss is increased. This corresponds to a *widening* of the Q-curve response for each mode, as suggested within Figure 8.

For the low $\tan\delta$ material, it is observed from Figure 7 that the TE_{101} mode is resonant at 4.707GHz with $|S_{11}| = -9.8$dB. The TE_{011} is resonant at 4.7375GHz with $|S_{11}| = -9.4$dB. Alternatively, for the high $\tan\delta$ material, the TE_{101} mode is resonant at 4.705GHz with $|S_{11}| = -3.3$dB. The TE_{011} is resonant at 4.374GHz with $|S_{11}| =$

-3.3dB. Further tuning of each modal resonant frequency would allow for further refinement and enhancement of the impedance matching between cavity and feed line resulting in lower values of $|S_{11}|$. In addition, stub tuning on the feed line would also serve as a means of controlling the impedance matching and level of coupling.

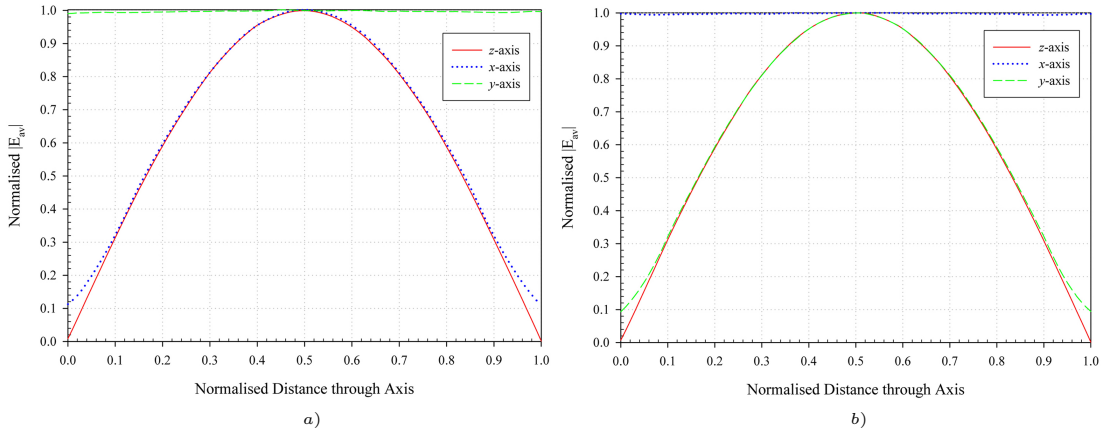

Figure 8: Normalised electric field [complex] magnitude within a low loss cavity through the x, y and z axis for a) the TE$_{101}$ and b) TE$_{011}$ modes, respectively.

The normalised electric field magnitude through the x, y and z-axis is shown within Figure 8, Figure 9 and Figure 10 for the *lower* loss and the *high* loss cavities. Figure 8a displays the normalised electric field magnitude for the TE$_{101}$ mode within the *low* loss cavity. As expected, a well defined TE$_{101}$ mode pattern is produced where the electric field varies sinusoidally through both the x-axis and z-axis while remaining constant through the y-axis. The normalised magnitude is at a maximum at the centre of the x-z plane. Figure 8b shows a similar relationship for the TE$_{101}$ except that the electric field in constant through the x-axis and varies sinusoidally through the y-z plane. Figure 11 displays the electric field distribution of the TE$_{101}$ and TE$_{011}$ modes, respectively.

Similar plots for the *high* loss cavity are shown in Figure 9. Degradation of the field pattern can be observed as compared to the *lower* loss cavity plots. Figure 9a displays the normalised field distribution for the TE$_{101}$ mode at resonance. The electric field magnitude through the y-axis is approximately uniform but decreases towards the outer area of the cavity. This is due to weak coupling of the TE$_{011}$ mode at the resonant frequency of the TE$_{101}$ mode. This *degradation* of the electric field pattern of the TE$_{101}$ mode could be increased by either, increasing the loss of the filling material within the cavity volume or by perturbing the shape of the cavity such that the resonant frequency of the weakly coupled TE$_{011}$ mode becomes *closer* to TE$_{101}$ mode resonant frequency. A similar effect is observed for the TE$_{011}$ mode within Figure 9b. In this case, the electric field pattern is

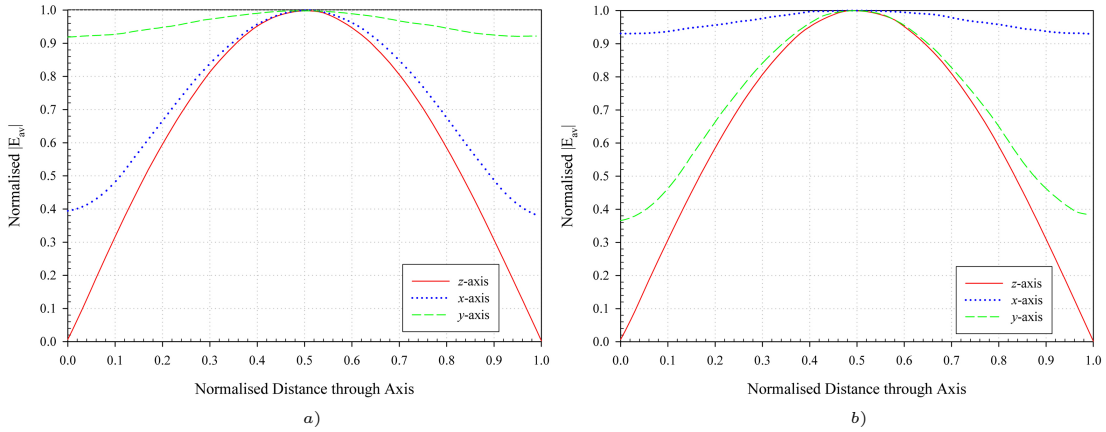

Figure 9: Normalised electric field [complex] magnitude within a high loss cavity through the x, y and z axis for the TE_{101} [left] and TE_{011} [right] modes, respectively.

perturbed through the [now] weakly coupled TE_{101} mode.

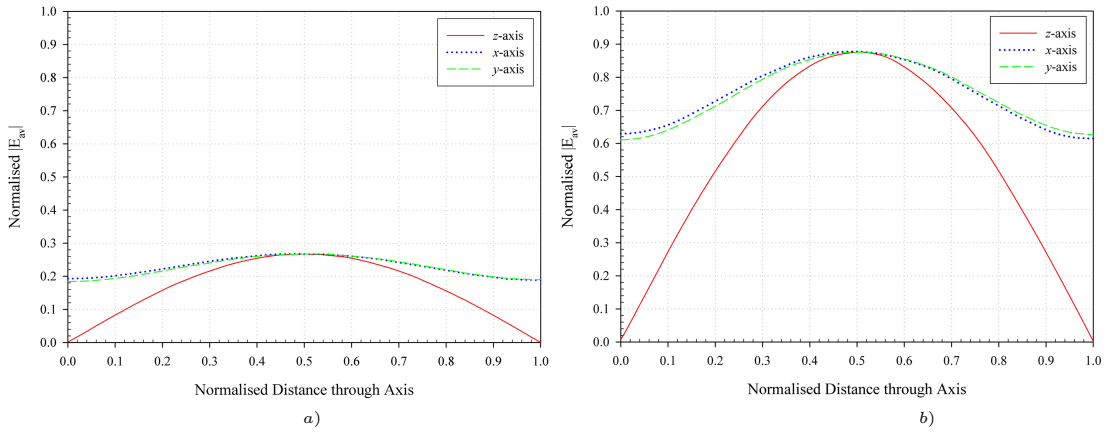

Figure 10: Normalised electric field [complex] magnitude of the quasi degenerate TE_{101} and TE_{011} modes through the x, y and z axis for $a)$ tan $\delta = 5\text{x}10^{-5}$ and $b)$ tan $\delta = 5\text{x}10^{-3}$, respectively.

Figure 10 displays the normalised electric field pattern through each axis when the cavity is excited at 4.722GHz. This corresponds to the mid-way point between each resonant mode ensuring both modes are equally coupled into the cavity. The *low* loss case is displayed in Figure 10a with the electric field magnitude normalised to the maximum magnitude of the TE_{101} mode. (It is assumed that, since the coupling of the TE_{101} and TE_{011} modes are approximately equal, the maximum magnitude of the electric field at the respective resonant frequencies can also be considered approximately equal). The field pattern is a summation of both the TE_{101} and TE_{011} modes. The electric field magnitude through the x-axis and y-axis are approximately equal suggesting that, not only is the assumption above valid, but that the fields are quasi degenerate. However, the maximum magnitude within the centre of the cavity is 0.28 indicating poor coupling of each mode.

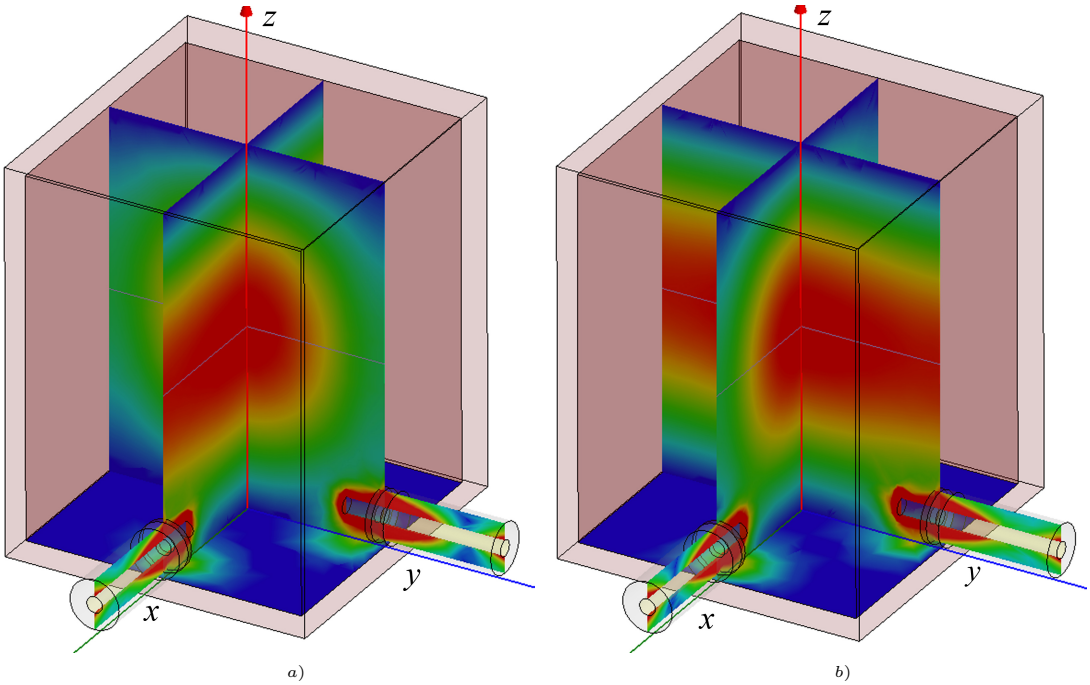

Figure 11: Electric field distribution of the a) TE_{101} and b) TE_{011} modes, respectively.

Figure 7 confirms that this is the case as $|S_{11}| = -0.2$dB at 4.722GHz.

Improved quasi degenerate coupling is achieved within the *high* loss cavity. For this example, $|S_{11}| = -1.8$dB at 4.722GHz. Figure 10b shows the electric field magnitude through the x-axis and y-axis is approximately equal and that the maximum normalised magnitude is approximately 0.85 indicating improved coupling into the cavity. The magnitude of the electric field distribution is displayed in Figure 12.

4.4.3 Computational Predictions

Figure 13 displays $|E_T|^2$ for the summation of the odd mode resonances where $N = 3$. The TM_{110} and TM_{330} modes within a rectangular cavity with dimensions 200cm x 200cm x 10cm are added in phase. Each mode has an amplitude equal to unity. $|E_T|^2$ is normalised to the amplitude of the lowest resonance (in this case, the TM_{110} mode). As predicted by the degenerate mode model, the electric field of each mode constructively interferes in the centre of the x-y plane $(x = y = a/2)$ since a maxima in the electric field of each mode exists at this point. Four side lobes are observed with each with a L_R of -3.94dB. These off-centre peaks exist due to the contribution of the TM_{330} mode off-centre maxima. L_W for the summed modes is 22.75%.

As more odd mode resonances are included within the model, the main peak tends to

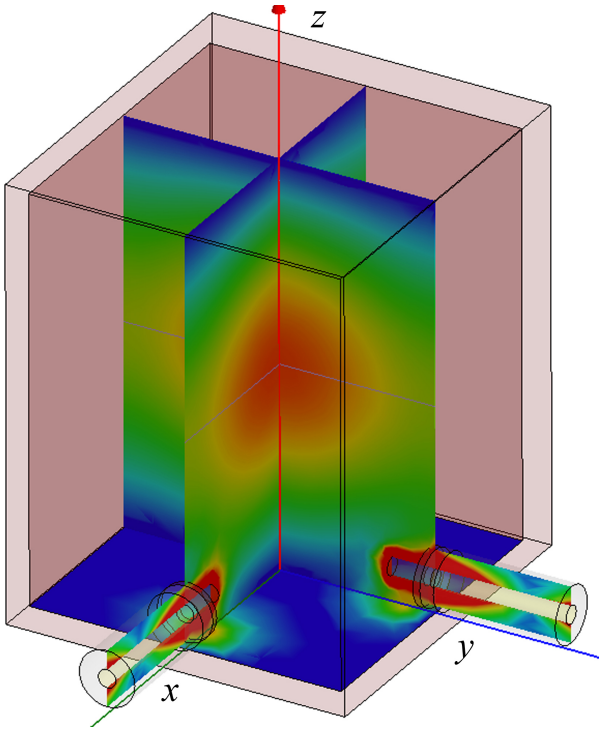

Figure 12: Electric field distribution of the quasi degenerate TE_{101}-TE_{011} mode.

sharpen, as displayed in Figure 14. However, L_R remains relatively constant at -5dB. Table 3 contains L_R and L_W for a number of odd mode summations starting from the fundamental TM_{110} mode.

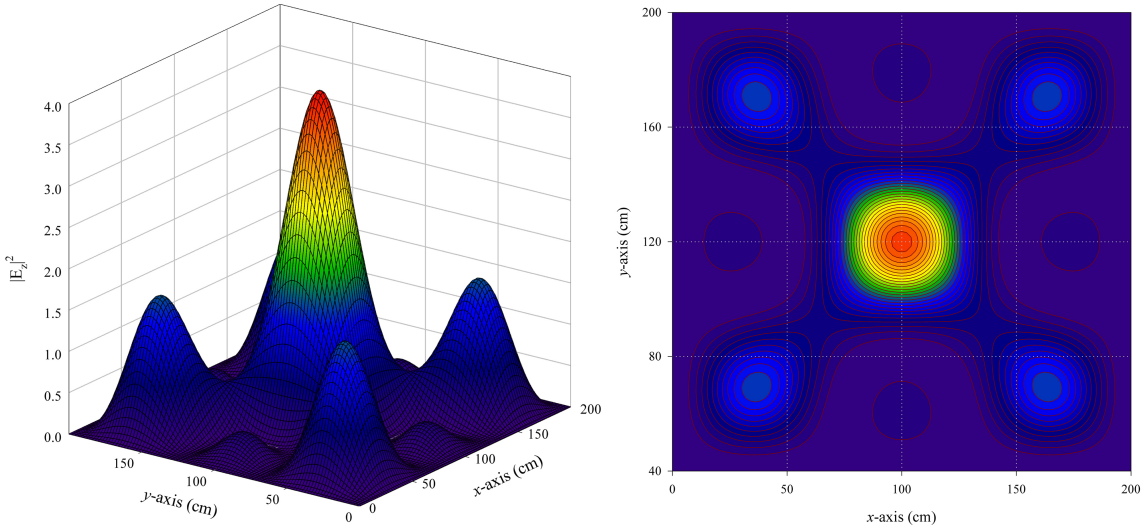

Figure 13: $|E_T|^2 = (E_{z_{110}} + E_{z_{330}})^2$.

The modes considered, so far, have equal amplitude weighting. Figure 15 displays the field patterns for four mode sets. Only the first quarter of the x-y diagonal has been plotted in order to focus on the central peak and the first minor lobe of the normalised electric field distribution. It is observed that L_R does not increase significantly through adding

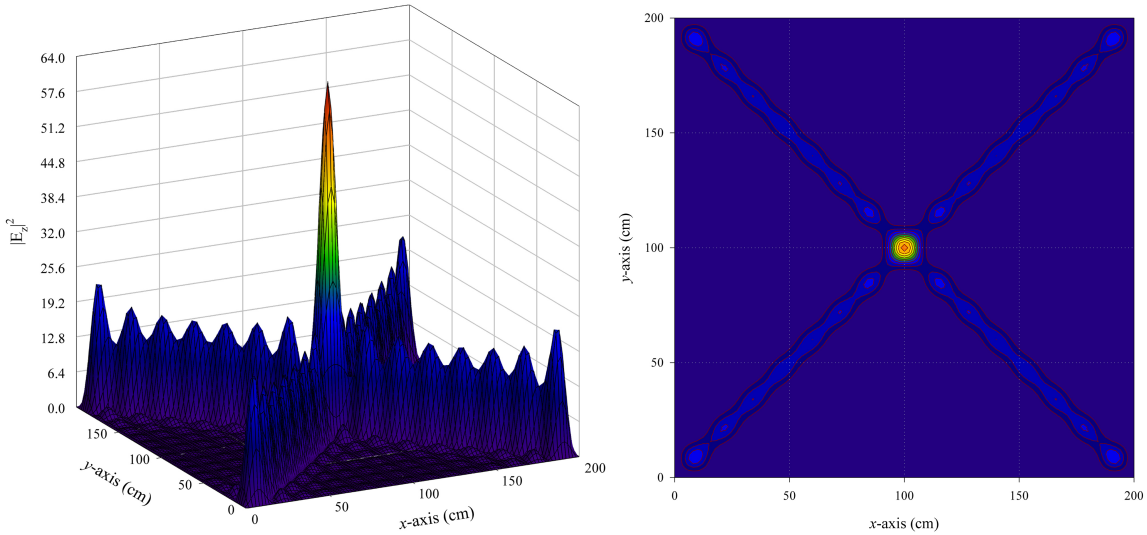

Figure 14: $|E_z|^2$ odd mode summation for TM_{101} to $TM_{15,15,0}$.

additional odd order modes to the summation. By comparison, L_W decreases suggesting a sharper electric field *hot-spot* in the centre of the cavity. This is not unlike radiation pattern behaviour for a uniform array antenna. An improvement in both L_R and L_W can be observed through removing a number of the lower order modes from the summations. Analysis of the normalised electric field distribution of the odd mode summation from TM_{550} to $TM_{15,15,0}$ shows $L_R = -5.91$dB and $L_W = 3.74\%$ compared to the TM_{110} to $TM_{15,15,0}$ summation with $L_R = -4.95$dB and $L_W = 4.36\%$. Analysis of the odd mode summation of $TM_{11,11,0}$ to $TM_{41,41,0}$ gives $L_R = -5.95$dB and $L_W = 1.69\%$ compared to $L_R = -4.97$dB and $L_W = 1.82\%$ for the TM_{110} to $TM_{15,15,0}$ summation.

Table 3: Theoretical results from odd mode summation.

Highest Order TM Mode	**Main Peak Amplitude**	**L_R (dB)**	**L_W (%)**
3,3,0	4	-3.93	17.20
15,15,0	64	-4.95	4.36
21,21,0	121	-4.96	3.24
31,31,0	256	-4.96	2.32
41,41,0	441	-4.97	1.82
51,51,0	676	-4.96	1.50

Other results, which have been obtained by the addition of odd order TM mode field patterns starting from the fundamental TM_{110} mode (Table 3), indicate a lack of improve-

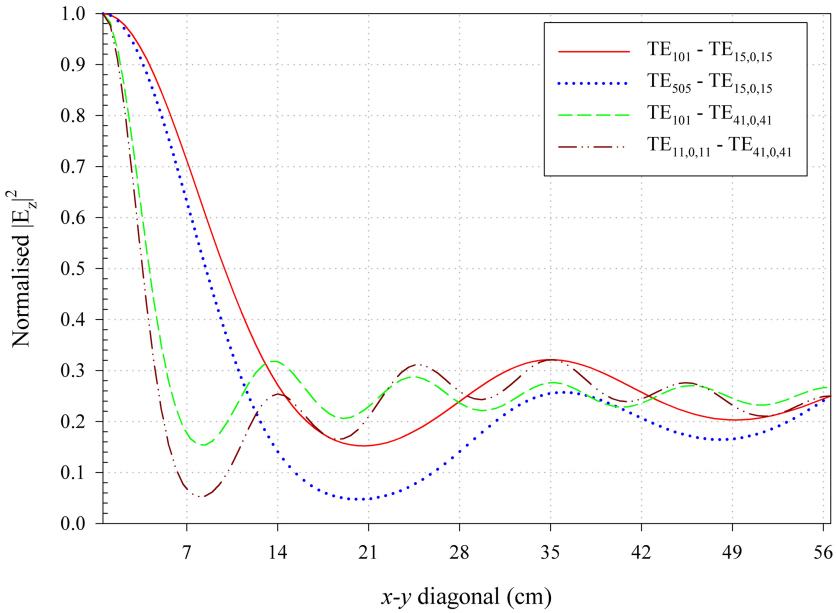

Figure 15: $|E_z|^2$ odd mode summation for constant distribution.

ment in selectivity as the number of modes is increased.

For very higher order modes, L_R tends towards a fixed value of -4.96dB. L_W continues to diminish as additional modes are introduced. Summation of the TM_{110} to $TM_{51,51,0}$ (25 odd modes) leads to $L_W = 1.5\%$. In a 200cm x 200cm x 10cm cavity, this represents a 3cm x 3cm *hot-spot* of electric field.

4.4.4 Amplitude Tapering

In practice it is unlikely that degenerate modes within a given mode set will have equal weighting. This is due to uneven or differing coupling levels for each resonant mode in the cavity. The amount of coupling from the source transmission line directly determines the magnitude of peak electric field within the cavity. Adjustment of the coupling for a probe feeds allows for a degree of weighting of each mode excited within the volume. Therefore, a weighting distribution (amplitude variation) of the mode set can be defined.

Three amplitude variations have been considered based around well-known distributions namely a *linear ramp*, a *sinc function*, and an *exponential decay*. Table 4 shows the relative amplitudes of each mode for the three distributions. For each distribution, electric field patterns have been generated. These represent the summation of all the odd modes from the TM_{110} mode to the $TM_{15,15,0}$ mode. The results are displayed in Figure 16 and are compared with the pattern generated by employing equally weighted modes. The pre-

sentations are produced by taking a diagonal cut through the x-y plane where the minor lobe ratio is at a minimum. The distribution is then normalised to the magnitude of the principal field maximum and is plotted from the centre of the cavity.

Table 4: Various amplitude distributions.

TM Mode	**Ramp Distribution**	**sinc x Distribution $0 \leq x \leq \pi$**	**Exponential Distribution**
1,1,0	0.875	0.974	0.687
3,3,0	0.750	0.900	0.472
5,5,0	0.625	0.784	0.325
7,7,0	0.500	0.637	0.223
9,0,9	0.375	0.471	0.153
11,11,0	0.250	0.300	0.105
13,13,0	0.125	0.139	0.072
15,15,0	0.000	0.000	0.049

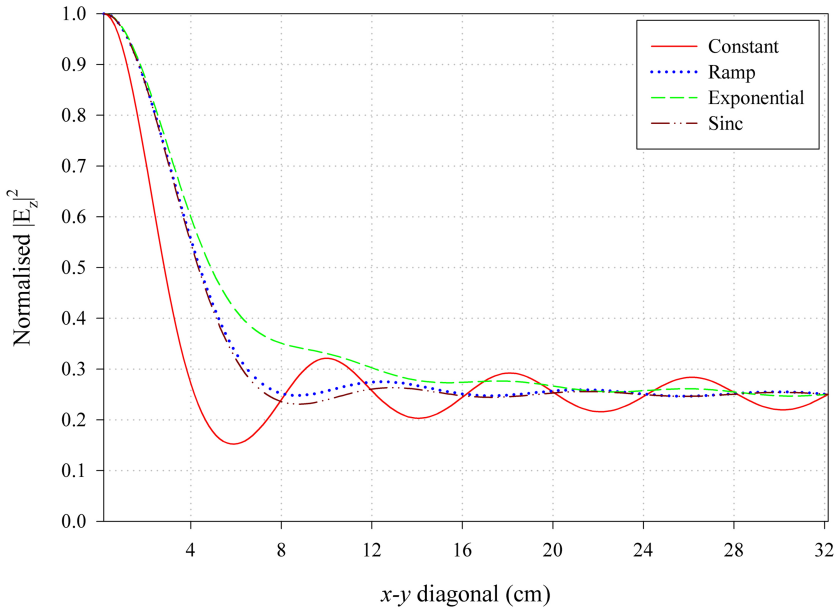

Figure 16: Electric field through the x-y diagonal for four amplitude distributions.

The electric field distributions through the x-y diagonal for the *ramp* and *sinc* functions share the same characteristics due to similar amplitude coefficients. The widest peak is produced by the decaying *exponential* function followed by the *ramp* and *sinc* functions and finally the *constant* distribution. This would be expected as, in each distribution,

the higher order modes contribute a progressively heavier weighting to the total distribution. The *ramp* function, the *sinc* function and the decaying *exponential* function produce relatively flat minor lobes as compared to the *constant* distribution. The *ramp* function $\mathrm{L_R} = -5.6$dB compared to $\mathrm{L_R} = -4.95$dB for the *constant* function. For the decaying *exponential* function $\mathrm{L_R} = -5.59$dB. For the *sinc* function, $\mathrm{L_R} = -5.80$dB showing a small improvement when compared to the other amplitude distributions. As the higher order modes contribute less to the overall field pattern summation for the *ramp* and *sinc* distribution (and in particular the decaying *exponential* distribution), $\mathrm{L_W}$ is larger for these distributions when compared to the *constant* distribution. The major features in the above paragraph have been summarised in the Table 5.

Table 5: Results relating to the amplitude distributions.

Amplitude Distribution	$\mathbf{L_R}$ (dB)	$\mathbf{L_W}$ (%)
Constant	-4.95	4.36
Ramp	-5.61	6.8
Sinc	-5.80	6.73
Exponential	-5.59	7.48

4.4.5 Non-Degenerate Mode Scintillation

It has been assumed that the mode sets within Section 4.4.3 are fully degenerate. In the absence of perfect degeneracy, the amplitude of each mode within the summation, will vary sinusoidally through its period. Within the following analysis, the amplitude of each mode is allowed to vary according to $e^{j\omega_i t}$ where ω_i describes the angular frequency of the mode. The modes under consideration has been assumed to be equally coupled in phase within a cavity with dimensions 200cm x 200cm x 10cm. The cavity is fully filled with a lossless material with a dielectric constant of 51. The resonant frequency of each mode is given in Table 6.

It can be clearly seen in Table 6 that the angular frequency of the $\mathrm{TM}_{15,15,0}$ is fifteen times greater than the angular frequency of the lowest order mode (the TM_{110} mode). Therefore, the $\mathrm{TM}_{15,15,0}$ mode will have oscillated fifteen times for every oscillation of the TM_{110} mode. Figure 17 describe the behaviour of the electric field distribution within the cavity over one quarter of the lowest order modes period. (There is no need to model

Table 6: TM_{mn0} mode data.

TM Mode	Resonant Frequency (GHz)	Angular Frequency ($rads^{-1}$)	Multiples of ω_o
110	0.0148	0.0932	1
330	0.0445	0.2797	3
550	0.0742	0.4662	5
770	0.1039	0.6527	7
990	0.1336	0.8392	9
11,11,0	0.1633	1.0258	11
13,13,0	0.1929	1.2123	13
15,15,0	0.2226	1.3988	15

the whole period since the results for the second half of the lowest order modes period are symmetrical).

Figure 17 displays the electric field distribution over one quarter of TM_{110} mode period. The main peak only exists at $t = T/4$ (it will also exist during the negative half of the cycle). During the first quarter of TM_{110} period, four smaller electric field peaks can be seen to combine to give the main peak at $t = T/4$. The normalised magnitude of these peaks is equal to approximately 0.25. During the second quarter of the T_{101} the peaks move apart. This process is repeated during the third and fourth quarters.

4.4.6 Mode Degeneracy within a Rectangular Cavity

In Section 4.4.1, the proposed principle of modal superposition in high order mode cavities is based on mode sets having been assumed to be fully degenerate without giving any consideration as to whether or not the constituent modes in each set could actually be made degenerate. It is clear that in practice, to achieve multi-mode degeneracy in a high order mode cavity, modes that are naturally, or almost naturally, degenerate must be chosen as tuning of modes over tens of the percent of the un-tuned centre frequency is not possible. Low order mode resonances in a rectangular cavity can be tuned, using conventional tuning techniques such as an electric field probe, over a typical range of approximately 5% of the resonant frequency. Consequently, choosing modes that have resonances that are naturally degenerate, or almost naturally degenerate, will ensure that

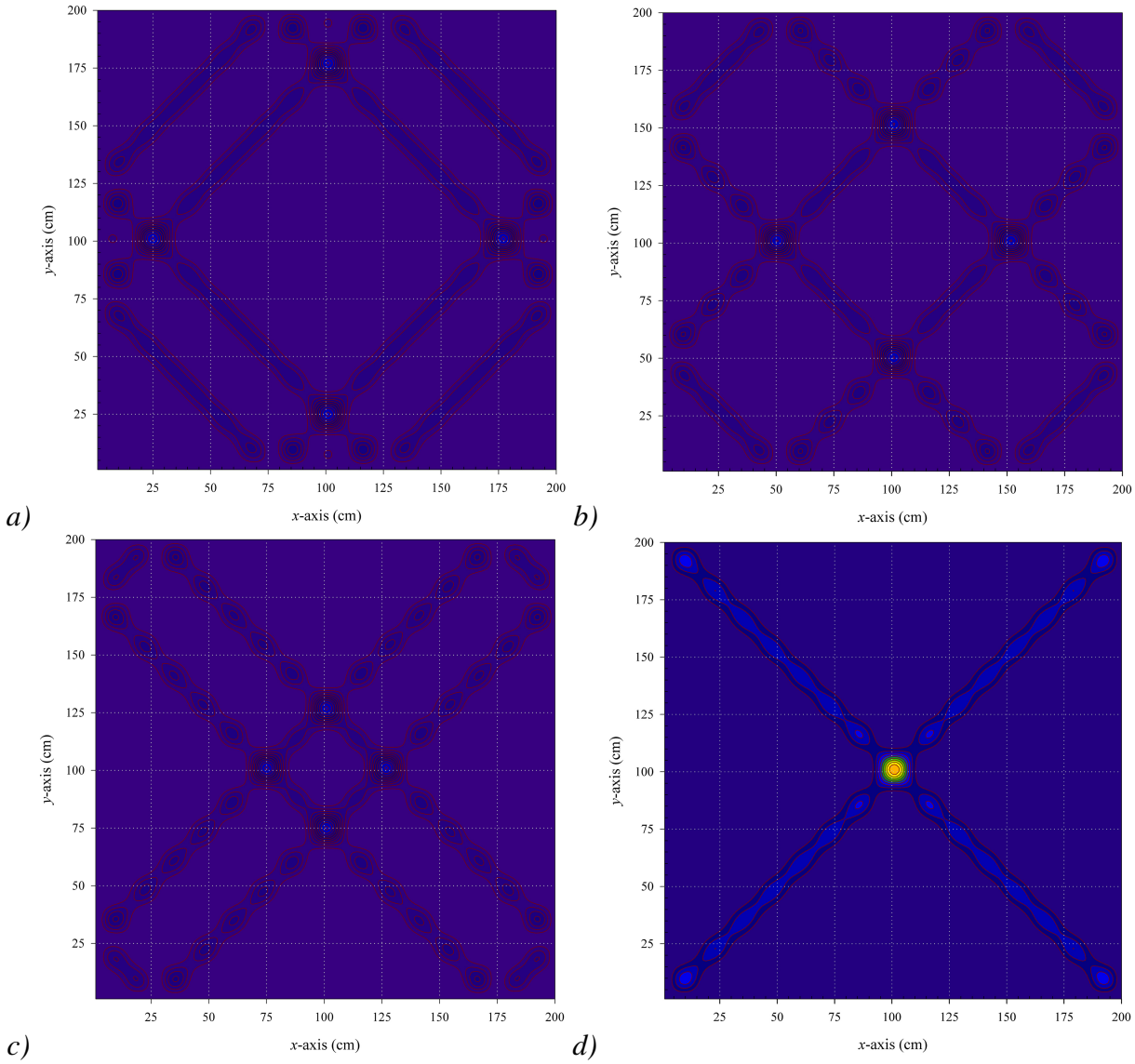

Figure 17: Plots showing electric field distribution for (a) $t = \frac{1}{16}T_{101}$*, (b)* $t = \frac{1}{8}T_{101}$*, (c)* $t = \frac{3}{16}T_{101}$ *and (d)* $t = \frac{1}{4}T_{101}$*.*

the degree of tuning [if required] will be within practical limits.

As indicated earlier it is also known that, to procure significant levels of modal field superposition, a high degree of degeneracy is only required in very high Q cavity systems. In practical systems the cavity Q may be quite low (e.g. in a hyperthermia application) and therefore quasi-degeneracy may be adequate to secure field enhancement through modal superposition. Both of these requirements will dictate that a practical system need not be overly complex structurally, and hence unrealisable.

Fifty nine resonances exist within a possible hyperthermia cavity filled with a low-loss material ($\varepsilon_r = 51$) having the dimensions 200cm x 200cm x 10cm when operated over a frequency range of 338.8MHz to 342.7MHz. The cavity is heavily *overmoded*, but more

importantly, a large number are degenerate or are almost degenerate. The majority of these modes have been discarded as, at this stage, the analysis has been restricted to the examination of field focusing using TM_{mn0} modes only. This modal limitation can be achieved by restricting the length of the cavity and also through the proper placement of suitable modal feed arrangements within the cavity.

Seven potentially degenerate modes within the low height rectangular cavity have been selected and summed together in order to investigate *hot-spot* formation with this more practical mode set. The chosen modes are listed in Table 7, along with their respective resonant frequencies. $TM_{9,31,0}$ / $TM_{31,9,0}$ and $TM_{15,29,0}$/ $TM_{29,15,0}$ / $TM_{21,25,0}$ / $TM_{25,21,0}$ can be seen to be naturally degenerate.

Figure 9 displays the normalised squared electric field magnitude as a function of distance along the x-axis, the y-axis, and the primary diagonal, with the distance being measured from the centre of the cavity. As expected the plots are symmetrical about the cavity centre. The significant feature of these plots is the presence of a second order peak on each axis at approximately 12cm from the cavity centre. These occur, for very high order modal summations, wherever significant constructive field build up occurs, in a manner not too dissimilar to the formation of secondary lobes or grating lobes in antenna array theory.

Table 7: TM_{mn0} resonances for a practical mode set.

TM Mode	**Resonant Frequency (GHz)**
31,9,0	0.3388
9,31,0	0.3388
23,23,0	0.3414
29,15,0	0.3427
15,29,0	0.3427
21,25,0	0.3427
25,21,0	0.3427

The irregularity of the patterns on the x-axis and y-axis, and the marked similarities between them, reflects the irregularity of the modal sequences in this limited quasi-

degenerate mode set. The selected modes exhibit 9, 15, 21, 23, 25, 29 and 31 half cycles variations within the width and height of the cavity, and no variation through its length. It is these modal sequence differences that are the source of the observed differences in the patterns. This seven mode set produces a L_W of 3% and an L_R of -4.1dB.

Amplitude tapering was also performed on this particular example. However, the results did not improve on the performance of the *constant* amplitude example, with the secondary peaks on each axis increasing by approximately 0.67dB on the x/y-axis and 0.87dB on the diagonal axis relative to the *constant* amplitude case, when a *ramp* taper was introduced. The other amplitude tapers considered produced worse results when compared to the *ramp* taper. The L_W of each taper remained constant with no identifiable influence observed.

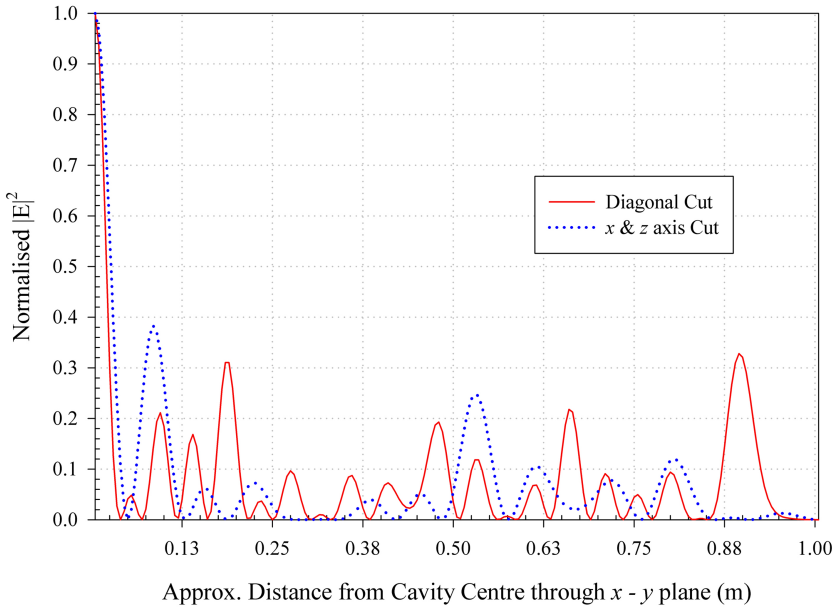

Figure 18: Normailsed $|E|^2$ through x-axis, y-axis and diagonal axis from centre of cavity $x-y$ plane.

4.4.7 Theoretical Results for Cylindrical Disc Resonator

An analysis, similar to that which has been applied to the square cavity, has been applied to a quasi degenerate sequence of cylindrical waveguide modes in a low height disc resonator. At this stage only TM_{0mq} modes have been analysed as these modes conveniently support an electric field peak along the axis of the cavity. Consider a multiple number of TM_{0mq} modes where m and q can be any integer. Here m represents the number of half cycle variations along the ρ-axis while q represents the number of half sinusoidal

variations along the z-axis. For a low height disc cavity q is unlikely to have a value of greater than 6. For the purpose of this theoretical analysis, all TM modes are assumed to be excited with equal amplitude. The electric field components E_z and E_ρ of a TM mode in a cylindrical cavity resonator are given in (3.59) and (3.60) respectively. For the TM_{0mq}, (3.59) and (3.60) reduce too,

$$E_z = A_{0mq} J_0(k_c \rho) \cos\left(\frac{qz\pi}{h}\right) e^{j\omega_{0mq}t} \tag{4.11}$$

$$E_\rho = -\frac{j\beta}{k_c} A_{0mq} J_0'(k_c \rho) \sin\left(\frac{qz\pi}{h}\right) e^{j\omega_{0mq}t} \tag{4.12}$$

where $k_c = p_{0m}/a$, $\beta = \sqrt{(}k_o^2 - k_c^2)$ and $m = 1, 2, \cdots \infty$. p_{0m} represents the m^{th} zero of the Bessel function J_0 of the first kind of order zero, and A is a field amplitude constant. The cylindrical cavity under consideration has dimensions $a = 100$cm and $h = 10$cm.

The total electric field in the cavity is given by,

$$|E_{res}| = \sqrt{E_\rho^2 + E_z^2} \tag{4.13}$$

$|E_{res}|^2$ is plotted in the following figures. As with the rectangular cavity analysis, a number of theoretical results are presented each with additional higher order modes $n >> 1$ included in the summation in order to assess the field focusing potential of the process of adding together the degenerate modes. The modes analysed in the degenerate mode simulation are given in Table 8. The cavity is filled with a dielectric constant $\varepsilon_r = 51$.

Table 8: High order mode degeneracy for cylindrical cavity.

m	***n***	***q***	**Resonant Frequency (GHz)**	**Frequency Deviation (%)**
0	10	6	1.2759	0.00
0	14	6	1.2921	1.2669
0	18	6	1.3134	2.9368
0	22	6	1.3396	4.9933

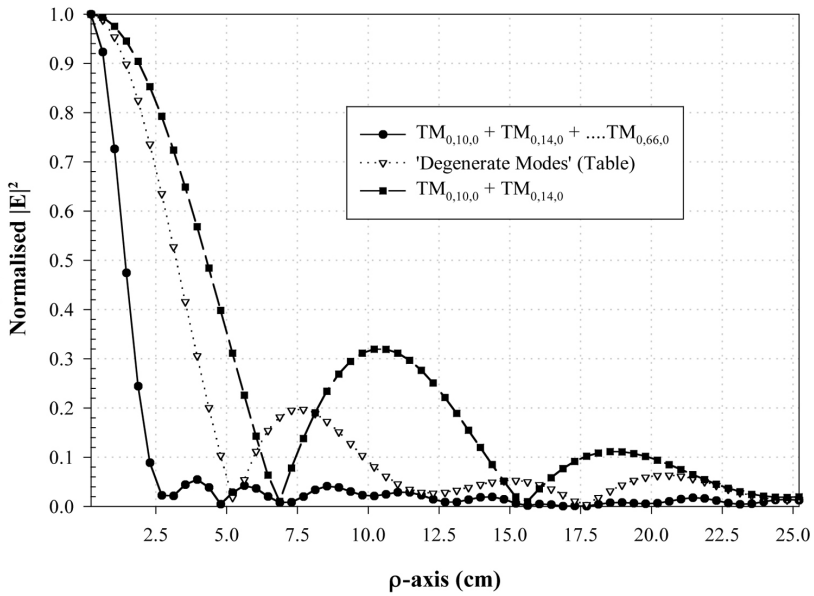

Figure 19: Normalised $|E|^2$ electric field magnitude though ρ-axis from $0 \leq \rho \leq a/4$.

The normalised electric field squared magnitude versus the ρ-axis been plotted. $0 \leq \rho \leq 0.25$ has been plotted as this allows a better comparison of the results around the maxima. The electric field pattern for does not add any useful information to the discussion. The results are symmetrical around the centre of the cavity. $TM_{0,10,0}$ summed with $TM_{0,14,0}$ has an azimuthal L_R equal to -4.95dB. As more modes are added to the calculation, the normalised electric field maxima can be seen to sharpen and the corresponding off centre peaks reduce. Consider an 'ideal' mode superposition (forced degeneracy) where 14 modes from $TM_{0,10,0}$ through to $TM_{0,66,0}$ are summed together. The azimuthal L_R is equal to -12.62dB and L_W equal to 1.46%. A more practical summation of the four almost degenerate TM modes in Table 9 shows that this mode set will produce a slightly wider peak in the electric field pattern in the azimuthal plane compared to the *ideal* 14-mode case. This L_W change is accompanied with a slight degradation in the azimuthal L_R. The L_R for the more limited mode summation is equal to -6.99dB and at a position approximately 7.55cm from the centre of the cavity. The summation also has a L_W equal to 3.25%.

Operating the cavity using very high order modes allows the use of large integer values of q. Increasing q leads to a greater selection of degenerate (or almost degenerate) modes suitable for producing small L_R values. Although the electric field is not focussed in the longitudinal direction (E_z), proper choice is cavity length would ensure uniform heating through the cancerous region. Ideally, the length of cavity should be of similar magnitude to that of the cancerous region (within practical limits). High integer values of q would

result in an average heating effect through the axial length of the cavity with focussing being confined exclusively to the radial axis.

Table 9: Cylindrical cavity results.

'Degenerate' TM Mode Set	$\mathbf{L_R}$ **(dB)**	$\mathbf{L_W}$ **(%)**
$TM_{0,10,0}+TM_{0,14,0}$ (2 modes)	-4.95	4.26
$TM_{0,10,0}+TM_{0,14,0}+\cdots$ $TM_{0,66,0}$ (14 modes)	-12.62	1.46
'Degenerate Mode Set' Table 8	-6.99	3.25

4.5 Conclusion

The chapter provides a preliminary examination of modal superposition in a multimode, degenerate mode, cavity applicator for hyperthermia treatment. The aim of the study was to illustrate that with careful selection of a limited set of high order modes, which have been forced into degeneracy by cavity perturbation, significant field enhancement can be secured in a localised region of the cavity.

Two cases have been evaluated, namely modal superposition in a low height square cross-section cavity and in a low height cylindrical cavity. The low height limitation was adopted to minimise analytical complexity. The models demonstrate that if modal degeneracy can be secured by cavity perturbation, useful levels of field focusing can be produced with only a handful (no more than twelve) of high order modes. For example, with six degenerate modes in a low height cylindrical cavity of 1m diameter, a *hot-spot* of 2.18cm diameter can be placed at the centre of the cavity.

The comprehensive examination of field enhancement in low height cavities clearly show that unless the cavity Q is very high, the degree of degeneracy required to procure useful levels of modal superposition, and hence significant *hot spot* formulation, is well within

the reach of a practical system.

CHAPTER FIVE

QUASI DEGENERATE & NON-DEGENERATE MODE HEATING: OPEN-ENDED MICROWAVE CAVITY APPLICATOR

5.1 Introduction

This chapter considers focussed microwave heating using the evanescent fields of a high order mode in a waveguide cavity. A novel, frequency agile, open-ended microwave oven is described which has been applied to the curing of encapsulants within electronic packaging technologies. A cavity geometry specific to this application area is discussed.

The conditions for resonance within the geometry are presented in Section 5.3. A plane wave analysis technique is used to determine the continuity of the normal electric field through the dielectric interface for a number of high order modes [121]. The evanescent decay within the cavity cut-off region is described with reference to the mode order and bulk filling material relative permittivity. The rate of decay of the evanescent field is also highlighted through consideration of the absorbed power loss within a lossy sample located within the below cut-off waveguide. The position of the lossy sample is varied within the longitudinal plane. The design trade-off between frequency scaling (due to the inclusion of a dielectric filling) and the attenuation of the evanescent fringing fields is presented.

An analysis of the electromagnetic fields within the oven are presented for both single frequency microwave (SFM) and VFM heating. Of particular interest are the boundary conditions at the dielectric-air interface, where focussed heating will occur. A theoretical analysis is conducted in order to validate the process of mode scintillation within the oven. An idealised mode set is presented and the resulting electromagnetic field effect

established.

The potential impact of an open-ended oven incorporating precision alignment is discussed. The device combines a number of design features that make the proposed implementation unique in the area of electronics packaging.

5.2 Open-Ended Cavity Geometry

In electromagnetic terms, the microwave oven can be described as a terminated waveguide transmission line resonator. Because of radiation loss, which normally occurs from the open end of a waveguide, empty metal waveguide cavity resonators are usually formed with short circuits at each end thus taking the form of a closed box (if the waveguide has rectangular cross-section). However, if a significant proportion of the waveguide cavity volume is filled with a low loss, high permittivity dielectric material, a resonant cavity can be formed even if one end is *open*. The resonant modes are trapped waves between the short circuit, at one end, and a quasi open circuit (formed by the dielectric-air interface), at the other.

The TM field components must equal zero at the open end of the cavity (assuming a perfect open circuit) due to boundary conditions. In practice, these fields are small but finite, as a perfect open circuit is not achievable. If the open end represents a *good* open circuit to the cavity fields, the only significant fields to exist at this point are the transverse (to the guide axis) electric fields, which are close to their maximum values. Continuity of tangential electric fields at a dielectric interface requires that similar strength fields will exist at the external surface of the dielectric, in the form of stored energy [for a below cut-off section of waveguide]. A sample of lossy material, placed in these fields, will experience ohmic heating if sufficient power is supplied. The open-ended cavity becomes an *open oven*.

The quality of the open circuit is dependent of the magnitude of the relative permittivity of the dielectric. If it is to be viable, the open-ended oven requires the permittivity of the filling material to be high enough to encourage strong modal resonances by inhibiting radiation from the open end. Moreover, the boundary conditions on the air side of the dielectric-air interface (3.14)-(3.17) require that,

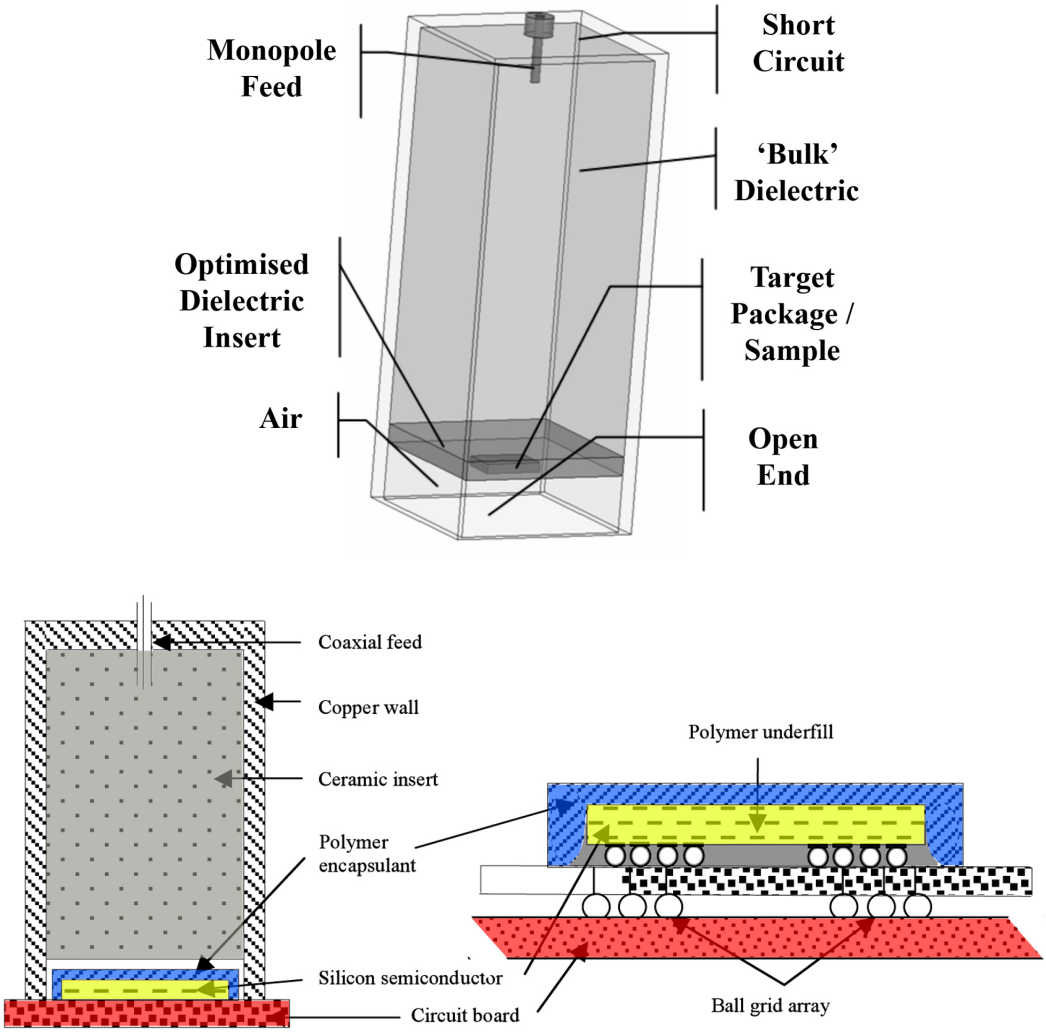

Figure 20: Schematic layouts of the open oven, with an optimised low loss dielectric insert [top], showing position of the target package relative to the dielectric-air boundary [bottom].

$$E_{n_2} = \varepsilon_r E_{n_1} \tag{5.1}$$

$$E_{t_2} = E_{t_1} \tag{5.2}$$

where E_{n_1} and E_{t_1} are the normal and tangential electric fields at the interface in the dielectric region and E_{n_2} and E_{t_2} are the corresponding quantities in the air region. Equations (5.1) and (5.2) suggest that the longitudinal electric field component on the air side of the discontinuity is multiplied by a factor equal to the relative permittivity of the cavity filling. To exploit this field enhancement in the air region, it is proposed that the oven operates on a TM resonant mode.

A schematic of the device incorporating an optimised dielectric insert (described in Chapter 6) is shown in Figure 20. A coupling probe located on the conducting wall opposite the open end of the oven provides a means of exciting a TM resonance within cavity. It is intended that the target package (integrated circuit package, die or chip assembly) be placed within the air filled, cut-off region of the cavity where the evanescent fields are located. This is achieved through physically altering the position of the oven using a precision alignment machine to enable spatial connectivity between target package and cavity oven. It is well known that evanescent fields have been used to generate electromagnetic coupling in a variety of microwave devices [122]. Adjustment of the source power, longitudinal position of the target package within the air filled section, impedance matching from feed transmission line to cavity and target package material characteristics will dictate the optimum length and degree of cure for the package. It is anticipated that the power and cure time requirements of the oven will be found through practical experimental investigation and through complex, multi-physics modeling [123]. The magnitude of the evanescent field directly at the open end of the cavity can be suppressed through consideration of the evanescent field attenuation (Section 5.3.1), the magnitude of the source power and the length of air section such that the electric field strength is zero (or at the very least, within safe limits). An additional dielectric insert (described in Chapter 6) is placed on the boundary between the main or bulk dielectric filling and air region and is shown in Figure 20. Adjustment of the permittivity and length of the dielectric insert allows a means of controlling the boundary condition at the dielectric-air interface and therefore provides a method for optimising the magnitude of the evanescent field.

5.3 Fields at the Dielectric Boundary

The relationship which exists between the fields at the open end of the resonator, and those of the resonant mode within the dielectric filled cavity, can be described through a plane wave description of waveguide or cavity modes [124]. Since the open end of the resonator is cut-off, a conventional impedance matching approach to the interface problem is much less instructive than the field analysis [125]. It should be noted that it is assumed that for any integrated circuit package inserted into the open end of the resonator, curing will occur in very small localities that occupy only a very small portion of the cut-off section. Consequently, the field mechanisms examined in the analysis [121] will not be significantly perturbed by the presence of a target chip or package.

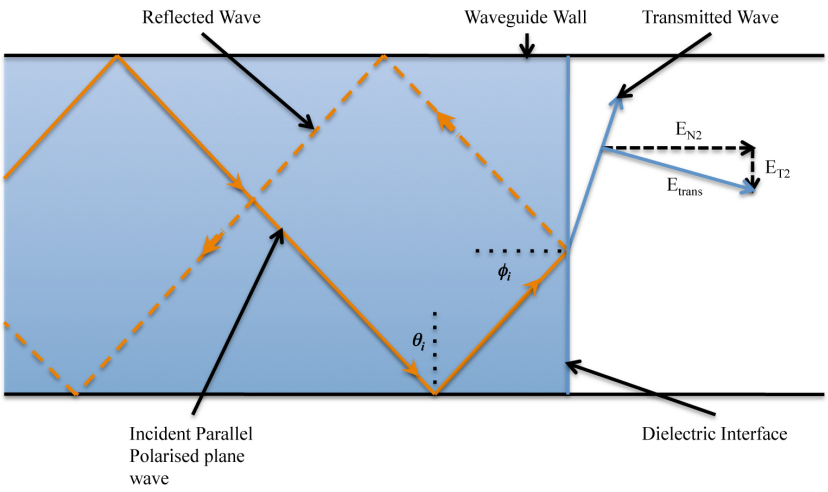

Figure 21: Schematic of parallel polarised plane wave at the dielectric interface showing E-field directions (the transmitted wave becomes evanescent when ϕ_i is greater than the critical angle).

A TM mode in rectangular waveguide can be constructed from parallel polarised plane waves reflecting off the conducting walls, and, in the case of a cavity, also off the end faces. A two dimensional schematic of the process is presented in Figure 21.

Plane wave refraction at a plane dielectric-air interface results in the following formula for the reflection coefficient for a parallel polarised plane incident on the interface at angle ϕ_i,

$$\Gamma = \frac{\cos\phi_i - \sqrt{\varepsilon_r(1 - \varepsilon_r \sin^2\phi_i)}}{\cos\phi_i + \sqrt{\varepsilon_r(1 - \varepsilon_r \sin^2\phi_i)}} \tag{5.3}$$

where ε_r is the relative permittivity of the cavity filling material. When $|E_z/E_x|$ or $|E_z/E_y| > 2$ (when the TM mode is operating not too far from cut-off) the square root term in (5.3) becomes imaginary. Consequently, $|\Gamma| = 1$ and total internal reflection occurs at the interface. The cavity will resonate strongly for such modes. The behaviour of the reflection coefficient Γ at the interface as a function of frequency, normalised to the frequency of the TM_{33} waveguide mode, is shown in Figure 22. The calculations were performed for the dielectric filled square cross-section guide with dimension 25mm x 25mm filled with a lossless material with $\varepsilon_r = 6$. For the plane wave model to correctly represent a particular TM mode, its angle of incidence θ on the conducting waveguide walls must be related to the propagation coefficient of the mode β through,

$$\sin\theta_i = \frac{\beta}{\varepsilon_r k_0} \tag{5.4}$$

while it is noted that $\phi_i = 90° - \theta_i$.

The dependence of $\Re\{\Gamma\}$ and $\Im\{\Gamma\}$ in the normalised frequency $(f_0/f_{c_{33}})$, as shown in Figure 22, can best be explained by referring to (5.3) and (5.4). At $f_0/f_{c_{33}} = 1$, the TM_{33} mode in the waveguide is cut-off, and $\beta = 0$. Hence $\theta_i = 0$ and $\phi_i = 90°$. The plane-wave components of the TM_{33} mode propagate parallel to the open interface therefore,

$$\Re\{\Gamma\} = -1 \tag{5.5}$$

As $f_0/f_{c_{33}}$ becomes larger than unity, the numerator and the denominator in equation (5.3) become complex conjugates. Therefore, $|\Gamma| = 1$ with the real component increasing steadily from -1 to $+1$ at $f_0/f_{c_{33}} = 2.45$. The imaginary component decreases to a minimum of -1, where $\Re\{\Gamma\} = 0$, and rises rapidly to zero at $f_0/f_{c_{33}} = 2.45$. At this value of the normalised frequency,

$$\sin\phi_i = \frac{1}{\sqrt{\varepsilon_r}} = \frac{1}{\sqrt{6}} \tag{5.6}$$

and the plane wave components of the TM_{33} waveguide mode are incident on the open interface at the critical angle. When $f_0/f_{c_{33}}$ is increased in magnitude beyond 2.45, transmission into the external air region begins to occur and the reflection coefficient is real. As $f_0/f_{c_{33}}$ continues to increase beyond a value of approximately 4, ϕ_i tends towards zero and,

$$\Gamma \Rightarrow \frac{1-\sqrt{\varepsilon}}{1+\sqrt{\varepsilon_r}} = -0.42 \tag{5.7}$$

This behaviour of the constituent plane-waves is true of all modes at the open interface of a dielectric filled square cross-section cavity resonator.

In the normalised frequency range,

$$1 < f_0/f_{c_{33}} < 2.45 \tag{5.8}$$

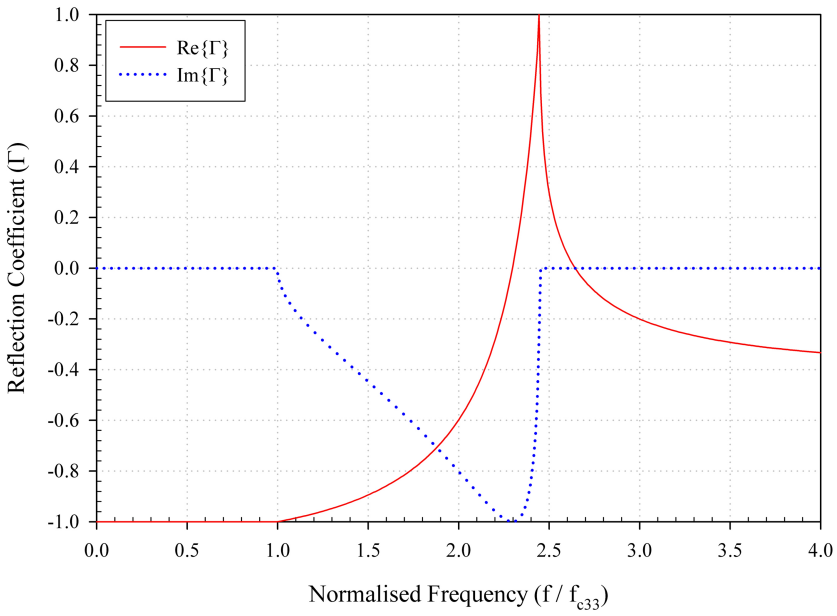

Figure 22: Reflection coefficient at the dielectric interface as a function of normalised frequency $f_0/f_{c_{33}}$ $(m = n = 3, \varepsilon_r = 6)$.

total internal reflection does not mean that there are no fields on the air-side of the open-end interface. The fields are governed by the boundary conditions expressed in (5.1) and (5.2). Moreover, plane wave calculations show that E_T, the total electric field on the dielectric side of the interface, is given by,

$$E_T = (1 + \Gamma)E_{inc} \tag{5.9}$$

where E_{inc} is the electric field magnitude of the incident plane wave in the waveguide. Hence using (5.1), (5.2), (5.3) and (5.4) and on the air side of the interface,

$$E_{n_2} = \varepsilon_r[\sin\phi_i + \rho\sin(-\phi_i)] \tag{5.10}$$

$$E_{inc} = \varepsilon_r(1 - \Gamma)\sin\phi_i E_{inc} \tag{5.11}$$

$$E_{t_2} = [\cos\phi_i + \rho\cos(-\phi_i)] \tag{5.12}$$

$$E_{inc} = (1 + \Gamma)\cos\phi_i E_{inc} \tag{5.13}$$

Figure 23 depicts the relationship between E_{n_2} and E_{t_2} and the frequency of excitation within the cavity when (5.11) and (5.13) are used in conjunction with (5.3) and (5.4). The electric field magnitude E_i for the incident TM mode is equal to twice the incident plane

wave magnitude in a perfect waveguide.

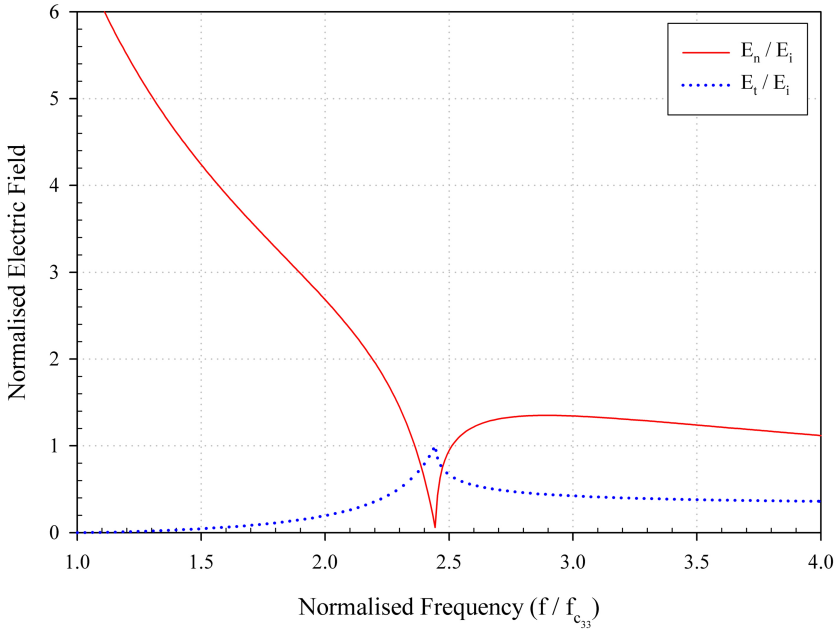

Figure 23: Estimated E-fields on the air side of the dielectric interface normalised to the cavity E-field magnitude expressed as a function of normalised frequency $(m = n = 3, \varepsilon_r = 6)$.

Figure 23 shows clearly that in the range of frequencies, indicated within (5.8), the normal component of electric field on the air side of the interface is much larger than both the internal cavity field and the external tangential electric field, except where f_0/f_{c33} approaches the critical value. Table 10 shows that the TM_{33k} modes $(k = 1/2, 3/2, 5/2)$ are within this range. Consequently, these modes should resonate strongly, while at the same time generating a strong external field for device heating in the open end.

Table 10: Computed TM_{33k} *mode resonances.*

k	**Resonant Frequency (GHz)**	f_0/f_{c33}
0	10.036	1.0000
1/2	10.042	1.0016
3/2	10.079	1.0163
5/2	10.153	1.0448

5.3.1 Evanescent Region

A cut-off section of waveguide is created within the volume of the cavity through recessing the bulk dielectric from the open end. The resonant frequency of the coupled mode or mode set, within the bulk dielectric, should be lower than the cut-off frequency of the air filled recess / heating region in order to ensure a strong resonance and good penetration of the normal electric field, as suggested by Figure 23. As such, the fields within the air section of waveguide are evanescent and attenuate with distance from the dielectric-air interface. The rate of attenuation is related to the resonant frequency of the coupled mode and the cut-off frequency of the air filled section. The greater the difference between the coupled mode resonant frequency and the cut-off frequency; the greater the rate of attenuation of the evanescent field. The rate of attenuation of an evanescent field within cut-off waveguide [109] is,

$$\alpha = \beta_o \sqrt{\left(\frac{\lambda_o}{\lambda_c}\right)^2 - 1} \tag{5.14}$$

where β_o is the propagation constant in an unbounded medium (for the resonating cavity described within this chapter, this corresponds to the air region), λ_o is the wavelength in an unbounded medium and λ_c is the cut-off wavelength of the waveguide (determined by the cross section size of the evanescent region). The resonant frequency of the mode within the bulk dielectric is used to determine β_o. Alteration of the relative permittivity of the bulk dielectric will perturb the resonant frequency of a coupled mode thus altering the attenuation within the evanescent region.

In practical terms, control of the evanescent field attenuation introduces a number of design considerations. It is a requirement within the overall design that the fields be confined to the volume of the cavity. In the event of a very high power source being used to increase the heating potential of the system, the likelihood of fringing fields existing outside of the oven [at the open end] is increased. Adjustment of the attenuation of the evanescent field and length of recess region can offer a means of reducing the field at the open end to zero (or at the very least, to within prescribed safe limits). Additionally, care should be taken to ensure that introduction of the target package does not decrease the cut-off frequency of the heating region to a level where either propagation occurs resulting in the fringing fields at the open end increasing to beyond prescribed levels.

An additional design consideration is the longitudinal position of the lossy material [within

the heating region] relative to the position of the dielectric-air interface. If the rate of attenuation of the evanescent field and the distance between dielectric-air interface and target load is large then the fields at the target location may be reduced below the levels required for efficient heating. The height of the target package, shown in Figure 20, may dictate that solder bumps (for example) are located several millimetres from the dielectric-air interface. Care must be taken to ensure that the trade-off between attenuation, recess length, target location and coupled power do not combine to produce minimal fringing fields at the open end at the expense of the actual heating potential of the device.

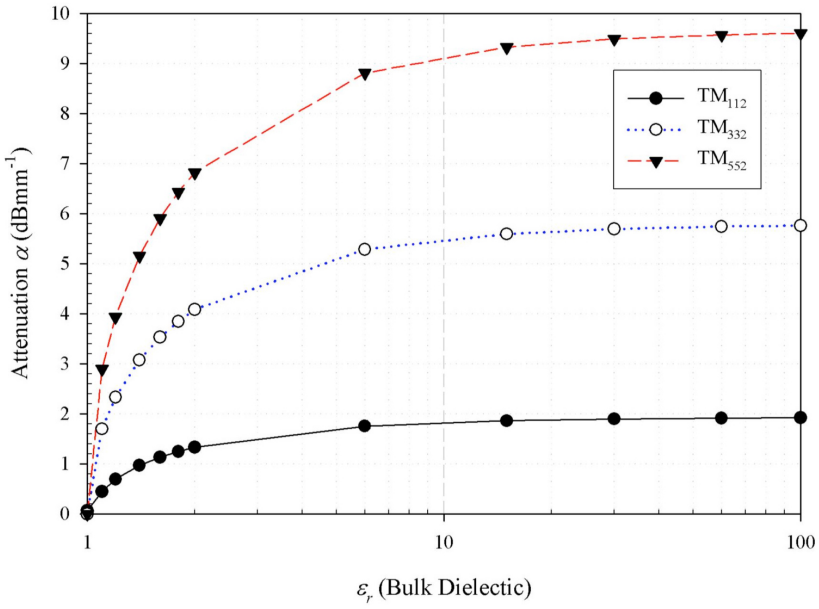

Figure 24: Attenuation of the evanescent field within the air region.

Alteration of the bulk dielectric relative permittivity offers a flexible method of controlling the attenuation of the evanescent field. Increasing the relative permittivity of the filling material reduces the resonant frequency of a mode, relative to the cut-off frequency within the air filled region, and therefore increases the rate of attenuation of the evanescent field decay. The rate of attenuation within the evanescent section of waveguide versus bulk dielectric within the resonating section is given in Figure 24. The volume of the cavity is held constant. As a result, any change in dielectric constant of the material within the resonating region will cause a change in resonant frequency of the coupled mode. Increasing the relative permittivity of the bulk dielectric will reduce of the resonating frequency of the mode set under investigation. The bulk dielectric relative permittivity is varied from 1 to 100 and the rate of attenuation within the non-propagating region calculated using for three resonant modes: TM_{112}, TM_{332} and TM_{552}. The rate of attenuation is dependant on two factors, namely, the order of mode resonant within the bulk dielectric

and the relative permittivity of the bulk dielectric itself.

5.3.2 Dielectric Power Loss within Sample

The power absorbed per unit volume (Wm^{-3}) due to dielectric loss within a material exposed to an electric field is defined as,

$$P_D = \frac{f_{res}\pi\varepsilon'' \int_V \vec{E} \cdot \vec{E} dV}{V} \tag{5.15}$$

where f_{res} is the resonant frequency of the coupled mode, ε'' is the imaginary component of the complex permittivity, $\vec{E}$ is the electric field and V is the volume of the material. In order to maximise the dielectric power loss, and therefore the heating potential, the target sample should have a high dielectric loss tangent relative to the dielectric filling [bulk] materials within the cavity. If the dielectric loss of the bulk filling material is *high*, then unwanted heating within the material will occur. Additionally, if the bulk filling dielectric properties are not stable with temperature, then any increase in temperature may cause unwanted perturbation of the modal resonant frequency. Regulation of the source power ultimately reduces the capacity of the system to cure quickly, due to a reduction of the magnitude of the evanescent field [49], [50].

A more efficient heating system would be one that has minimal dielectric loss within the bulk filling material (located in the propagating region of the cavity) and high dielectric losses within the target sample. This can be achieved by weighting the fields and loss properties of the materials in favour of the target sample. The loss tangent of the target material will generally be several orders of magnitude larger than that of the dielectrics within the cavity volume. Since the volume of the target sample is small compared to the overall volume of the cavity, the perturbation of the resonant frequency, due to a change in complex permittivity of the sample, will be minimal. Typical values for the dielectric constant of an epoxy / encapsulants and dielectric range from 4 to 13 and anything from 2 to 30, respectively. Typical values of $\tan\delta$ [at X-band and $24°$C] for the epoxy and bulk dielectric range from $2\mathrm{x}10^{-4}$ to $5\mathrm{x}10^{-1}$ and $1\mathrm{x}10^{-4}$ to $1\mathrm{x}10^{-3}$, respectively.

An electromagnetic simulation package (HFSS) is used to analyse the change in normalised power density within the lossy target sample relative to the power density within the low loss bulk dielectric material. An *eigenmode solution* with approximately 24,000

tetrahedra enables the field pattern and resonant frequency of the modes under consideration to be found for each solution. Maximisation of the normalised power density suggests an increase in the overall heating performance of the cavity system as outline above. Three cavities, with the same volume but different bulk dielectric relative permittivites, are simulated based on coupling of the TM_{331} mode. A small lossy target sample is placed within the electric field maxima of the evanescent field. The normalised power density is then calculated as the position of the sample is extended from the dielectric-air interface. The normalised power density is found from,

$$\begin{aligned} P_{D_{ep}} &= \frac{\frac{f_{res}\pi\varepsilon''_{r_{ep}}\varepsilon_o \int_{V_{ep}} \vec{E_{ep}}\cdot\vec{E_{ep}}\ dV_{ep}}{V_{ep}}}{\frac{f_{res}\pi\varepsilon''_{r_{bulk}}\varepsilon_o \int_{V_{bulk}} \vec{E_{bulk}}\cdot\vec{E_{bulk}}\ dV_{bulk}}{V_{bulk}}} \\ &= \left(\frac{V_{bulk}}{V_{ep}}\right)\left(\frac{\varepsilon''_{r_{ep}}}{\varepsilon''_{r_{bulk}}}\right)\left(\frac{\int_{V_{ep}} \vec{E_{ep}}\cdot\vec{E_{ep}}\ dV_{ep}}{\int_{V_{bulk}} \vec{E_{bulk}}\cdot\vec{E_{bulk}}\ dV_{bulk}}\right) \\ &= \left(\frac{V_{bulk}}{V_{ep}}\right)\left(\frac{\varepsilon'_{r_{ep}}}{\varepsilon'_{r_{bulk}}}\right)\left(\frac{\tan\delta_{ep}}{\tan\delta_{bulk}}\right)\left(\frac{\int_{V_{ep}} \vec{E_{ep}}\cdot\vec{E_{ep}}\ dV_{ep}}{\int_{V_{bulk}} \vec{E_{bulk}}\cdot\vec{E_{bulk}}\ dV_{bulk}}\right) \end{aligned} \tag{5.16}$$

where the ep and $bulk$ subscripts correspond to the epoxy sample and bulk dielectric respectively, V is the volume, ε is the permittivity of the material, $\tan\delta$ is the dielectric loss tangent and $\vec{E}$ is the electric field. The normalised power density within the epoxy sample can be investigated through alteration of three parameters within the design: the volume of the dielectric / epoxy sample, the complex permittivity (dielectric constant and $\tan\delta$) and the magnitude of the average electric field within each component.

It is clear from (5.16) that an increase in the dielectric constant, loss tangent or average field within the epoxy relative to the bulk dielectric parameters will cause an increase in normalised power density. Both the dielectric constant and loss tangent are parameters that can be managed at the design stage. In order to maximise the normalised power density, an epoxy (or lossy material) should be chosen that has a large loss tangent while the dielectric fillings should be as lossless as possible. Equation (5.16) [in combination with the typical material values given previously] indicate that the loss tangent *ratio* will be several times larger than the dielectric constant *ratio* and, as such, will have a dominating influence of the magnitude of the normalised power density.

The absorbed power due to the evanescent fields on the air side of the dielectric interface has been modelled by spatially aligning several lossy *pellets* with peaks of the $TM_{33,5/2}$ mode. The normalised power density is then plotted versus distance from the

Table 11: Cavity and pellet Dimensions.

ε_r	**Cavity (mm)**	**Air Gap (mm)**	**Pellet (mm)**
2	40 x 40 x 115	10	9 x 9 x 0.5
6	23 x 23 x 110	10	3.45 x 3.45 x 0.5
30	11 x 11 x 110	10	0.825 x 0.825 x 0.25

bulk dielectric-air interface. For each bulk dielectric variation, the cavity and pellet size are scaled such that excitation of the $TM_{33,5/2}$ occurs at approximately 10GHz. Table 11 contains dimensional information for both the cavity and pellet size. In all cases the pellet has a dielectric constant of 4.2 and a loss tangent of 0.02.

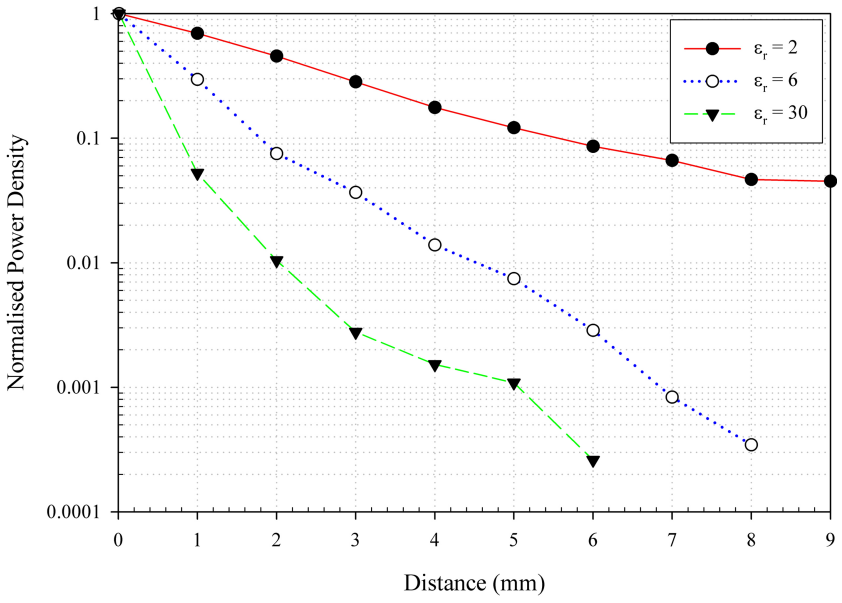

Figure 25: Normalised power density within a lossy material versus distance from bulk dielectric-air interface.

As anticipated by (5.14), the power absorbed decays exponentially with distance due to the exponential decay of the field. For high values of bulk dielectric permittivity, the rate of attenuation is very much greater than the lower values (where excitation of the cavity occurs closer to the cut-off frequency of the air filled region of waveguide).

The analysis conducted in [120] indicates that a pellet power absorption of 16μW is produced for a 1W input power suggesting the current prototype is relatively inefficient. It was hypothesised that an oven power of 300W, for approximately 1min, would be sufficient for curing of typical integrated circuit packages in the open-ended microwave oven.

An increase in either pellet dielectric loss or electric field strength is required in order to increase the absorbed power density within the pellet.

5.4 TM Mode - Excitation Options

5.4.1 Single Frequency Mode

It is envisaged that the open oven be excited using a conventional single mode excitation or using a VFM excitation. Using a single order mode excitation, it is anticipated that both the fundamental mode (SFM_f) or very high order mode variation on the fundamental mode (SFM_h) will offer the user practical choices in the *type* of cure. The three excitation methods are desired.

Microwave power fundamentally accelerates the cure kinetics of polymer adhesives [37]. It provides a route to maximise the deposition of heat energy into the polymer materials due to the dielectric loss characteristics. Therefore, microwaves can be used to minimise the temperature increase in the surrounding materials such as the substrate and die during the cure process. This is especially important for devices incorporating either low thermal budget materials or interfaces with large thermal coefficient mismatch. The concentration of heat into the polymer during the cure process promotes its adhesion properties, as the magnitude of residual stress between the polymer and materials, to which it is being bonded, will be low. For example, it is well known in flip-chip packages, delamination between encapsulant / underfill and the die is a major contributor to low reliability (hence lifetime) of such packages.

Through SFM_h, it is hypothesised that greater selective heating will be offered through alignment of the TM normal electric field peaks with the solder / ECA bumps of a die or chip package. Through minimising the heating within the die itself, the thermal stress during the cure process can be reduced increasing the lifetime of the product. However, as will be demonstrated in Chapter 7, quasi degeneracy limits the simple implementation of a SFM_h excitation. SFM_h does not allow for uniform heating within the target package due to the spatial electric field variation. While this may prove useful for targeted heating of, for example, solder bumps, it reduces the uniformity of cure within encapsulant processes.

A design and performance assessment of the open oven concept was carried out by modelling a prototype design using a finite element method (FEM) electromagnetic simulation package (Ansoft HFSS). The dimensions of the cavity are 24mm x 24mm x 110mm. The bulk dielectric material was modelled with a relative permittivity of 6 and a $\tan\delta$ of 0.006. Also, the filling was made 5mm shorter than the length of the waveguide to procure a short section of cut-off waveguide at the open end. Using the *driven mode* simulation procedure, the model was excited at the short circuit end with a z-directed probe to ensure the coupling of a TM mode.

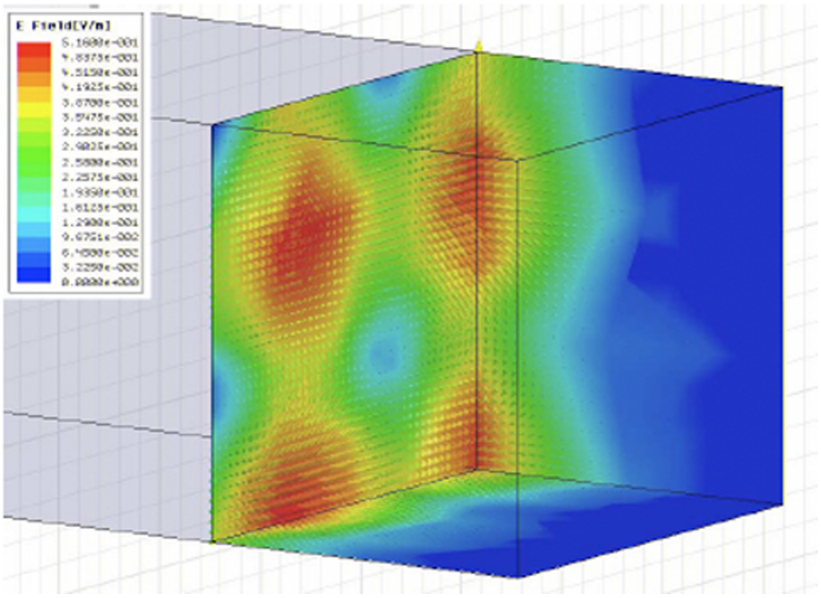

Figure 26: Evanescent fringing field within cut-off region.

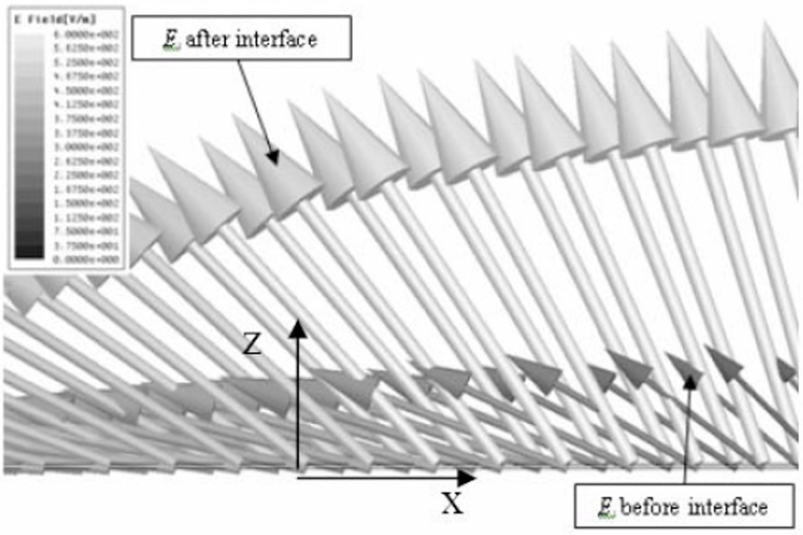

Figure 27: FEM model of the total electric field distribution at the dielectric interface (dark arrows = just inside interface; light arrows = just on the air side of the interface).

Figure 26 displays $|E|$ within the air filled, cut-off section of a waveguide filled with a bulk filling material with $\varepsilon_r = 6$. One quarter section has been simulated incorporating two perfect magnetic wall symmetry planes in order to reduce the computational effort. The $TM_{33,5/2}$ mode exhibits a strongly selective evanescent field within the cut-off section at 10.08GHz. The '$5/2$' field variation within the longitudinal plane is due to the quasi open-circuit boundary condition at the dielectirc-air interface. The field tends to approximately 0V/m after 3mm. Figure 27 displays a detailed analysis of the electric fields in the planes immediately before and after the dielectric-air interface. It is clear from Figure 27 that the FEM model predicts an electric field at the air-dielectric interface which is considerably stronger on the air side of the interface as compared to the interface inside the dielectric. The levels are in good agreement with the predictions made from the electric flux density continuity relationship (5.1). Figure 28 and Figure 29 display the electric field before and after the interface for a cavity partially filled with a dielectric constant and excited by the TM_{33l} mode set. One quarter of the cavity has been simulated in order to reduce the complexity of the design and the resultant computational effort. Two symmetry planes exist located on the back walls.

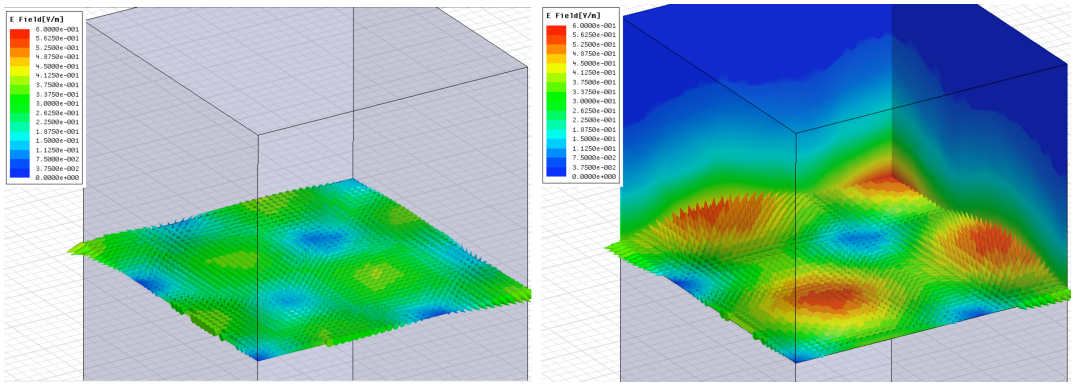

Figure 28: Electric field prior / after the dielectric interface.

It can be seen from Figure 28 that the transverse field is continuous though the interface. The multiplication *effect* of the normal field through the interface is shown in Figure 29. The normal electric field maximum after the interface is approximately 6 times greater than the maximum normal field before the interface. It was observed that the maximum electric field after the interface was approximately 6dB to 8dB less than the maximum electric field within the dielectric material for the TM_{33l} mode set. This holds for a variety of dielectric constants. In effect, a very high permittivity dielectric is desirable in order to excite a very high order mode at a low frequency and also to maximise the multiplication of the normal field at the dielectric-air interface.

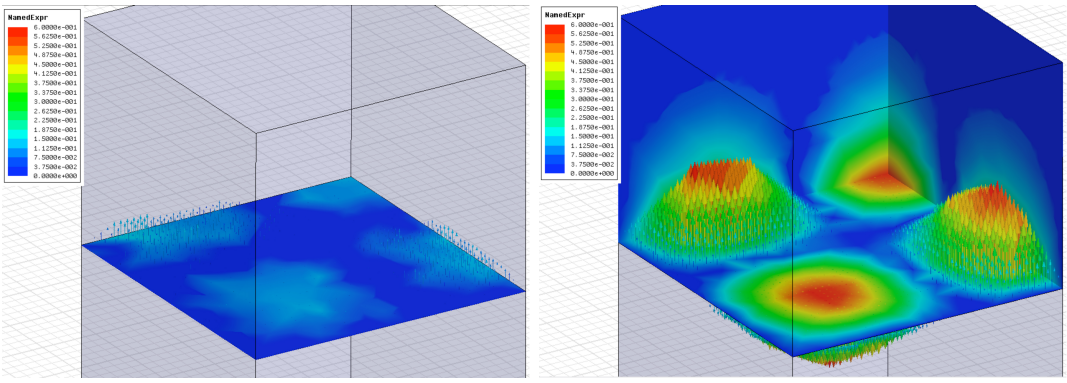

Figure 29: Normal electric field prior / after the dielectric interface.

5.4.2 Variable Frequency Microwave Theoretical Analysis

Targeted mode hopping or jumping is a well-known technique often used within radar *jamming* applications. In this context, the term *frequency hopping* will be applied to the process of alternating between a set of prescribed resonant modes within the waveguide cavity. An assumption is made in order to simplify the analysis: each resonant mode that is excited within the cavity volume is distinct and non-degenerate. Other modes that may be loosely coupled into the cavity are discounted. If the degree of coupling of the quasi degenerate modes is known, it is possible to calculate the field distribution of multiple targeted degenerate modes sets as suggested by the degenerate mode model outlined in Section 4.4.

The mean square of a function $x(t)$ is,

$$\left\langle x^2(t) \right\rangle = \frac{1}{T_0} \int_{t_0}^{t_0+T_0} x^2(t) dt \tag{5.17}$$

leading to the root mean square of x given by,

$$x_{rms} = \sqrt{\left\langle x^2(t) \right\rangle} \tag{5.18}$$

As a simply example, consider a function $f(x_a, x_b)$ where,

$$f(x_a, x_b) = \begin{cases} x_a(t) & 0 \leq t \leq 2\pi \\ x_b(t) & 2\pi < t \leq 4\pi \end{cases} \tag{5.19}$$

and

$$x_a(t) = A\sin(t) \tag{5.20}$$

$$x_b(t) = B\sin(3t) \tag{5.21}$$

The mean square of x_a is found from,

$$\begin{aligned}\left\langle x_a^2(t)\right\rangle &= \frac{A^2}{2\pi}\int_0^{2\pi}\frac{1}{2}\left[1-\cos(2t)\right]dt \\ &= \frac{A^2}{2}\end{aligned} \tag{5.22}$$

Therefore, the root mean square of x_a is,

$$x_{a_{rms}} = \frac{A}{\sqrt{2}} \tag{5.23}$$

Therefore, the following integral holds for f_{rms},

$$\begin{aligned}f_{rms} = \sqrt{\langle f^2\rangle} &= \sqrt{\frac{1}{4\pi}\left[\int_0^{2\pi}x_a^2dt+\int_{2\pi}^{4\pi}x_b^2dt\right]} \\ &= \frac{1}{2}\sqrt{A^2+B^2}\end{aligned} \tag{5.24}$$

If the analysis is extended to include a spatial term, say $\sin(z)$, within each function then (5.20) and (5.21) become,

$$x_a(z,t) = A\sin(z_a)\sin(t) \tag{5.25}$$

$$x_b(z,t) = B\sin(z_b)\sin(3t) \tag{5.26}$$

and,

$$f(x_a,x_b) = \begin{cases} x_a(z,t) & 0\le t\le 2\pi \\ x_b(z,t) & 2\pi < t\le 4\pi \end{cases} \tag{5.27}$$

Then the mean square of the f incorporating a term dependent on z is,

$$\langle f^2(z,t)\rangle = \frac{1}{4}\left(A^2\sin^2(z_a) + B^2\sin^2(z_b)\right) \tag{5.28}$$

Finally, the root mean square of (5.28) is found from,

$$f_{rms} = \sqrt{\langle f^2(z,t)\rangle} = \frac{1}{2}\sqrt{A^2\sin^2(z_a) + B^2\sin^2(z_b)} \tag{5.29}$$

Equation (5.29) shows that f_{rms} is dependent on the amplitude of the individual spatial terms. In general, for the case of an infinite number of unique spatial distributions, the following relation holds,

$$\sqrt{\langle f^2(z,t)\rangle} = \sqrt{\sum_{i=1}^{\infty} C_i^2\sin^2(z_i)} \tag{5.30}$$

where C_i is the amplitude of the function and z_i describes a spatial distribution in the z direction. This analysis suggests that in order to find the average spatial distribution over the total period, a weighted summation of the spatial components within the distribution can be made. However, the analysis conducted so far has assumed that each spatial component in the z direction is 'excited' over the same period. In practise this may not be practical. Instead, it would be far more likely that there be a requirement for uneven resident times for each mode.

A general example applied to a waveguide cavity is presented. A mode-hopping scheme excites three fictitious, non-degenerate modes in turn with each mode resident for 1ms. *Mode A* is resonant at 10GHz, *Mode B* is resonant at 11GHz and *Mode C* is resonant at 12GHz. The total time taken for a single frequency sweep cycle is 3ms.

The TM mode electric field distribution within the cavity for each mode is be described by,

$$E(x,y,z,\omega,t) = \begin{cases} e_a(x,y,z)\sin(\omega_a t) & 0 \le t \le p \\ e_b(x,y,z)\sin(\omega_b t) & p < t \le s \\ e_c(x,y,z)\sin(\omega_c t) & s < t \le q \end{cases} \tag{5.31}$$

where $e_i(x, y, z)$ describes the spatial field distribution of the coupled mode and p, s and q describe the resident time of each mode, respectively.

The mean square of mode E_a is,

$$\begin{aligned} \left\langle E_a^2 \right\rangle &= \frac{e_a^2(x,y,z)}{T_0} \int_0^p A^2 \sin^2(\omega_a t) dt \\ &= A'' e_a^2(x,y,z) \end{aligned} \tag{5.32}$$

The mean square of mode E_b is,

$$\begin{aligned} \left\langle E_b^2 \right\rangle &= \frac{e_b^2(x,y,z)}{T_0} \int_p^s B^2 \sin^2(\omega_b t) dt \\ &= B'' e_b^2(x,y,z) \end{aligned} \tag{5.33}$$

The mean square of mode E_c is,

$$\begin{aligned} \left\langle E_c^2 \right\rangle &= \frac{e_c^2(x,y,z)}{T_0} \int_s^q C^2 \sin^2(\omega_c t) dt \\ &= C'' e_c^2(x,y,z) \end{aligned} \tag{5.34}$$

where,

$$A'' = \left[\frac{1}{4\pi q} A^2 \left(p - \frac{\sin(2\omega_a p)}{2\omega_a} \right) \right] \tag{5.35}$$

$$B'' = \frac{B^2}{4\pi q} \left[(s-p) - \frac{1}{2\omega_b} \left[\sin(2\omega_b s) - \sin(2\omega_b p) \right] \right] \tag{5.36}$$

$$C'' = \frac{C^2}{4\pi q} \left[(q-s) - \frac{1}{2\omega_c} \left[\sin(2\omega_c q) - \sin(2\omega_c s) \right] \right] \tag{5.37}$$

The root mean square of (5.31) is found from,

$$\sqrt{\langle E^2 \rangle} = \sqrt{A'' e_a^2(x,y,z) + B'' e_b^2(x,y,z) + C'' e_c^2(x,y,z)} \tag{5.38}$$

Table 12: Fictitious mode set data with equal resident time.

Mode	**Resident Time (ms)**	**Frequency (GHz)**	$\boldsymbol{\omega}$ (10^9) **rads**$^{-1}$
A	1	10	62.83
B	1	11	69.12
C	1	12	75.4

Using the values within Table 12 in (5.32)-(5.34) then,

$$A'' \cong \frac{A^2}{12\pi} \tag{5.39}$$

$$B'' \cong \frac{B^2}{12\pi} \tag{5.40}$$

$$C'' \cong \frac{C^2}{12\pi} \tag{5.41}$$

Therefore, the average electric field within the cavity is approximated by,

$$\sqrt{\langle E^2 \rangle} \cong \sqrt{\frac{A^2}{12\pi} e_a^2(x,y,z) + \frac{B^2}{12\pi} e_b^2(x,y,z) + \frac{C^2}{12\pi} e_c^2(x,y,z)} \tag{5.42}$$

Table 13 describes unequal resident times for each mode. Using these values gives,

$$A'' \cong \frac{A^2}{60\pi} \tag{5.43}$$

$$B'' \cong \frac{B^2}{15\pi} \tag{5.44}$$

$$C'' \cong \frac{C^2}{6\pi} \tag{5.45}$$

and,

$$\sqrt{\langle E^2 \rangle} \cong \sqrt{\frac{A^2}{60\pi} e_a^2(x,y,z) + \frac{B^2}{15\pi} e_b^2(x,y,z) + \frac{C^2}{6\pi} e_c^2(x,y,z)} \tag{5.46}$$

In other words, the non-uniform resident times for each mode leads to a greater or lesser weighting of each modal pattern within the average distribution. A comparison can be

Table 13: Fictitious mode set data with unequal resident time.

Mode	Resident Time (ms)	Frequency (GHz)	ω (10^9) rads^{-1}
A	1	10	62.83
B	4	11	69.12
C	10	12	75.4

made between the field summation of quasi degenerate modes and the targeted frequency jumping to specific mode sets. Equations (4.10) and (5.38) describe similar field summation phenomenon. In the first case, the instantaneous field distribution is described through summation of [degenerate] modes where the period of each mode is equal. The weighting of each mode within the summation is determined primarily through the degree of coupling (which is in turn determined by coupling mechanism location and geometry). The second case describes an expression for describing the average field summation through the course of a single frequency sweep. In this case, the instantaneous field is in a continual state of scintillation. The average field distribution is then described through a weighted summation of the modal field pattern where the amount of weighting is determined through the degree of coupling and resident time.

Within low Q cavities, it can be difficult to excite a single high order mode due to the effect of quasi degeneracy as outlined in Section 4.4.2. Rather than frequency *hop* from one distinct mode to another, it would be more accurate to describe a process of jumping between quasi degenerate mode sets. Each mode set consists of a weighted summation of degenerate modes as described by (4.10). The total number of quasi degenerate mode sets would be determined through the efficiency of the coupling into the cavity, the value of loaded Q within the cavity and the range of frequencies that the source is swept over. It is intuitive to assume that, for VFM, it is beneficial to incorporate very wide band coupling into the cavity such that a wide variation of modes are excited within the cavity volume.

5.4.3 VFM Mode Set

The VFM analysis presented in the previous section is applied to a practical mode set within an open-ended, dielectric filled waveguide cavity. An open-ended rectangular waveguide cavity with dimensions equal to 24mm x 24mm x 105mm is described. The cavity is filled with a low loss dielectric material with relative permittivity $\varepsilon_r = 6$ and is

recessed from the open end of the cavity by 5mm. High order modes exist within the X-band frequency region (8GHz - 12GHz) ranging from the $TM_{226^{th}}$ resonant at 8.0072GHz to the $TM_{426^{th}}$ mode at 11.9242GHz. A TM resonance can be created within the dielectric filling by placing a coupling probe on the conducting wall opposite the open end. For the purpose of this analysis, the coupling probe is assumed to perfectly couple individual modes with equal weighting. In addition, modes with longitudinal field variations of greater than 6 are discounted.

A difference between a conventional VFM oven and the open-ended oven approach exists within the dimensional order of the field scintillation. A conventional VFM oven obtains an average uniform field through scintillation of mode orders within three dimensions. However, the open-ended oven proposed within this chapter obtains an average field distribution within the transverse cross-section only [within two dimensions] since the longitudinal field component within the air filled section is evanescent.

Appendix A contains a range of TM modes resonant frequencies and the corresponding normal field magnitude on the dielectric-air interface and within the air filled section of waveguide for an idealised excitation. Figure 30 and Figure 31 display the normalised root mean square of the electric field distribution from a frequency sweep through X-Band where it is assumed that every mode is excited equally and with equal residency. As such, each mode has a maximum field magnitude at the conducting wall opposite the open face. Equation (5.38) suggest that the root mean square magnitude is a summation of the individual field distributions within the transverse plane of the waveguide and is evaluated using MATLAB computer software with modal data provided in Appendix A.

The distribution is normalised to the maximum magnitude within the transverse plane. Figure 30 and Figure 31 indicate that a uniformity of field distribution is created through the central area of the transverse plane. The field decays rapidly to zero at the edges of the plane due to the well known transverse electric field boundary condition at the surface of a perfectly conducting wall. Figure 31 indicates small peaks of field at approximately $a/5$ (where a is the x or y distance). The field at the centre of the cavity is 1.5dB less than this peak. It is anticipated that using very high order modes, with spatial variations of the order of 10, will reduce the distance from the wall to the position of the first field peak while maintaining a degree of uniformity through the centre of the cavity.

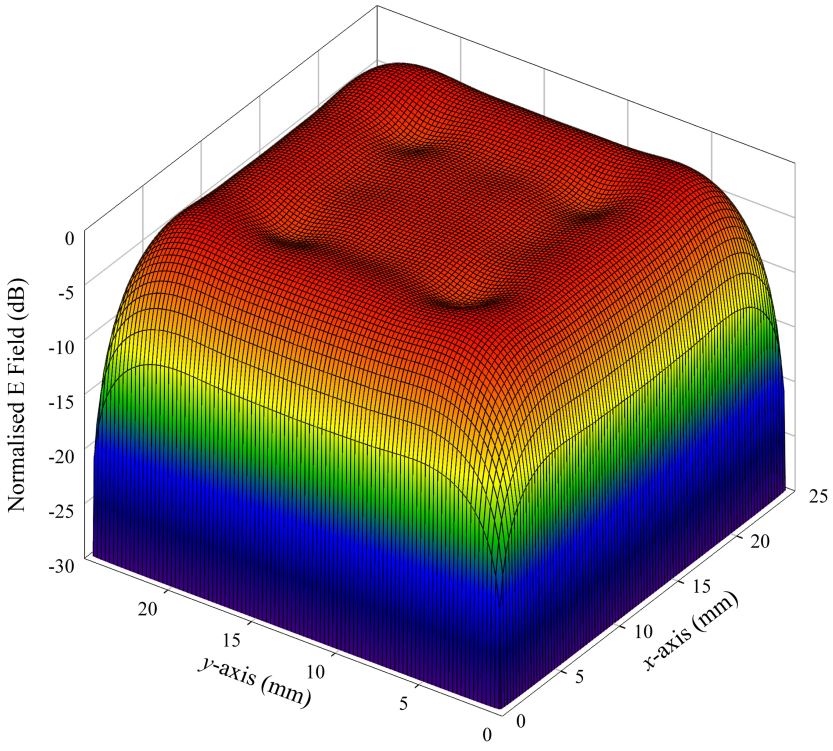

Figure 30: Normalised average electric field within the evanescent region.

5.5 Conclusion

A novel open-ended microwave oven is presented that makes use of both SFM and VFM excitation methods. The open-ended design feature is described with specific reference to the boundary conditions at the dielectric-air interface. The device is intended to be installed on the arm of a precision alignment machine or flip-chip bonder for combined placement and cure / bonding processes. Further to this, the proposed methodology is highlighted. By placing the oven on the arm of a precision alignment platform or flip-chip bonding machine, it is proposed that productivity savings can be made through combination of the placement and curing stages of production. Modification of the excitation source parameters enables materials with higher conductivity to be placed within the oven volume with a reduced likelihood of arcing to the ground-plane.

The conditions required for resonance within the open oven are described within Section 5.3. The change in reflection coefficient of the TM_{33} mode (seen at the dielectric-air interface) is examined as a function of the excitation frequency. The analysis shows that there exists a frequency range where the first few longitudinal variations are cut-off within the air section therefore exhibiting strong resonant characteristics where the normal electric field is large as compared to the transverse field.

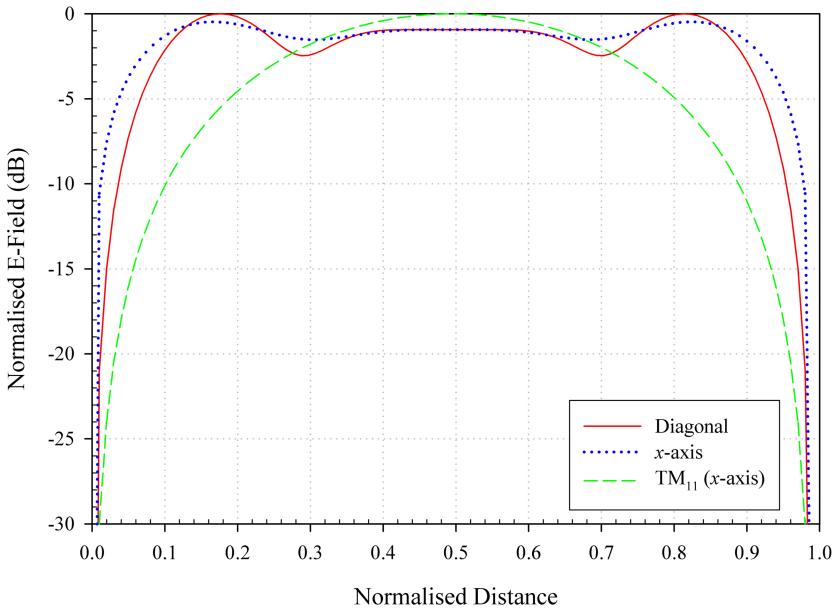

Figure 31: Normalised average electric field through the diagonal and x-axis mid-plane versus normalised distance.

The rate of attenuation of the evanescent field is presented. It is proposed that a change the relative permittivity of the dielectric bulk filling material will allow for control over the rate of attenuation and, to some extent, the depth of *heating*. An analysis is presented showing the change in the rate of attenuation of the field within the cut-off section of waveguide as both the mode order and the relative permittivity of the bulk dielectric are altered.

An analysis of the absorbed power within a lossy pellet or phantom material is described within Section 5.3.2. As the pellet is moved towards the open end (and away from the dielectric-air interface) the absorbed power decays exponentially with distance. Three examples are presented based on differing relative permittivity values. As expected, the higher relative permittivity allows for a greater rate of attenuation and therefore a greater decay in absorbed power with distance.

The functionality of the proposed open oven is described in the context of curing of ECA and solder bumps on die and chip packages. In addition, curing of encapsulant materials is proposed. The alignment principle of the oven is presented for the curing and bonding of packages at the placement stage of production.

Both SFM and VFM field patterns are presented within Section 5.4. Two categories of SFM excitation are highlighted, namely, high order single frequency (SFM_h) and fun-

damental order single frequency (SFM_f). It is hypothesised that excitation of a higher order mode, where the electric field peaks are spatially aligned with ECA bumps, may lead to an even greater selectivity within the heat deposition. A simple field distribution is described and the electric field at the dielectric-air interface examined.

A VFM analysis is described based on well known frequency *hopping* or *stepping* methods. The source frequency is swept across a frequency bandwidth causing scintillation of the modes within the cavity volume. The analysis suggests that the average field pattern (root mean square) can be expressed as a weighted summation of the individual mode field patterns, where the weighting of each field pattern is dependent of the coupling and resident time. It is further hypothesised that, in practice, the average field pattern would consist of a weighted summation of degenerate mode *sets*. An open-ended cavity example is examined where the frequency is swept across the X-band frequency range where a number of distinct modes, based around the TM_{33} mode variation, are resonant. The root mean square of the electric field is calculated using (5.30). The average electric field distribution is approximately unifrom within the centre of the cavity.

CHAPTER SIX

OPEN-ENDED OVEN: EVANESCENT FIELD OPTIMISATION

6.1 Introduction

This chapter addresses a means of optimising the electromagnetic fringing fields at the dielectric-air interface located within the open-ended oven, through inclusion of an additional section of lowloss dielectric material. The permittivity of the new dielectric insert should be greater than that of the bulk dielectric to procure a suitable boundary condition. Adjustment of the length and permittivity of the dielectric insert allows for control of the reflection phase at the bulk dielectric-insert dielectric interface. In doing so, the reflection phase can be altered from that of a quasi open-circuit to a quasi short-circuit. This allows the normal electric field of the TM mode to be maximised at the interface. The insert is best described as a quarter wave matching section.

A figure of merit is defined to provide a quantifiable means of the relating the relative magnitude of the evanescent electric field to the electric field within the bulk dielectric. It is proposed that a more efficient oven is one where the figure of merit is maximised.

An eigenmode solution of a lossless, multi-section cavity is presented. As the length of the dielectric insert is increased, the resonant frequency of the coupled mode under consideration decreases due to the perturbation effect. An eigenmode solution provides a means of calculating the resonant frequency of a mode as the length of the insert is altered.

A plane-wave analysis is formulated based on the theory of multiple reflections from dielectric interfaces within waveguide [126]. The analysis allows the phase of the reflection coefficient, seen at the bulk dielectric-insert dielectric interface, to be calculated as

a function of dielectric insert length. Furthermore, the plane-wave analysis is confirmed through implementation of a simple transmission line equivalent circuit analysis [127].

Finally, a full wave simulation is conducted in order to investigate the change in the dielectric power density within a lossy target sample placed within the open end of the oven for both optimised and non-optimised cavities.

6.2 Optimised Cavity Synthesis and Analysis

The power absorbed per unit volume (Wm^{-3}) due to dielectric loss within a material is given by (5.15). The heat deposition within the load (epoxy, encapsulant or ECA) material can be increased through either increasing the source power (and therefore, the magnitude of the electric field), the frequency of the source excitation or the dielectric loss tangent of the material. If the source power is increased then, not only will the power loss within the load increase, but also the absorbed power within the bulk dielectric. An optimum design would be one that minimises the absorbed power within the bulk dielectric filling material while maximising the absorbed power within the load. As such, the evanescent fields should be increased relative to the electric field within the bulk dielectric.

In order to quantify the performance of the open oven, a figure of merit F (dB) is created and defined as the logarithmic ratio of the relative strength of the electric field maxima within the bulk dielectric region (supporting the resonance) and the electric field at the target location within the cut-off volume of the cavity,

$$F = 20 \log_{10} \left(\frac{|E^m|_{\text{evanescent}}}{|E^m|_{\text{bulk}}} \right) \tag{6.1}$$

where $|E^m|_{\text{evanescent}}$ is the maximum magnitude of the electric field within the evanescent region and $|E^m|_{\text{bulk}}$ is the maximum electric field point within the bulk dielectric. Larger values of F suggest a more efficient oven performance.

In order to take advantage of the longitudinal field enhancement at a dielectric-air interface, the open oven operates best in a TM resonance [121]. In this case, the longitudinal E_z field is dominant for heating. For this polarisation, the dielectric-air interface behaves

as a quasi open-circuit. As a consequence, the normal electric field at the interface is almost a minimum, limiting the magnitude of the evanescent field in the cut-off region. This electric field quasi null significantly reduces F for the open oven.

For TM modes, an effective short-circuit at the dielectric-air interface will shift the maximum of the normal electric field to the interface. Continuity of normal electric flux would then ensure significantly stronger evanescent fields in the air filled cavity [121] and a large increase in F. However, a metal surface is clearly not appropriate, as it will fully confine the fields to the dielectric region. Optimisation of F for the open oven is based on realising an effective boundary condition at the interface of the bulk dielectric with air that reproduces an effective short-circuit, while allowing for field penetration into the open-ended heating chamber. In order to achieve this, a thin insert of loss-loss dielectric, with a higher permittivity as compared to the bulk dielectric, is introduced into the cavity. This insert will effectively perform as an impedance matching section, transforming a quasi open-circuit into a quasi short-circuit.

6.2.1 Eigenmode Formulation

The resonant frequency of a mode within the open-ended cavity oven can be calculated through consideration of the eigenmode problem. Indeed, the resonant frequency of each mode is required for the plane-wave analysis presented in Section 6.2.2. As the length of the dielectric insert is increased, the resonant frequency of the mode under consideration will reduce as the higher permittivity material encompasses a greater portion of the cavity volume.

Within rectangular waveguide the following relationships are valid,

$$k_c = \sqrt{\left(\frac{m\pi}{a}\right)^2 + \left(\frac{n\pi}{b}\right)^2} \tag{6.2}$$

$$k_i = \omega\sqrt{\mu\varepsilon_i} \tag{6.3}$$

$$\beta_i = \sqrt{k_i^2 - k_o^2} \tag{6.4}$$

where k_c is the cut-off wavenumber, k is the wavenumber, β is the propagation constant and a and b the transverse waveguide dimensions. The subscript i denotes the dependance of each quantity on the properties of the material filling the waveguide.

For a lossless material, the electric field E_x and magnetic field H_x of the TM$_{mn}$ mode traveling in the forward direction within a material i is given by,

$$E_x^{(+)} = -\frac{j\beta_i m\pi}{k_c^2 a} p_{mn} \cos\frac{m\pi x}{a} \sin\frac{n\pi y}{b} e^{-j\beta_i z} \tag{6.5}$$

$$H_x^{(+)} = \frac{j\omega\varepsilon n\pi}{k_c^2 b} p_{mn} \sin\frac{m\pi x}{a} \cos\frac{n\pi y}{b} e^{-j\beta_i z} \tag{6.6}$$

The electric field E_x and magnetic field H_x of the TM$_{mn}$ mode traveling in the backward direction within a material i is given by,

$$E_x^{(-)} = -\frac{j\beta_i m\pi}{k_c^2 a} q_{mn} \cos\frac{m\pi x}{a} \sin\frac{n\pi y}{b} e^{j\beta_i z} \tag{6.7}$$

$$H_x^{(-)} = \frac{j\omega\varepsilon n\pi}{k_c^2 b} q_{mn} \sin\frac{m\pi x}{a} \cos\frac{n\pi y}{b} e^{j\beta_i z} \tag{6.8}$$

The electric field at a point within material i can, in transmission line analogy terms, be described as incident and reflected voltages related to a physically meaningful power relation in terms of wave amplitudes [128] through,

$$V_i = V_i^{(+)} + V_i^{(-)} = \sqrt{Z_{o_i}}(p_i + q_i) \tag{6.9}$$

where p_i is the amplitude of the wave traveling in the forward direction and q_i is the amplitude of the wave traveling in the backward direction [within a material i]. Similarly, the magnetic field can be analogised as incident and reflected currents giving,

$$I_i = I_i^{(+)} - I_i^{(-)} = \frac{1}{\sqrt{Z_{o_i}}}(p_i - q_i) \tag{6.10}$$

Referring to Figure 32 and assuming $p^{(1,2)}$ and $q^{(1,2)}$ are the forward and backward traveling waves of the TM$_{mn}$ mode within waveguide Regions 1 and 2, respectively, then the following field relationship must hold at the dielectric boundary.

$$E_x^{(1)} = E_x^{(2)} \tag{6.11}$$

$$H_x^{(1)} = H_x^{(2)} \tag{6.12}$$

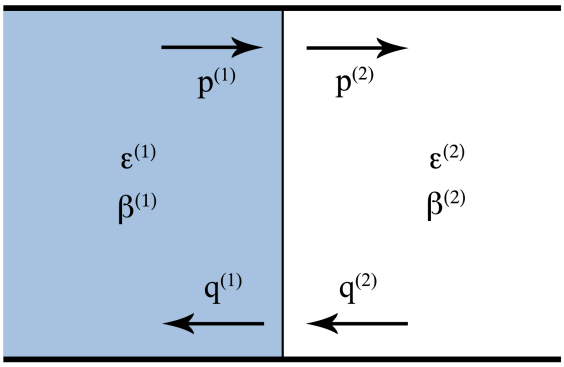

Figure 32: Schematic representation of a material interface with forward and backward traveling waves.

For the E_x field component at the material interface,

$$\frac{-j\beta^{(1)}m\pi}{k_c^2}p^{(1)} + \frac{j\beta^{(1)}m\pi}{k_c^2}q^{(1)} = \frac{-j\beta^{(2)}m\pi}{k_c^2}p^{(2)} + \frac{j\beta^{(2)}m\pi}{k_c^2}q^{(2)} \tag{6.13}$$

$$-\beta^{(1)}p^{(1)} + \beta^{(1)}q^{(1)} = -\beta^{(2)}p^{(2)} + \beta^{(1)}q^{(2)} \tag{6.14}$$

Similarly, for the H_x field component at the material interface,

$$\varepsilon^{(1)}p^{(1)} - \varepsilon^{(1)}q^{(1)} = \varepsilon^{(2)}p^{(2)} - \varepsilon^{(2)}q^{(2)} \tag{6.15}$$

Equations (6.14) and (6.15) can be arranged to give,

$$p^{(1)} + q^{(1)} = \frac{\beta^{(2)}}{\beta^{(1)}}(p^{(2)} + q^{(2)}) \tag{6.16}$$

$$p^{(1)} - q^{(1)} = \frac{\varepsilon^{(2)}}{\varepsilon^{(1)}}(p^{(2)} - q^{(2)}) \tag{6.17}$$

Summation of (6.16) with (6.17) leads to,

$$2p^{(1)} = \left(\frac{\beta^{(2)}}{\beta^{(1)}} + \frac{\varepsilon^{(2)}}{\varepsilon^{(1)}}\right)p^{(2)} + \left(\frac{\beta^{(2)}}{\beta^{(1)}} - \frac{\varepsilon^{(2)}}{\varepsilon^{(1)}}\right)q^{(2)} \tag{6.18}$$

and,

$$2q^{(1)} = \left(\frac{\beta^{(2)}}{\beta^{(1)}} - \frac{\varepsilon^{(2)}}{\varepsilon^{(1)}}\right) p^{(2)} + \left(\frac{\beta^{(2)}}{\beta^{(1)}} + \frac{\varepsilon^{(2)}}{\varepsilon^{(1)}}\right) q^{(2)} \tag{6.19}$$

Equations (6.18) and (6.19) can be reduced into a *Transmission Matrix* relating the forward and backward waves across the boundary interface.

$$\begin{bmatrix} p_i^{(2)} \\ q_i^{(2)} \end{bmatrix} = \begin{bmatrix} A_i & C_i \\ D_i & E_i \end{bmatrix} \begin{bmatrix} p_{i+1}^{(1)} \\ q_{i+1}^{(1)} \end{bmatrix} \tag{6.20}$$

$$\begin{bmatrix} p_{i+1}^{(1)} \\ q_{i+1}^{(1)} \end{bmatrix} = \begin{bmatrix} A_i & C_i \\ D_i & E_i \end{bmatrix}' \begin{bmatrix} p_i^{(1)} \\ q_i^{(1)} \end{bmatrix} \tag{6.21}$$

In the case of the single material boundary presented within Figure 32,

$$A = \frac{1}{2}\left(\frac{\varepsilon^{(1)}\beta^{(2)} + \varepsilon^{(2)}\beta^{(1)}}{\varepsilon^{(1)}\beta^{(1)}}\right) \tag{6.22}$$

$$C = \frac{1}{2}\left(\frac{\varepsilon^{(1)}\beta^{(2)} - \varepsilon^{(2)}\beta^{(1)}}{\varepsilon^{(1)}\beta^{(1)}}\right) \tag{6.23}$$

$$D = \frac{1}{2}\left(\frac{\varepsilon^{(1)}\beta^{(2)} - \varepsilon^{(2)}\beta^{(1)}}{\varepsilon^{(1)}\beta^{(1)}}\right) \tag{6.24}$$

$$E = \frac{1}{2}\left(\frac{\varepsilon^{(1)}\beta^{(2)} + \varepsilon^{(2)}\beta^{(1)}}{\varepsilon^{(1)}\beta^{(1)}}\right) \tag{6.25}$$

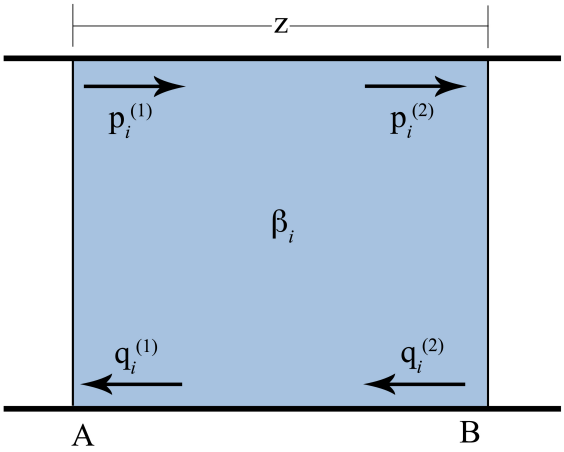

Figure 33: Schematic representation of a phase change between forward and backward travelling waves within a homogenous material.

With reference to Figure 33, the change in phase from point A to point B for the forward and backward traveling waves within a lossless medium is,

$$p_i^{(2)} = e^{-j\beta_i z} p_i^{(1)} \tag{6.26}$$

$$q_i^{(2)} = e^{j\beta_i z} q_i^{(1)} \tag{6.27}$$

From (6.26) and (6.27), the change in the phase due to a length of homogenous waveguide can be expressed as a *Transmission Matrix*.

$$\begin{bmatrix} p_i^{(1)} \\ q_i^{(1)} \end{bmatrix} = \begin{bmatrix} e^{j\beta_i z} & 0 \\ 0 & e^{-j\beta_i z} \end{bmatrix} \begin{bmatrix} p_i^{(2)} \\ q_i^{(2)} \end{bmatrix} \tag{6.28}$$

Since forward and backward waves at the perfect conducting wall and perfect magnetic wall (open face) are known, the overall system matrix can be described through a cascaded matrix of multiple material interface and phase matrices. The overall system matrix is,

$$\begin{bmatrix} p_e^{(1)} \\ q_e^{(1)} \end{bmatrix} = \begin{bmatrix} F & G \\ J & K \end{bmatrix} \begin{bmatrix} p_m^{(2)} \\ q_m^{(2)} \end{bmatrix} \tag{6.29}$$

The quantities $p_e^{(1)}$, $q_e^{(1)}$, $p_m^{(2)}$ and $q_m^{(2)}$ within (6.29) are known and can be found through consideration of the boundary conditions of a TM mode at both a perfect and magnetic conducting walls (Section 3.3.1). For a perfectly conducting wall at $z = 0$, the transverse electric field is zero.

$$p_e^{(1)} = -q_e^{(1)} \tag{6.30}$$

At the perfect magnetic wall (open face of the cavity), the transverse electric field tends to a maximum.

$$p_m^{(2)} = q_m^{(2)} \tag{6.31}$$

Equating $p_{e,m}^{(1,2)}$ and $q_{e,m}^{(1,2)}$ to unity and substituting into (6.29) leads to,

$$\begin{bmatrix} p_e^{(1)} \\ q_e^{(1)} \end{bmatrix} = \begin{bmatrix} F & G \\ J & K \end{bmatrix} \begin{bmatrix} 1 \\ 1 \end{bmatrix} \tag{6.32}$$

At the prefect conducting wall,

$$p_1^{(1)} + q_1^{(1)} = F + G + J + K \tag{6.33}$$

The boundary conditions at the perfect conducting wall are known. Therefore substituting (6.30) into (6.33) leads to,

$$F + G + J + K = 0 \tag{6.34}$$

Having found the roots of (6.34) in terms of β (resonant frequency), it is then possible to use the transmission matrix to find the amplitudes on the air side of the dielectric-air interface. A normalised electric field quantity E_x can be through,

$$E_x = p_a^{(1)} + q_a^{(1)} \tag{6.35}$$

where $p_a^{(1)}$ and $q_a^{(1)}$ are the forward and backward wave amplitudes on the air side of the dielectric-air interface, respectively.

Results from the analytical solution presented above have been compared to the results of the solution of an *eigenmode* solver within the HFSS electromagnetic simulation package. An open ended, two section, cavity with overall dimensions of 24mm x 24mm x 110mm is created within HFSS. The bulk dielectric material has a relative permittivity of 6 and is considered to be lossless. A 5mm air gap is created at the open end thus forming a small recess within the cavity. Perfect electric walls are assumed on all boundaries except the *open* face which is modeled by a perfect magnetic wall. As such, the simulation model can be compared with the analytical solution with confidence. Table 14 displays the resonant frequency and normalised field magnitude on the air side of the dielectric-air

Table 14: Comparison of analytical solution and HFSS simulation for a two section open cavity.

Mode	Analytical Res. Freq. (GHz)	HFSS Res. Freq. (GHz)	Analytical Field Mag. (dB)	HFSS Field Mag. (dB)
$TM_{335^{th}}$	11.201	11.226	-10.46	-7.93

interface for the $TM_{335^{th}}$ mode. The electric field magnitude is normalised to the maximum electric field on the surface of the perfect electric wall adjacent to the open end.

A further comparison is made in order to verify the validity of the solver. An additional *wafer* dielectric insert is placed on the bulk dielectric-air boundary such that a three section open cavity is formed. The insert dielectric has dimensions of 24mm x 24mm x 2.5mm and has a relative permittivity of 12. The field magnitude is calculated on the air side of the insert-air boundary. The results shown in Table 14 and Table 15 show a high degree of correlation between the analytical solution and the HFSS *eigenmode solver* frequency solutions corresponding to an average error of 0.18%. However, the correlation of field magnitude results is lower corresponding to an error of approximately 14%. Further investigation is required to examine the increase in the error in the field magnitude.

Table 15: Comparison of analytical solution and HFSS simulation for a three section open cavity.

Mode	Analytical Res. Freq. (GHz)	HFSS Res. Freq. (GHz)	Analytical Field Mag. (dB)	HFSS Field Mag. (dB)
$TM_{335^{th}}$	11.147	11.170	-4.60	-5.75
$TM_{336^{th}}$	11.305	11.324	-4.36	-5.57

6.2.2 Plane Wave Analysis

The change in the relationship between the electric field within the resonating region and the evanescent region as the length of the dielectric wafer insert in increased can be described through a plane wave analysis [126]. A TM mode in rectangular waveguide is constructed from a pair of parallel polarised plane waves reflecting off the conducting walls, and in the case of a cavity, also off the end walls. A two dimensional schematic of

the process is presented in Figure 34.

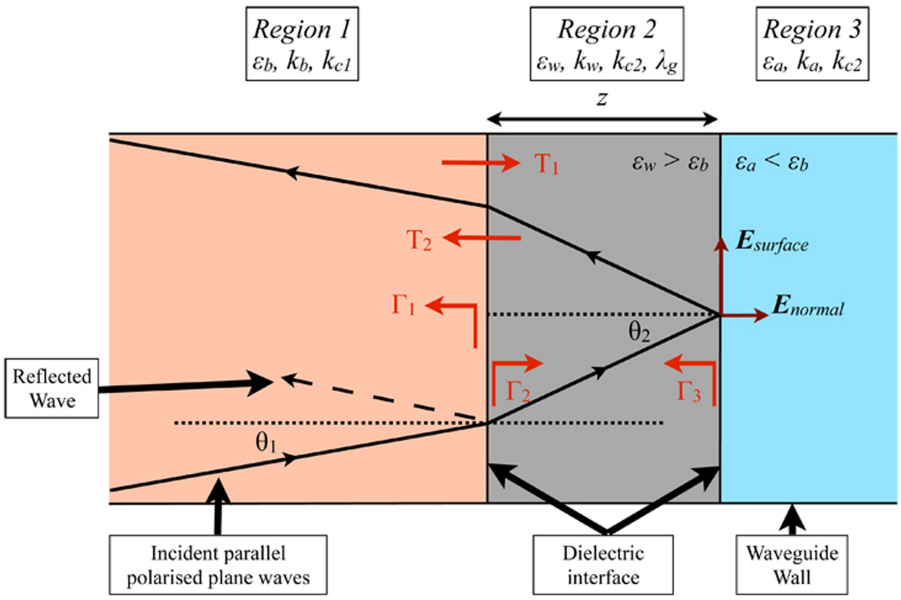

Figure 34: Schematic of the plane wave interaction within a three section waveguide.

Region 1 represents the resonating bulk dielectric portion of the cavity, *Region 2* the dielectric wafer insert and *Region 3* is the cut-off, air filled waveguide. Subscripts b, w and a represent the bulk dielectric, the wafer insert dielectric and the air regions, respectively. In the case of the three section open-ended cavity,

$$\varepsilon_b < \varepsilon_w \tag{6.36}$$

$$\varepsilon_b > \varepsilon_a \tag{6.37}$$

The reflection and transmission coefficients for a parallel polarised plane wave incident on the interface at angle θ are described by,

$$\Gamma_1 = \frac{\frac{1}{\sqrt{\varepsilon_r^w}}\cos\theta_1 - \frac{1}{\sqrt{\varepsilon_r^b}}\cos\theta_2}{\frac{1}{\sqrt{\varepsilon_r^w}}\cos\theta_1 + \frac{1}{\sqrt{\varepsilon_r^b}}\cos\theta_2} \tag{6.38}$$

$$\mathrm{T}_1 = \frac{\frac{2}{\sqrt{\varepsilon_r^w}}\cos\theta_1}{\frac{1}{\sqrt{\varepsilon_r^w}}\cos\theta_1 + \frac{1}{\sqrt{\varepsilon_r^b}}\cos\theta_2} \tag{6.39}$$

$$\Gamma_2 = \frac{\frac{1}{\sqrt{\varepsilon_r^b}}\cos\theta_2 - \frac{1}{\sqrt{\varepsilon_r^w}}\cos\theta_1}{\frac{1}{\sqrt{\varepsilon_r^b}}\cos\theta_2 + \frac{1}{\sqrt{\varepsilon_r^w}}\cos\theta_1} \tag{6.40}$$

$$\mathrm{T}_2 = \frac{\frac{2}{\sqrt{\varepsilon_r^w}}\cos\theta_1}{\frac{1}{\sqrt{\varepsilon_r^b}}\cos\theta_2 + \frac{1}{\sqrt{\varepsilon_r^w}}\cos\theta_1} \tag{6.41}$$

$$\Gamma_3 = \frac{\frac{j\alpha}{k_a}\frac{1}{\sqrt{\varepsilon_r^a}} - \frac{1}{\sqrt{\varepsilon_r^w}}\cos\theta_2}{\frac{j\alpha}{k_a}\frac{1}{\sqrt{\varepsilon_r^a}} + \frac{1}{\sqrt{\varepsilon_r^w}}\cos\theta_2} \tag{6.42}$$

where,

$$\alpha = \sqrt{k_a^2 + \beta_w^2} \tag{6.43}$$

and Γ and T represent the reflection and transmission coefficients from the various dielectric interfaces, θ is the angle of incidence, ε_r is the relative permittivity of the dielectric material, k is the wavenumber, k_c is the cut-off wavenumber, β is the propagation constant, λ_g is the guide wavelength within *Region 2* and α is the attenuation coefficient.

The initial angle of incidence θ_1 is found through,

$$k_b \sin\theta_1 = k_{c_1} \tag{6.44}$$

The angle of incidence of the wave at boundary separating *Region 2* and *Region 3* is given by,

$$\sin\theta_2 = \sqrt{\frac{\varepsilon_r^b}{\varepsilon_r^w}}\sin\theta_1 \tag{6.45}$$

When the TM mode is operating not too far from cut-off then the angle of incidence of the wave impacting the boundary between *Region 2* and *Region 3* is greater than the critical

angle [120] and total internal reflection occurs at the boundary leading to the creation of a strong resonance within the cavity.

$$\sin\theta_c = \sqrt{\frac{\varepsilon_r^a}{\varepsilon_r^w}} \tag{6.46}$$

According to Snells law,

$$\sin\theta_3 > 1 \tag{6.47}$$

In other words, the angle θ_3 loses its physical significance. Total internal reflection occurs at the dielectric boundary separating *Region 2* and *Region 3* and, as consequence, Γ_3 is purely imaginary with magnitude equal to unity.

The reflection coefficient at the dielectric interface between *Region 1* and *Region 2* is a summation of the constituent reflections and transmission coefficients from each dielectric interface. As the initial incident wave hits the first dielectric interface, a proportion of the wave Γ_1 is reflected back from the interface while a proportion T_1 is transmitted. The transmitted wave is subject to a phase shift proportional to the physical length of the dielectric insert before being reflected by reflection coefficient Γ_3. Part this wave is then subjected to a further reflection by Γ_2. This process continues an infinite number of times. The total reflection coefficient Γ is represented by

$$\Gamma = \Gamma_1 + \mathrm{T}_1\mathrm{T}_2\Gamma_3 e^{-j2\beta_b z} + \mathrm{T}_1\mathrm{T}_2\Gamma_2\Gamma_3^2 e^{-j4\beta_b z} + ... \tag{6.48}$$

$$= \Gamma_1 + \mathrm{T}_1\mathrm{T}_2\Gamma_3 e^{-j2\beta_b z}\sum_{n=0}^{\infty}\left(\Gamma_2\Gamma_3 e^{-j2\beta_b z}\right)^n \tag{6.49}$$

Using the geometric progression for $x < 1$,

$$\sum_{n=0}^{\infty} x^n = \frac{1}{1-x} \tag{6.50}$$

leads to a general solution for the total reflection coefficient,

$$\Gamma = \frac{\Gamma_1 - \Gamma_3 e^{-j2\beta_b z}(\Gamma_1\Gamma_2 - \mathrm{T}_1\mathrm{T}_2)}{(1 - \Gamma_3\Gamma_2 e^{-j2\beta_b z})} \tag{6.51}$$

An analytical solution of (6.51) is provided based on a cavity with total interior dimensions equal to 25.5mm x 25.5mm x 120mm excited by a SFM_h excitation. The bulk dielectric material has a relative permittivity equal to 6. Inclusion of the dielectric wafer insert (with relative permittivity equal to 12) will cause a small perturbation of the TM_{334} resonate frequency. As the length of the wafer insert is increased the perturbation will also increase. The change in resonant frequency of the TM_{334} mode as the physical properties of the cavity change is accounted for within the analytical solution of the reflection coefficient. The eigenmode analysis, presented within Section 6.2.1, provides the means of determining the resonant frequency of the system.

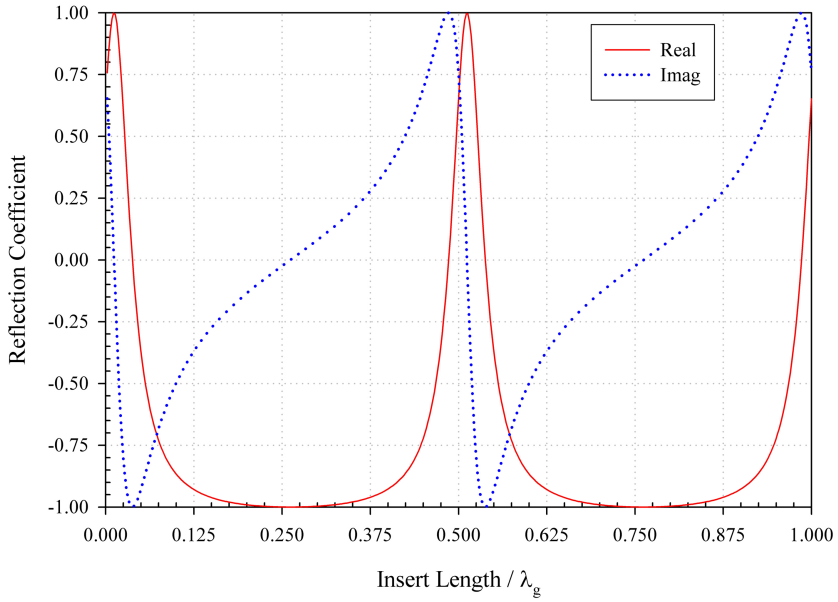

Figure 35: Reflection coefficient versus wafer insert length.

The bulk dielectric dimensions are equal to 25.5mm x 25.5mm x (110mm - *dielectric insert length*). *Region 3* has a length equal to 10mm and is air filled. *Region 3* has a cut-off frequency very much higher than the resonant frequency of the TM_{334} excited within the resonating portion of the cavity. The TM_{334} mode is resonant within the cavity at 10.522GHz. Therefore, the fields that exist within this air volume are evanescent and decay rapidly with distance from the dielectric-air interface in accordance with (5.14).

Figure 35 displays the real and imaginary components of the reflection coefficient Γ versus dielectric wafer insert length z [as a function of guide wavelength λ_g within *Region 2*]. Figure 36 displays a Smith Chart representation of the reflection coefficient as the wafer insert length is increased. Γ has a magnitude equal to unity regardless of the wafer

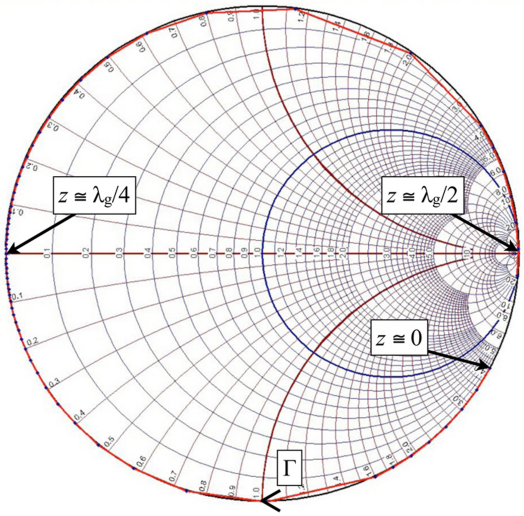

Figure 36: Smith Chart plot of reflection coefficient.

insert length suggesting that the TM_{334} mode remains strongly resonant as the wafer dimensions change. At $z = 0$, Γ can be represented by quasi open-circuit [121]. As the length of the wafer insert is increased, the reflection coefficient becomes less capacitive. At $z \approx \lambda_g/4$, the reflection coefficient is a *perfect* short-circuit. At $z \approx \lambda_g/2$, the reflection coefficient is consistent with the properties of a *perfect* open-circuit.

Table 16: Model geometry and material properties.

Bulk Dielectric	**Dimensions**	18mm x 18mm x 80mm
	ε_b	2.035
	$\tan\delta$	0.0005
Dielectric Insert	**Dimensions**	18mm x 18mm x 3.5mm
	ε_i	6
	$\tan\delta$	0.0005
Encapsulant	**Dimensions**	15mm x 15mm x 0.3mm
	ε_e	4
	$\tan\delta$	0.08

The analysis is extended for a SFM_f excitation. The first two resonant TM modes can be excited within the optimised open oven from considered selection of the excitation frequency. The cavity dimensions are designed based on the preferred order of mode subject to the available dielectric materials. The $TM_{11,1^{st}}$ and $TM_{11,2^{nd}}$ modes contribute to the a SFM_f excitation. In this example, the synthesis of an optimised open oven operating

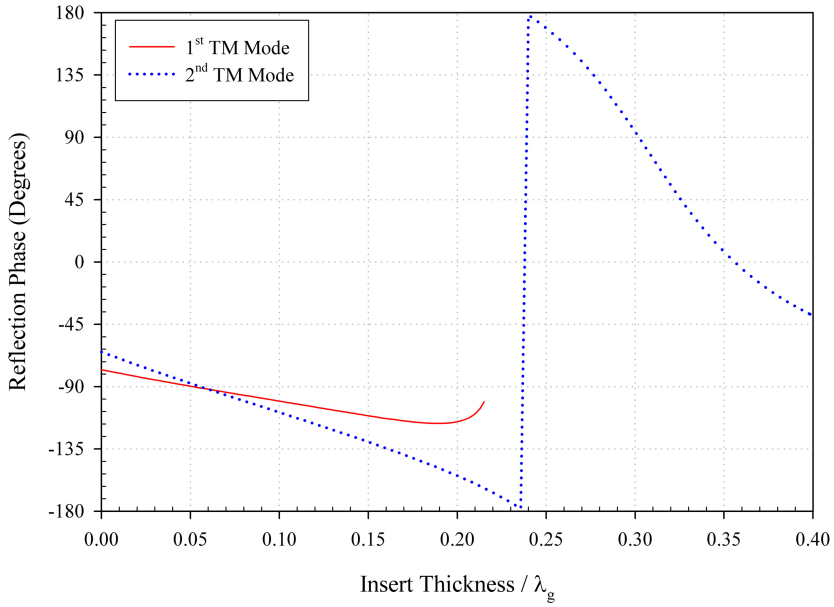

Figure 37: Reflection phase versus the thickness of the insert for the first two TM modes.

between 8.2GHz and 8.7GHz is conducted. For low cost and ease of fabrication, the bulk dielectric filling is chosen as PTFE with relative permittivity $\varepsilon_r \approx 2$. In order to simplify the excitation and identification of the operating mode, operation at lower order modes is preferred, where the spectral lines are sparser. The transverse dimensions of the cavity are 18mm x 18mm, allowing the TM_{11} modes to propagate in the PTFE-filled waveguide ($f_c = 8.13$GHz) while the evanescent region is created in the hollow, air filled section ($f_c = 11.79$GHz). The longitudinal length of the bulk dielectric is 80mm in order to minimise the perturbation due to a small target sample in the heating chamber [121]. The dimensions are summarised in Table 16. For the thin dielectric insert, a lowloss ceramic material with relative permittivity $\varepsilon_r = 6$ is utilised.

The phase of the reflection coefficient Γ versus the thickness of the insert for the first and second order TM modes is shown in Figure 37. As mentioned previously, the magnitude of Γ is unity due to the total internal reflection at the evanescent region. For the second TM mode, insert thicknesses approximately equal to a quarter wavelength (guided wavelength within the insert section), result in a reflection phase of $180°$, corresponding to an effective short-circuit and an optimum insert thickness that maximises F. The reflection phase for the first TM mode is depicted up until about $\lambda_g/5$. For thicker inserts, the resonant frequency of the mode perturbs below the cut-off frequency of the bulk dielectric waveguide section. The optimum reflection phase achieved for this mode is approximately $100°$.

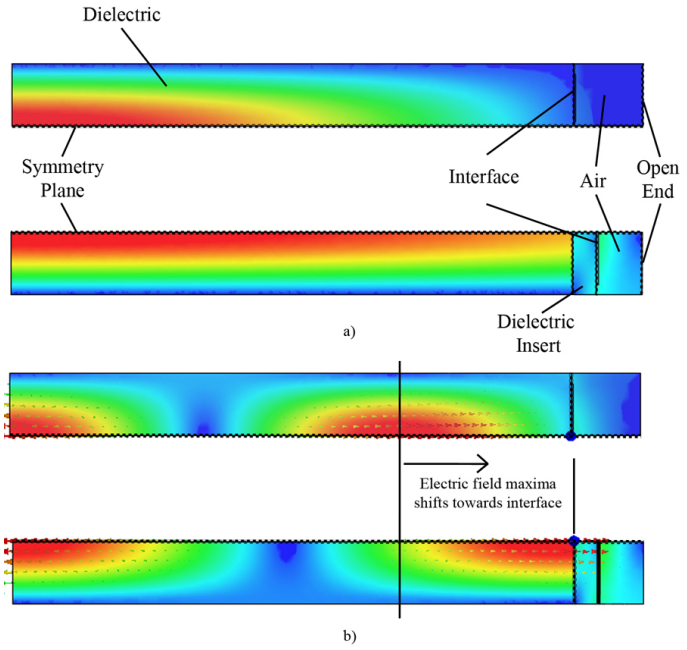

Figure 38: Electric field distribution comparing shift in maxima due to inclusion of an optimise dielectric insert: a) $TM_{11,1^{st}}$ mode b) $TM_{11,2^{nd}}$ mode.

The electric field distribution, simulated using the *HFSS Eigenmode Solver*, for the open oven with and without optimised inserts is shown in Figure 38 for the first and second TM modes. H-Plane symmetry plane allows for one half of the geometry to be simulated. For the case of the cavity with no insert, the field immediately prior to the dielectric-air interface has the properties associated with an open-circuit boundary condition as the normal electric field of the TM mode tends to a minimal value. The effective open-circuit imposes an electric field maximum at approximately a quarter / half wavelength away from the bulk dielectric -air interface for the first / second TM mode. The inclusion of an optimised dielectric insert *shifts* the normal electric field maxima towards the interface, therefore enhancing the strength of the evanescent fields within the air region. Figure 38 suggests that in the presence of the optimised insert, the second TM mode corresponds to a TM_{111} mode established in the bulk dielectric. For the first TM mode, the reflection provided by the dielectric insert does not reach that of short-circuit ($180°$). Therefore, the electric field strength at the interface between the two dielectrics, although improved, is less than optimum as compared to the second TM mode.

The performance improvement of the open oven (by virtue of the dielectric insert) is quantified in Figure 39 and shows F for a range of insert thickness. An improvement of 10dB and 3.5dB is observed for the first and second TM modes, respectively. As the insert thickness extends beyond the optimum value, the figure of merit F drops, with a minimum corresponding to a half guided wavelength, where the insert produces an effec-

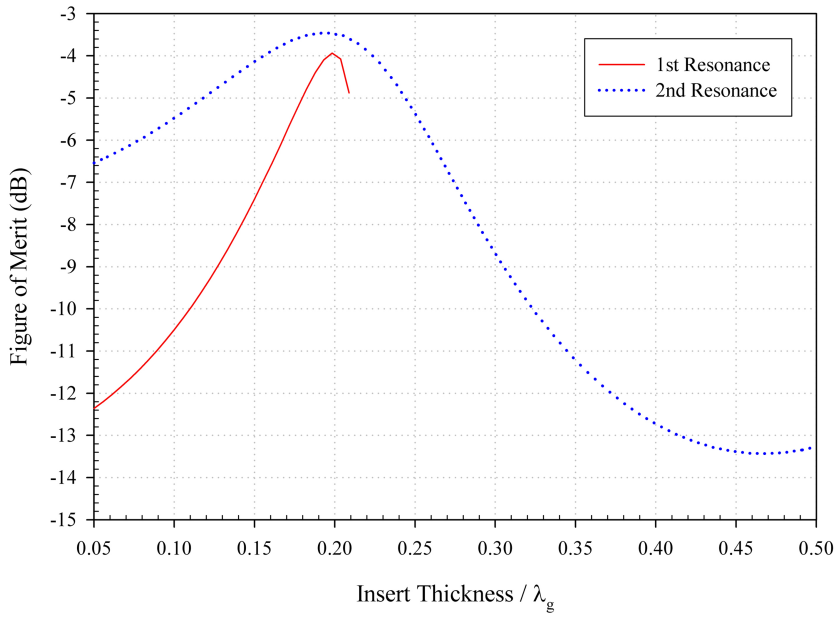

Figure 39: Change in F as a function of insert length.

tive open-circuit boundary condition.

6.2.3 Transmission Line Analysis

A schematic representation of the open oven cavity that includes three uniform waveguide sections (bulk dielectric, optimised insert and air filled heating chamber) is shown in Figure 40 [127]. Variables L, ε, Z and β represent the length, relative permittivity, characteristic impedance and propagation constant of each section respectively. The attenuation coefficient of the evanescent field within the cut-off section of waveguide is α_a. Subscripts b, i, and a correspond to the bulk dielectric, the optimised insert and the air region respectively. Due to the uniform cross section across the cavity, a waveguide mode incident to any of the two planar discontinuities will not excite modes of different transverse order. Therefore the structure can be modelled by a simple cascade of transmission lines with different characteristic impedances Z, as shown in Figure 40. The impedance of each transmission line is determined by the geometrical characteristics and dielectric filling of the corresponding waveguide section, as well as the transverse order of the propagating mode. Since the oven operates at a transverse magnetic mode then,

$$Z_{b,i} = \frac{\beta_{(b,i)}\eta_o}{\varepsilon_{(b,i)}k_o} \tag{6.52}$$

$$Z_a = \frac{j\alpha_a\eta_o}{k_o} \tag{6.53}$$

$$\beta_{(b,i)} = \sqrt{\varepsilon_{(b,i)}k_o^2 - k_c^2} \tag{6.54}$$

$$\alpha_a = -\sqrt{k_c^2 - k_o^2} \tag{6.55}$$

$$k_c = \sqrt{\left(\frac{m\pi}{a}\right)^2 + \left(\frac{n\pi}{b}\right)^2} \tag{6.56}$$

$$k_o = \frac{\omega}{c} \tag{6.57}$$

where η_o is the impedance of free space, ω is the angular frequency, c is the speed of light in vacuum, a and b denote the cross sectional dimensions of the waveguide cavity and m and n denote the transverse order of the waveguide mode. Imaginary values for the characteristic impedance correspond to the air-filled section (heating chamber), since the fields there are below cut-off. In contrast, the characteristic impedances of the bulk dielectric and optimised insert are real. This ensures that the magnitude of the reflection coefficient as seen from any dielectric filled section is always unity.

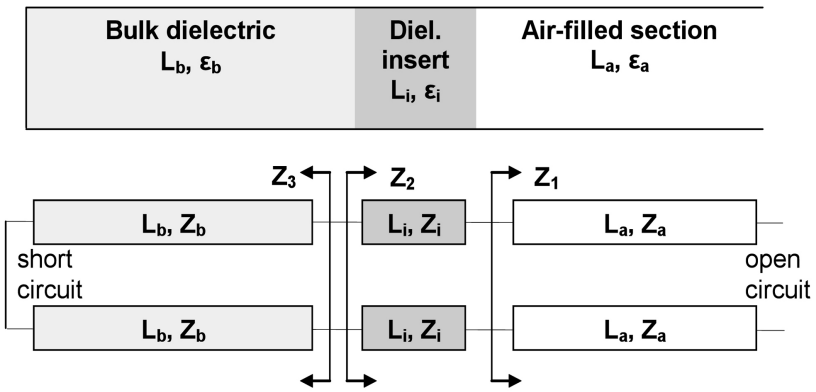

Figure 40: Schematic for a three section cavity with a transmission line equivalent circuit.

Considering the operation principle of the open oven, the length of the air-filled section L_a is assumed sufficient for the evanescent fields to reduce to negligible level at the open end. Therefore, for the purposes of circuit analysis the open end of the cavity is [to a good approximation] modelled by an open-circuit. A short-circuit represents the metallic wall at the close end of the cavity. Upon inclusion of the dielectric insert between the bulk dielectric and the air region, the resonant (operating) frequencies of the open oven are perturbed. The perturbation depends on both the length and permittivity of the dielec-

tric insert. For every dielectric insert, the operating frequency of the open oven can be calculated using the circuit model of Figure 40.

In order to obtain the resonant frequency for an open oven with a dielectric insert, there is the requirement to set-up and solve the eigenvalue problem. The transverse resonance technique is applied to the circuit of Figure 40 [127]. The load impedance Z_1 at the discontinuity between the transmission line (that represent the dielectric insert) and the air-filled section is imaginary and can be obtained by transferring the open-circuit along the air-filled section.

$$Z_1 = jZ_a \cot(j\alpha_a L_a) \tag{6.58}$$

The load impedance Z_2 at the discontinuity between the transmission line that represent the bulk dielectric and the dielectric insert towards the right hand side is,

$$Z_2 = Z_i \frac{Z_1 + jZ_i \tan(\beta_i L_i)}{Z_i + jZ_1 \tan(\beta_i L_i)} \tag{6.59}$$

The impedance Z_3 at the same point towards the left hand side is obtained by transferring the short-circuit along the transmission line that represents the bulk dielectric.

$$Z_3 = jZ_b \tan(\beta_b L_b) \tag{6.60}$$

The resonance condition corresponds to a total admittance equal to zero [129].

$$Z_2 + Z_3 = 0 \tag{6.61}$$

Substituting (6.52)-(6.58) into (6.61), the following eigenvalue problem is obtained.

$$Z_b \tan(\beta_b L_b) + Z_i \frac{Z_a \cot(j\alpha_a L_a) + Z_i \tan(\beta_i L_i)}{Z_i - Z_a \cot(j\alpha_a L_a) \tan(\beta_i L_i)} \tag{6.62}$$

The resonant frequency is obtained upon numerical solution of the eigenvalue equation (6.62). For each eigenvalue (resonant frequency), the field distribution across the three regions can be obtained considering the relative amplitude and phase of the forward and backward waves propagating in the equivalent transmission line (Figure 40). F is readily obtained from the field distribution. Similarly, in order to characterise the effective boundary condition produced by the thin insert, the reflection coefficient Γ seen at the interface with the bulk dielectric is extracted. Simple circuit analysis can be employed as outlined in [129].

The synthesis of an optimised open oven commences from selection of the operating frequency. The cavity dimensions are then designed based on the preferred order of mode subject to the available dielectric materials. The synthesis of an optimised open oven operating between 8.2GHz and 8.7GHz is presented below. The dimensions and properties of the materials within the 18mm x 18mm cavity (described in Section 6.2.2) are given in Table 16.

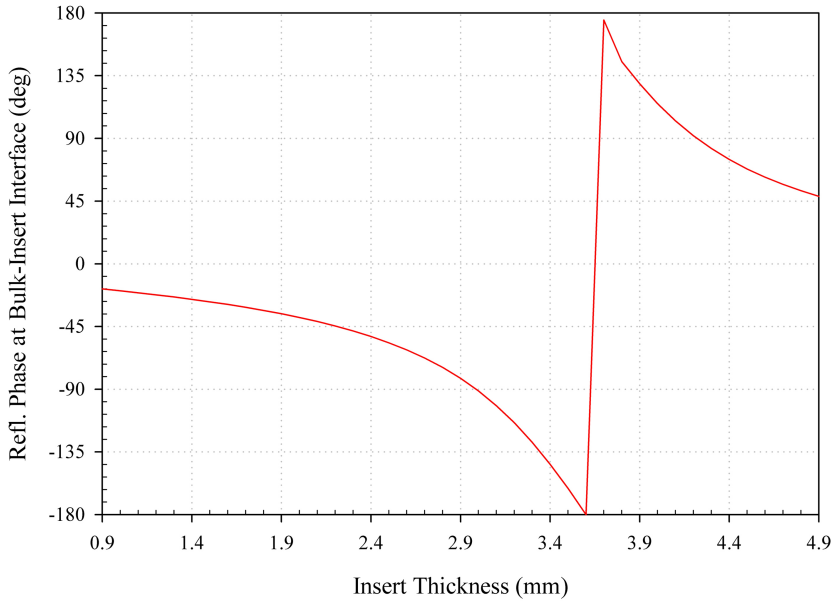

Figure 41: Reflection phase versus dielectric insert guide wavelength based on the transmission line model.

The phase of the reflection coefficient seen in the bulk dielectric at the interface with the air filled section in the absence of any dielectric insert at 8.3GHz is $-8.2°$. This is in agreement with the quasi open-circuit characteristics for this interface described in [121]. Upon introducing a dielectric insert, the phase of the reflection coefficient Γ seen from the bulk dielectric towards this interface is plotted versus the thickness of the insert at 8.3GHz in Figure 41. As mentioned above, the magnitude of Γ is unity due to the total reflection

at the evanescent section. For insert thicknesses approximately equal to 3.5mm, the reflection phase is $180°$, corresponding to an effective short-circuit. As mentioned above, the 3.5mm dielectric insert acts as an impedance transformer in an effective short-circuit. This is expected to shift the maximum longitudinal field in the bulk dielectric at its two ends, hence maximising F.

A concern regarding the performance of the open oven is related to the strength of the fields in the air region away as the target is moved away from the interface [121]. The power [per unit volume] absorbed by a sample versus distance is simulated using Ansoft HFSS. The size of the sample is slightly smaller than the transverse dimensions of the cavity and represents the likely cross-section of an actual package (Table 16). The absorbed power is shown in Figure 42 and is calculated using (5.15). The simulation of the absorbed power allows for a comparison of the open oven with and without the optimising thin dielectric insert for the first TM mode with an excitation of 1W. In sympathy with the attenuation of the electric field within the cut-off section, the power decays exponentially. As a result of the optimised insert, the power levels achieved at the level of the interface for the non-optimised cavity can now be achieved at a distance of 4.5mm [127].

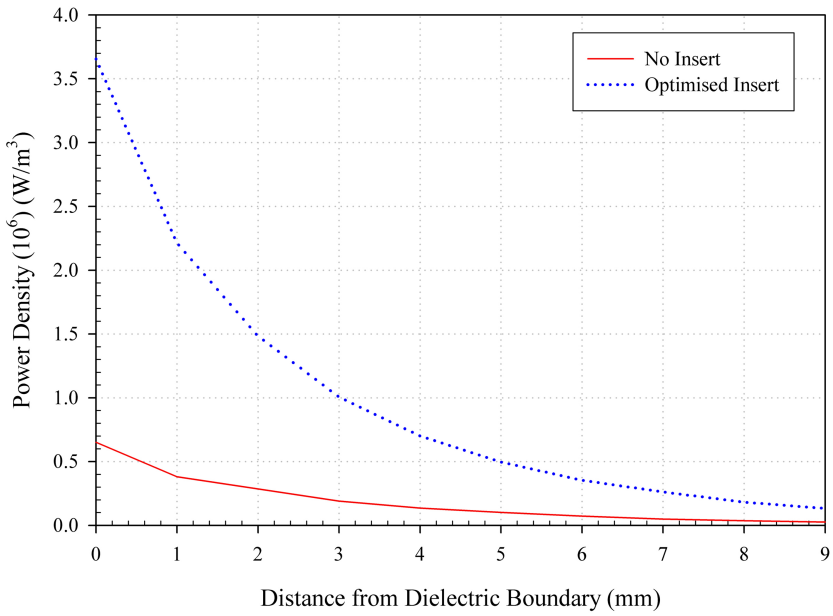

Figure 42: Simulated power density within the encapsulant as a function of location within the evanescent region for the first order TM mode with and without an optimised insert.

6.3 Conclusion

This chapter describes the analysis and synthesis of an open-ended oven cavity using a method for optimising the evanescent fringing field [surface waves] at the dielectric-air interface of the open-ended cavity oven. Through inclusion of a thin wafer dielectric insert, it is possible to control the phase of the refection coefficient seen at the dielectric boundary. The guide wavelength in the insert section is controlled through the relative permittivity of the insert dielectric. Further changes in insert dielectric thickness (length) ensures a means of varying the *path length* of the propagating waves within the insert waveguide section.

A figure of merit is defined based on the logarithmic ratio of the maximum magnitude of the electric field within the evanescent region and the maximum magnitude of the electric field within the bulk dielectric. It is proposed that a increase in F will correspond to a more efficient cavity oven as the fields within the evanescent section will be maximised relative to the fields within the bulk dielectric. Although it is possible to increase the fields within the evanescent section through an increase in source power, this will subject the bulk dielectric to [unwanted] heating effects.

An eigenmode formulation for calculating the resonant frequency of a cavity oven filled with various dielectric materials is presented. It is assumed that each dielectric material fully fills the transverse cross-section allowing a simple analytical solution to be found. As the length of the higher permittivity dielectric insert is increased, the perturbation of the resonant mode under consideration will also increase causing a reduction in the mode resonant frequency. For the plane wave analysis, within Section 6.2.2 to be valid, this change in resonant frequency must be accounted for.

A plane-wave analysis of the multi-section waveguide oven is presented within Section 6.2.2. The analysis confirms that the reflection phase of Γ can be controlled through the change in length of the higher permittivity dielectric insert. It was found that the optimum boundary condition, that produced a maximum in F, occurred for a dielectric insert guide wavelength of approximately one quarter. Furthermore, a minimum value of F occurred for a wavelength of approximately one half corresponding to an improved open-circuit boundary condition. A transmission line analysis was also conducted and went on to confirm the hypothesis presented within Section 6.2.2.

Finally, simulated normalised power density results are presented based on a lossy target sample placed as various points through the evanescent region. The results suggest an almost sixfold improvement in absorbed power for the optimised insert cavity as compared to the cavity with no insert present.

CHAPTER SEVEN

EXPERIMENTAL INVESTIGATION

7.1 Introduction

An experimental investigation into the open-ended cavity oven is presented. Various excitation mechanisms are employed to illustrate degenerate and non-degenerate mode heating. The experimental assessment has focussed on two particular schemes. Firstly, a SFM_h cavity that allows for alignment of electric field maxima with ECA bumps has been constructed. The design is implemented based on excitation of the TM_{33} mode set within the open oven. The optimisation of the evanescent fringing field at the dielectric-air interface is experimentally validated for a non-degenerate SFM_f excitation. Through coupling of the fundamental mode, quasi degeneracy can be avoided due to the sparsity of modal spectral lines thus allowing for a relative comparison to be made between optimised and non-optimised cavities. In principle, the inclusion of a lowloss dielectric wafer insert is valid for any higher non-degenerate mode or degenerate mode set. A curing trial based on encapsulation of a 741 op-amp validates the proposed technology.

Secondly, a VFM cavity, which encourages heavy overmoding and promotes uniform heating of a lossy test sample, has been realised. The source frequency is swept through the X-band frequency range such that quasi degenerate TM modes are arbitrarily coupled into the cavity. In addition, a closed loop feedback routine is implemented enabling the temperature within the test sample to be controlled to a user defined target temperature profile.

Finally, the complex permittivity of an encapsulant paste is characterised versus frequency and temperature. The complex permittivity is not only a function of temperature and frequency, but also degree of cure.

7.2 High Order Mode Experimental Results

7.2.1 SFM$_h$ Excitation

A number of physical models have been fabricated based on the open-ended cavity geometry described throughout this thesis. A significant constraint imposed by the limited availability of equipment is that the source frequency be maintained within the X-band frequency range (8GHz - 12GHz). A travelling wave tube (TWT) is used as the power source and provides 25W continuous wave power through the X-band frequency range. In the course of the experimental investigation, it was found that a maximum power in excess of 35W could be achieved within the lower region of the TWT frequency range (approximately 8GHz - 8.3GHz). The cavity itself has been manufactured from copper [in the case of the SFM$_h$ experiment]. Subsequent models have been manufactured from brass and aluminium. The dielectric bulk filling material consists of a lowloss ceramic composite material. The cross-sectional dimensions of the bulk filling material are equal to the dimensions of the waveguide and, as such, the dielectric material fully fills the transverse dimension of the cavity.

It is proposed that excitation of the open-ended cavity at the theoretical resonant frequency of various TM$_{33}$ modes will create non-degenerate modal field patterns at the dielectric-air boundary such that the corresponding electric field peaks are spatially aligned with solder / ECA bumps [for example] within a chip package. A cavity with dimensions 25.5mm x 25.5mm x 110mm has been fabricated (shown in Figure 45). The bulk dielectric material has a relative permittivity of 6 and dielectric loss tangent of $5\text{x}10^{-3}$ at 10GHz and room temperature. The source power is coupled into the cavity from coaxial cable. A small coupling probe is located on the conducting face adjacent to the open end and is set centrally within the transverse plane. The central conductor length is optimised to give maximum coupling of the TM$_{3,3,3/2}$ mode. (The '$1/2$' variation in the longitudinal plane is due to the quasi open-circuit boundary condition at the dielectric-air interface). The combination of parameters described results in several TM$_{33k}$ modes between 10GHz and 11GHz, a frequency range for which microwave measurement equipment is readily available. The prototype described for the SFM$_h$ experiment was specifically designed to provide a demonstration of the formation of multiple *hot-spots* in the open end.

A version of the experimental set-up is shown in Figure 43. The cavity is isolated from the TWT by a three port waveguide circulator. A load is connected to the isolated port

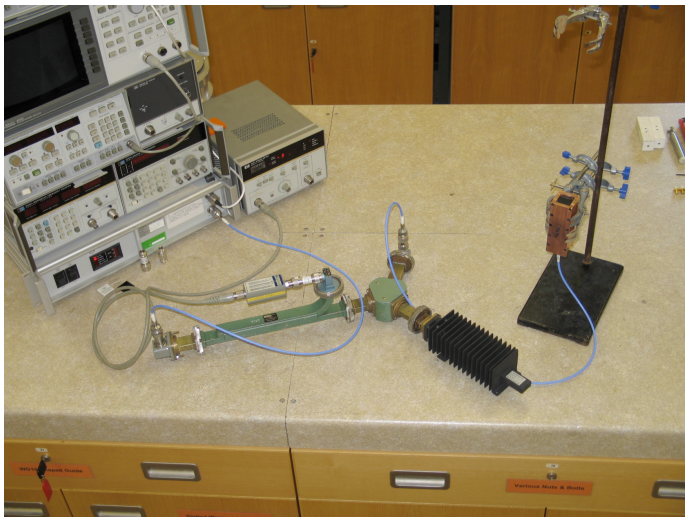

Figure 43: Experimental set-up for SFM_h trials.

of the circulator in order to absorb any reflected power from the cavity thus providing sufficient protection for the TWT. The reflected power is measured using a 20dB directional coupler and power meter located on the coupled port of the circulator. An element of tuning is introduced by adjusting the frequency such that minimum reflected power is recorded on the power meter. This introduces a simple method for ensuring the cavity is excited at resonance. Figure 43 displays the directional coupler located on the input port such that the forward directed power can be measured.

The measured frequency response of the cavity is obtained using a HP8720 Vector Network Analyser (VNA). Having recorded the frequencies at which the cavity is resonant, the demonstrator can then be connected to the high frequency source and corresponding waveguide circuitry. The resulting electric field pattern at the dielectric-air interface is found through introduction of temperature sensitive film placed directly on the surface of the bulk filling material. The film fully covers the transverse cross-section of the cavity. Although the film may be considered as a lowloss material (as compared to a lossy test sample), it was found that areas of the film exposed to high electric field generated a colour variation suggesting an increase in heat within the film. This technology provides a cheap and repeatable method of monitering the experiment.

Measurements on the cavity in Figure 45, with heat sensitive film inserted in the recess and on the surface of the dielectric, indicate (Figure 46) that the $TM_{3,3,5/2}$ mode is present at 10.12GHz. Measured and predicted resonances are shown in Table 17. The temperature sensitive film is designed to display black at 24°C, red at 26°C, green at 28°C and blue at 30°C. The image in Figure 46 indicates power levels which represents approxi-

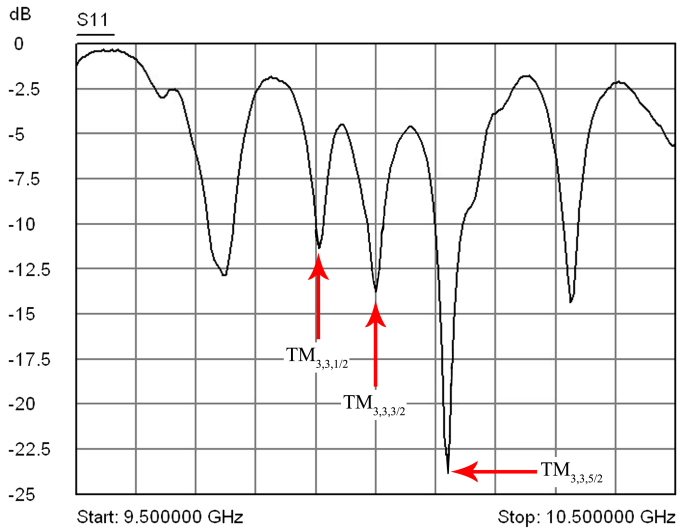

Figure 44: Screen dump from VNA (HP8510b) showing the frequency response of the open-ended cavity optimised for SFM_h.

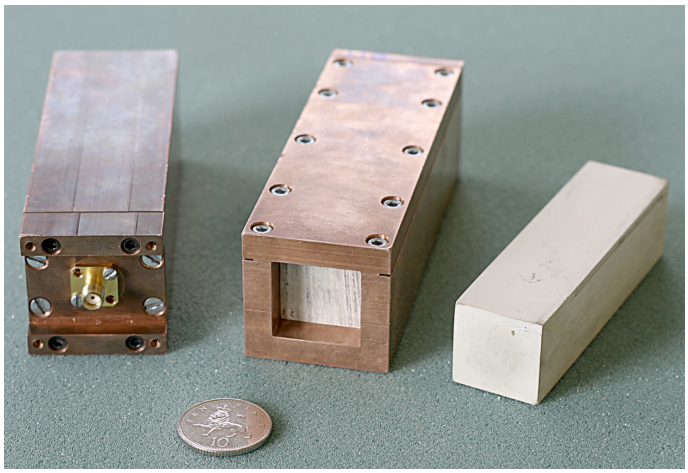

Figure 45: Experimental cavity for SFM_h.

mately 50% drive power (green spots on red background) after 1min.

It is clear that the measured mode shown in Figure 46 is not a *pure* TM_{33} mode as anticipated. This was true of further measurements on other modes. Only eight of the nine pattern peaks can be discerned for the $TM_{3,3,3/2}$ mode. Rather, it is suggested that quasi degeneracy degrades the purity of the field distribution. The quasi degeneracy is attributable to the fact that the available Q levels are insufficiently high, causing the modal fields of neighbouring modal resonances to overlap. The measured Q levels were in the range 200 - 300 for the $TM_{3,3,5/2}$ mode. This could be improved by employing a lower loss dielectric insert and higher conductivity metal cavity walls. Quasi degeneracy can also be suppressed by employing mode selective coupling involving the use of more than one excitation probe [7].

Table 17: Computed and measured TM_{33k} resonant frequencies [in GHz].

Mode	**Simulated** ***(Eigenmode)***	**Simulated** ***(Driven)***	**Measured**
$TM_{3,3,1/2}$	10.0415	10.010	9.905
$TM_{3,3,3/2}$	10.0787	10.045	10.000
$TM_{3,3,5/2}$	10.1530	10.125	10.12

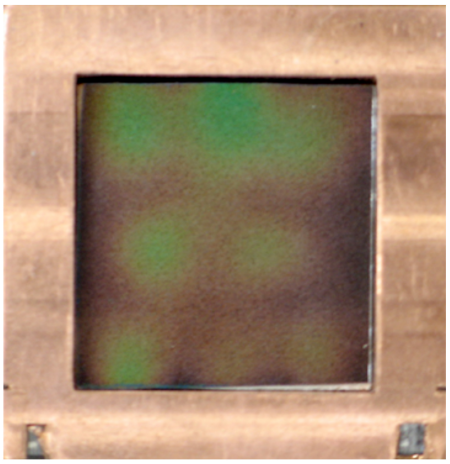

Figure 46: Measured transverse modal patterns in the cavity recess.

The TM_{33k} mode oven with an open-circuit at the open end does not take full advantage of the strong axial electric field formed by the mode when operated not too far from cut-off. If the open-circuit were *perfect*, no normal component of electric field would exist at the interface. The normal E-field within a waveguide cavity maximises in accordance with the TM boundary condition at a perfect conducting wall. Modelling of the cavity with a thin metal layer (thickness of $1/20$ skin depth) deposited on the open interface shows that a strong normal field does penetrate through the metal layer. This has been confirmed experimentally by inserting thin metallised glass slides in the open end of the cavity. Unfortunately the metal layer carries high currents at the power levels required for heating and could easily be burnt off. A more sophisticated impedance wall which behaves like a quasi short-circuit to the transverse fields at the open end of the oven while permitting the normal electric field component at its surface to pass through with minimal attenuation is required to make it possible to demonstrate more efficient heating at high power levels.

The simulations on the TM_{33k} modes in a square cross-section dielectric filled cavity, together with the confirming low power measurements, demonstrate clearly that the successful realisation of an *open* microwave oven is feasible. The heating mechanism depends on harnessing the normal field component of the high order TM mode in the open end. By operating the dielectric filled square cross-section cavity close to the cut-off of the required TM mode, the open end is non-radiating since the constituent plane-waves are incident on the dielectric interface at the open end of the cavity at greater than the critical angle. In this frequency regime the normal electric field on the external surface of the dielectric interface is much higher than the internal field and provides a potential mechanism for efficient heating. For small target packages which occupy only a small portion of the volume of the open end of the oven, the described mechanism remains largely true when heating is performed. Consideration of the relatively low Q levels must be taken into account if a high order non-degenerate mode is to be resonant without significant pattern degradation.

7.2.2 VFM Excitation Incorporating Temperature Control

Epoxy and encapsulant paste manufacturers often described cure schedules based on ramp-up, hold and ramp-down temperature gradients in order to allow for solvent evaporation within the curing process. As such, there is a requirement for temperature control within the open-ended cavity oven system. Experimental studies have been conducted based on a degenerate mode VFM excitation using a prototype system with coupling of arbitrary TM modes located between 8GHz to 12GHz. Optimised power coupling into the cavity over a wide bandwidth (a requirement for VFM) has not been implemented within the design at this stage. Rather, coupling has been optimised for a TM mode resonant at a single frequency. Although far from ideal, results have been generated suggesting the validity of a degenerate VFM excitation scheme for the open-ended cavity arrangement.

A 25W travelling wave tube with protection circuitry and regulated power supply is connected to the cavity through a coaxial transmission line. In this experiment, two 40dB directional couplers are used in order to sample the forward and backward power flow located at the coupling port of the circulator. As such, both the net power flow and the return loss at the cavity input can be calculated.

A thermal imaging camera (Electrophysics PV320) is used to record the temperature distribution within the test sample and provides the basis for a closed loop control routine

implemented using Labview [130]. A temperature profile is specified allowing the temperature within the test sample to be controlled through regulation of the source power. The source is pulsed from an on-state to an off-state as required. A cavity with dimensions 25.5mm x 25.5mm x 110mm is fabricated and contains a low loss, ceramic dielectric material as shown in Figure 45. The dielectric filling has dimensions equal to 25.5mm x 25.5mm x 100mm with a relative permittivity at room temperature of 6 and $\tan\delta$ of 0.0005 at 10GHz. The dielectric is recessed within the cavity at the open end, allowing for an air region of 10mm in length.

The test sample consists of a lead free solder paste placed between two circular coverslips of 15mm diameter and a thickness of 0.15mm. The overall thickness of the sample varies between approximately 0.4mm and 0.6mm depending on the amount of paste included within the test package. This variation in test sample volume has insignificant impact on the electromagnetic performance of the cavity as the perturbation of the resonant frequency for each mode [or mode set] is negligible. The complex permittivity of the lead free solder was measured at room temperature using a dielectric probe (Section 7.5) and was found to have a relative permittivity of 4.6 and $\tan\delta$ of 0.6 at 10GHz. The cavity was excited by a coupling probe located centrally within the transverse plane on the copper end wall.

The combination of parameters described above results in TM modes resonant between 8GHz and 12GHz centred around the TM_{335} at 10.424GHz. The length of the coupling probe is optimised to produce maximum coupling of the TM_{335} mode. The measured magnitude of the reflection coefficient $|S_{11}|$ is -13.2dB. The source frequency is continuously swepted across the X-band frequency with a sweep time of 0.75s. The output power from the TWT is set to give a maximum forward power of 25W. The net power flow incident at the cavity monopole at any particular time during the frequency sweep will depend on the return loss at that particular frequency.

A measurement of the cavity incorporating temperature feedback was conducted. The average temperature over the area of the coverslip is recorded using a thermal imaging camera. A target temperature versus time is plotted (red) over a period of 180s. The source power is automatically adjusted such that the average temperature of the sample corresponds to that of the target temperature. Figure 47 shows agreement between target and measured temperature within the lossy test sample thus demonstrating the validity of the control routine. The average paste temperature is shown in blue. The measurement

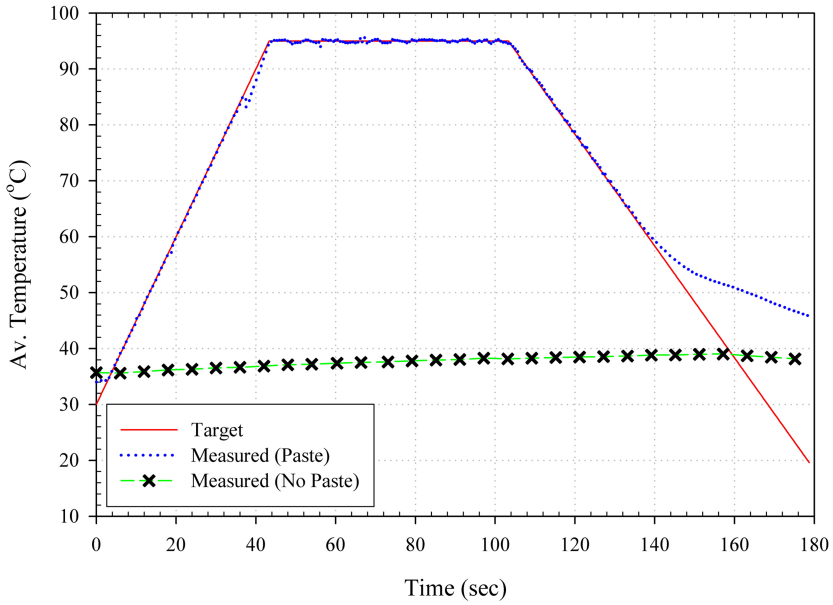

Figure 47: Recorded temperature within a controlled heating trial.

was repeated with no sample present within the cavity (green). It was observed that removal of the sample had a minimal effect on the return loss characteristics of the cavity allowing for comparative power levels to be delivered to the cavity for each experiment. The surface temperature of the dielectric increases by 7°C after 180s. Therefore, the increase in the temperature within the test sample is primarily due to emersion within the evanescent field as opposed to thermal conduction from the dielectric filling material.

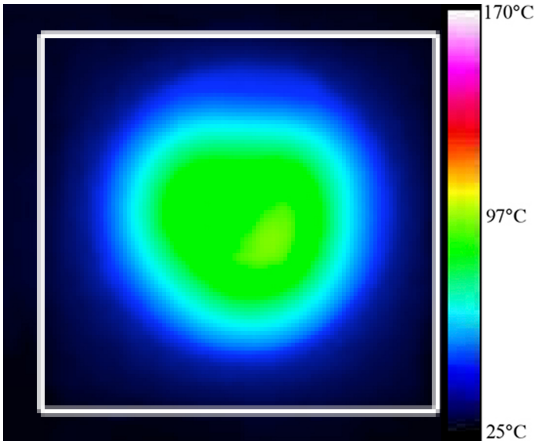

Figure 48: Temperature distribution recorded by the thermal imaging camera.

The temperature distribution within the test sample after 75s is plotted in Figure 48. An approximately uniform temperature distribution is displayed within the test sample. Although the cavity is optimised for the TM_{335} mode, it is clear that the thermal distribution correlates with a uniform pattern as anticipated within a VFM excitation. Further gains in heating efficiency could be made through optimisation of power coupling over a wide

bandwidth.

7.3 Fundamental Mode SFM$_f$ Excitation

In order to demonstrate the performance improvement described in Chapter 6, experimental results based on the open oven design are presented. Performance assessment is carried out by measurements involving the open oven without and in the presence of the optimised insert. Excitation of the cavity is achieved by means of a monopole located centrally at the short circuit end of the cavity. Impedance matching, at the desired frequency, is achieved through adjusting the length of the monopole. The prototype model incorporating the optimised dielectric insert is shown in Figure 49. The system was powered using a 25W travelling wave tube (TWT) at X-band. Two 40dB direction couplers enable the forward and backward power flow to be monitored and therefore the return loss and net power flow to be calculated. The thermal imaging camera, described in Section 7.2.2, is used to visually gauge the thermal distribution at the encapsulant sample over a temperature range of 25°C to 175°C. In this example, no temperature feedback is implemented.

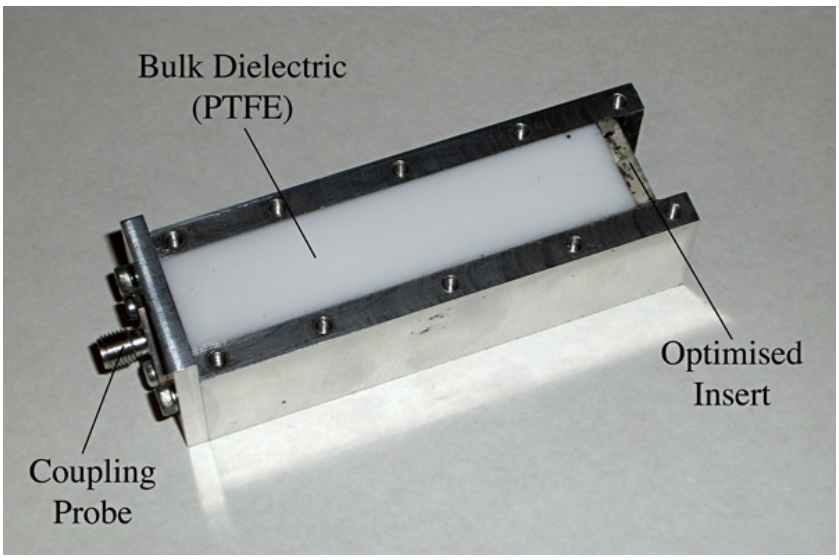

Figure 49: Experimental cavity prototype showing the PTFE, dielectric insert and coupling probe. The top wall of the cavity has been removed.

The cavity is manufactured from aluminium and has inner dimensions equal to 18mm x 18mm x 90mm. The bulk filling material is PTFE while the optimised insert is a ceramic composite material. The PTFE has dimensions equal to 18mm x 18mm x 80mm. It is

desired that the $TM_{331^{st}}$ mode be coupled into the cavity. The length of the coupling probe is altered to provide maximum coupling of the $TM_{331^{st}}$ mode at its corresponding resonant frequency; the length of the coupling probe is 5.3mm. The plane wave analysis in Section 6.2 enables the length of insert to be calculated for optimisation of the evanescent fringing field within the air region of the cavity. For a $TM_{331^{st}}$ mode within the optimised cavity, the length of the insert is calculated as 3.5mm. For the $TM_{332^{nd}}$ mode within the optimised cavity, the length of insert is 3.6mm. The structure is simulated with and without the optimised insert using a high frequency electromagnetic solver. The simulated resonant frequencies for the first and second TM modes are shown in Table 18. The measured reflection coefficient with and without an optimised dielectric insert is shown in Figure 50. The resonant frequencies are identified at the points of minimum reflection. An error of less than 0.4% between simulated and measured frequency results allows for considered identification of the operating modes within the prototype.

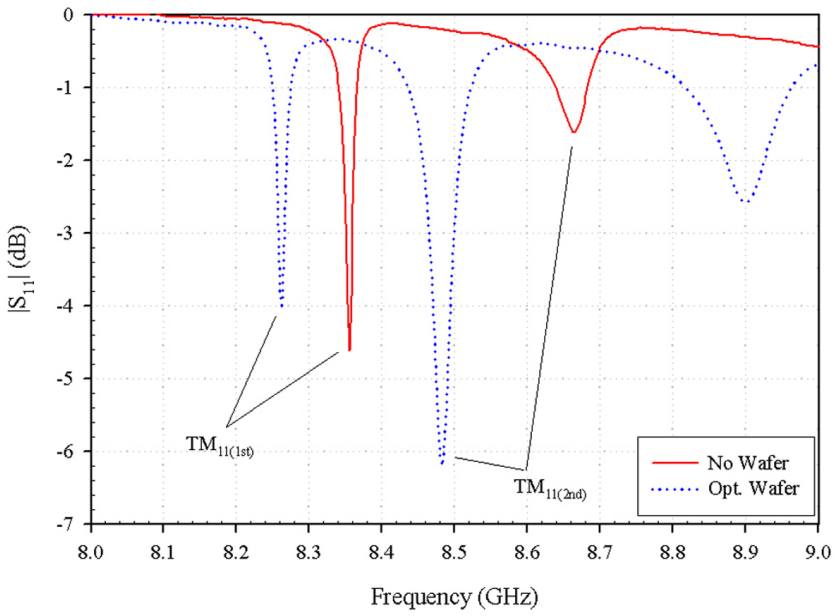

Figure 50: Measured $|S_{11}|$ as a function of frequency.

A commercially available encapsulant has been utilised as a target sample. Its complex permittivity was measured at room temperature through the X-band frequency range using a commercial dielectric probe kit (Agilent 85070E). The encapsulant was found to have a dielectric constant of 4 and $\tan\delta$ of 0.08 at 8.2GHz. The encapsulant was placed between two 15mm x 15mm x 0.1mm coverslips. The overall thickness of the sample ranged from 0.3mm to 0.5mm. In each case, the sample was placed in direct contact with the dielectric-air interface. Two series of measurements (in the presence and absence of the dielectric insert) were conducted. The un-optimised cavity was excited at 8.355GHz

Table 18: Resonant frequency (GHz).

MODE	**SIMULATED (HFSS) (*Driven Solution*)**	**MEASURED (VNA)**
1^{st} TM_{11} - *No Insert*	8.3502	8.335
1^{st} TM_{11} - *With Insert*	8.2648	8.2625
2^{nd} TM_{11} - *No Insert*	8.6295	8.665
2^{nd} TM_{11} - *With Insert*	8.4583	8.4825

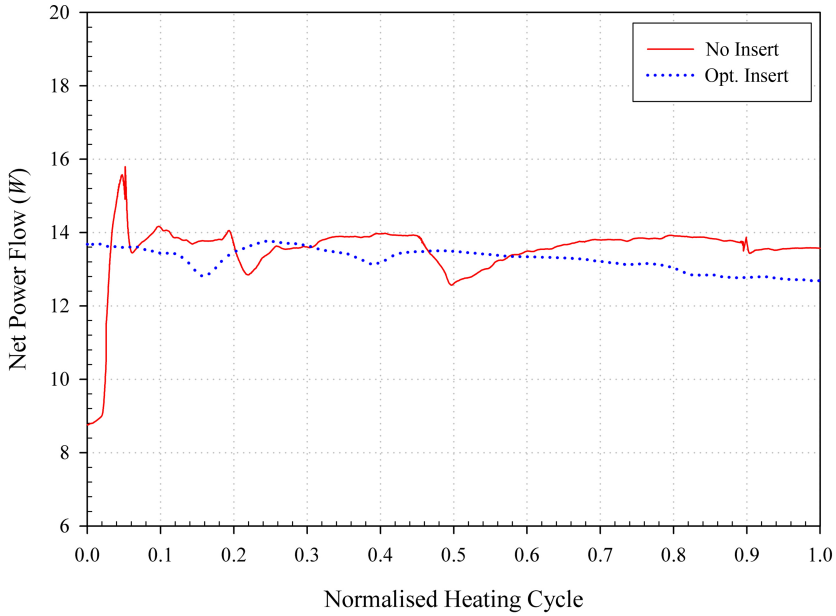

Figure 51: Continuous net power flow versus time.

with a net power flow of approximately 13W for a period of 300s. In the case of the cavity with the optimised dielectric insert, the operating frequency was 8.265GHz with an average net power of 13W. The length of the heating time for the optimised cavity was 30s. Both cavities were operating in the first TM mode.

To ensure comparibility between optimised and non-optimised experiments, it is essential that, in both cases, the cavities are excited on the same mode and with the same net power flow throughout the heating cycle. The net power flow for each case is shown in Figure 51. The source frequency and output power were manually adjusted to ensure that the cavity was excited at resonance with a net power flow of 13W. The increase in temperature of the PTFE through the course of the heating cycle resulted in mild perturbation of the TM mode resonance hence the requirement for small adjustments in frequency and power. Future work will allow this process to be fully automated.

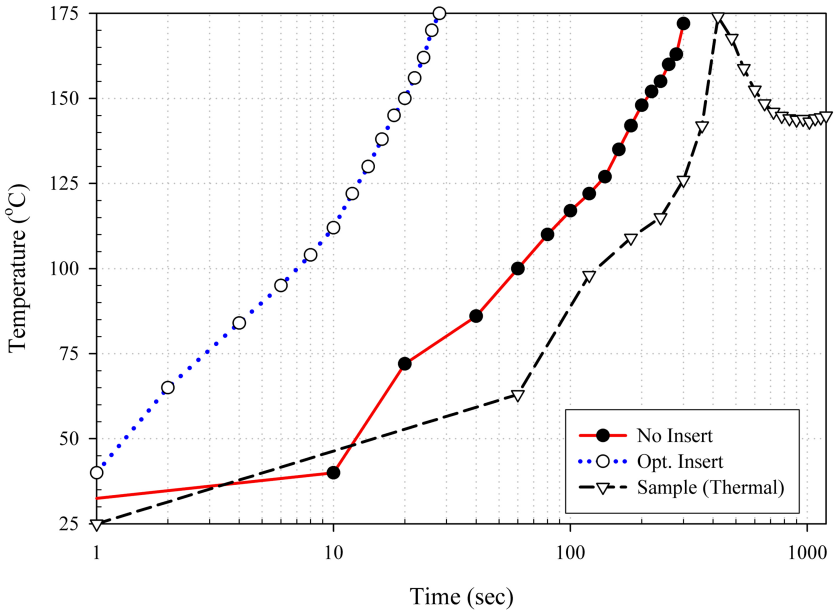

Figure 52: Peak temperature recorded by the thermal imaging camera versus heating time.

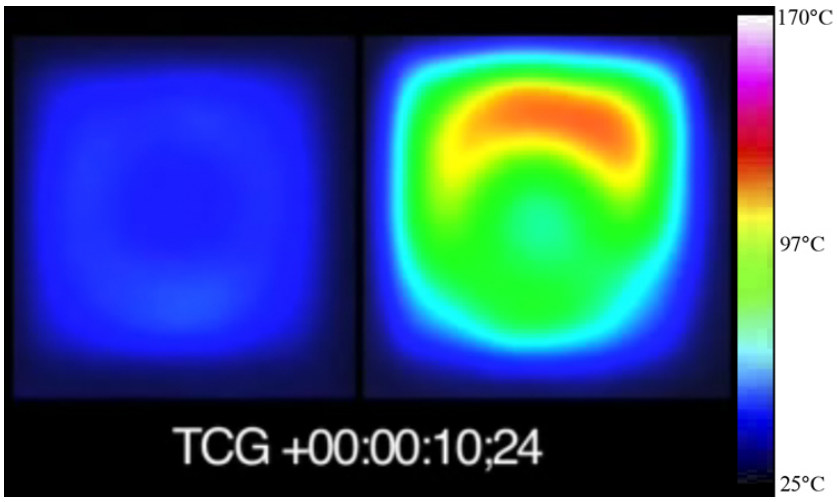

Figure 53: Plot of the thermal distribution within the encapsulant after a heating time of 10s for the un-optimised cavity [left] and the optimised cavity [right].

Figure 52 shows the temperature recorded at the peak location within the encapsulant sample versus time for both cavities. In addition, a plot of the measured temperature of an encapsulant sample cured through conventional convection heating (Section 7.4) according to the manufacturers guidelines is shown as a comparison. The optimised dielectric insert increases the rate of heating by a factor of more than ten over the observable temperature range. The thermal distribution after 10s is shown in Figure 53 for both cavities. The peak temperature on the right hand side is approximately equal to 115°C while, on the left, the encapsulant temperature is approximately 37°C. The non-uniform temper-

ature distribution is attributed to varying thickness of the sample. A threefold increase in the temperature is achieved after the first 10s of the experiment. The performance improvement observed is in agreement with the 9.4dB increase in F, shown in Figure 39 of Section 6.2.2.

It is interesting to note that in order to ensure an almost constant net power flow into the cavity, the source frequency and power were manually adjusted during the course of the heating experiment. This is because, during the course of the experiment, power is absorbed by the PTFE, causing variation of its complex permittivity as a result of the change in PTFE temperature. For the case of the optimised insert, the resonant frequency detuned by approximately 0.5% at peak temperatures. Rigorous treatments of these processes require study of the coupled thermal and electromagnetic processes, as discussed in [123].

7.4 Curing Investigation

Conventional curing of polymer materials for die attach, encapsulation and underfill processes are often conducted within a convection oven incorporating sensitive temperature and humidity controls. It is well known that it is impossible to obtain a 100% cure of epoxy materials as this would require an infinite amount of time! Rather, manufactures state a temperature-time heating profile that allows the material to be held 20°C to 30°C above the glass transition temperature for an amount of time that ensures a 98% - 99% cure of the polymer constituent of the paste. It is often the case that a pre-cure heating cycle will be defined, where a low temperature is described (30% of the glass transition temperature) for a set time, to enable the solvents, used in making the paste viscous, to be evaporated before hardening occurs. Without this process, the solvents become trapped; evaporation occurs as the material hardens forming voids within the polymer volume. These voids are required to be avoided as the structural integrity of the paste reduces leading to reliability issues.

An experiment is conducted to measure the temperature within an encapsulant sample placed within a conventional convection oven (Innovens 77 EU2). The temperature of an encapsulant sample (Henkel EO1080) is recorded using a calibrated wire thermocouple. In addition, a second thermocouple is used to measure the temperature inside of the oven itself. The manufactures cure schedule states that full cure will be obtained if heated at

150°C for 20min. The sample is placed within a pre-heated oven at $t = 0$s and the temperature recorded. It can be seen in Figure 54 that the oven temperature increases steadily through the cure cycle from 90°C to 160°C. The reduced temperature at the start of the cure is a result of opening the door of the pre-heated oven. Of note is the occurrence of a peak within the sample temperature after 7min. The temperature recorded at this point is approximately 25°C higher than the temperature within the oven itself. It is at this point that the exothermic heating catalyst is at a maximum [123]. This cure effect reduces as more polymer material is cured and, as such, the temperature can be seen to steadily reduce to 135°C.

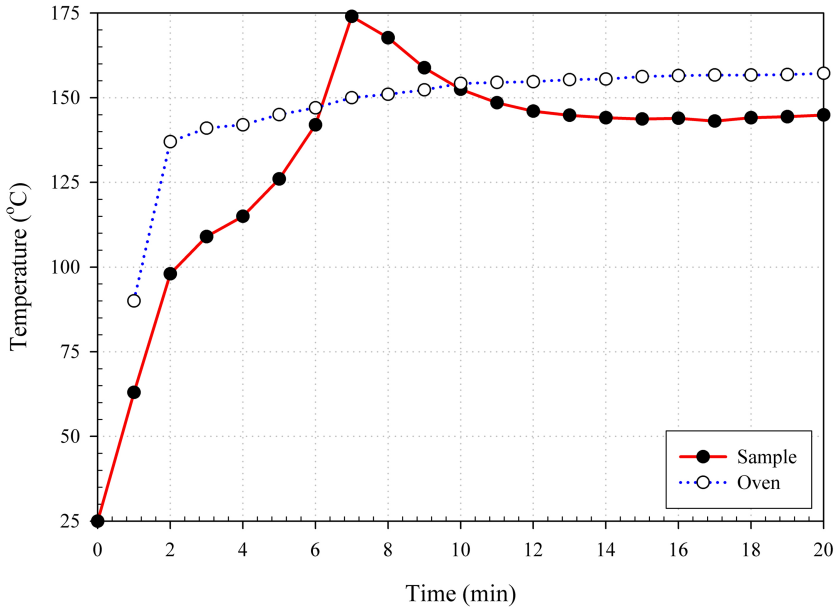

Figure 54: Temperature recorded within a conventional thermal oven and encapsulant sample.

A curing trial using the open oven heating system based on encapsulation of an op-amp chip is presented. The purpose of this experiment is to subject a robust package to strong electromagnetic fields within the cavity volume in order to demonstrate the curing capability of the cavity geometry. A 741 op-amp chip is placed on a circuit board with accompanying resister components. The circuit is arranged such that the 741 amp lies centrally within the transverse plane of the cavity oven; the resistors lie outside of the oven and are not subjected to the heating fields. A small amount of EO1080 encapsulant is placed on and around the 741 chip. The cavity oven is placed in position over the chip such that the component lies within the load section of the cavity oven.

The open-ended cavity with inner dimensions of 18mm x 18mm x 90mm is used within the experiment utilising a SFM$_f$ excitation. The cavity bulk dielectric is PTFE ($\varepsilon_r =$

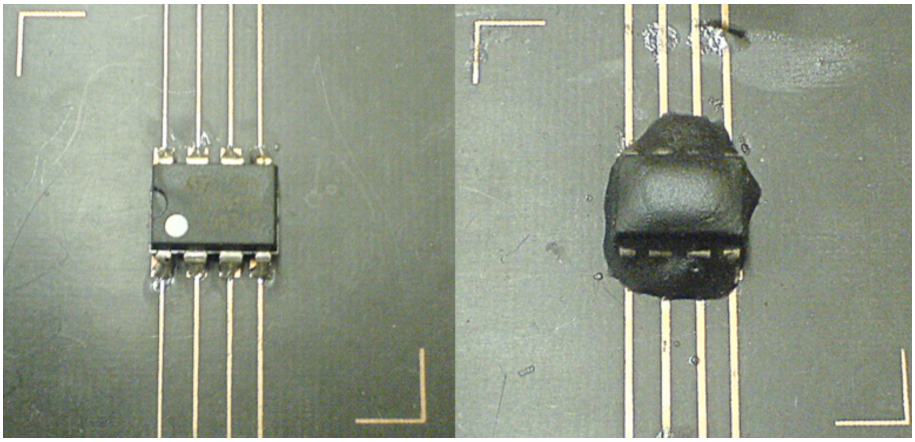

Figure 55: Cured encapsulant surrounding 741 *op amp.*

2.035; $\tan\delta = 0.005$) and has dimensions equal to 18mm x 18mm x 85mm allowing for a 5mm recess at the open face. The cavity itself is manufactured from aluminium ($\sigma = 3.8\text{x}10^6$S/m). The cavity is excited at 8.54GHz corresponding the $\text{TM}_{11(2^{nd})}$ mode. A continuous net source power of 35W is coupled into the cavity using a coaxial probe located on the end wall of the cavity for a period of 2min. Manual adjustment of the frequency and source power during the course of the experiment allows for compensation of perturbation in the resonant frequency due to changes in the permittivity of the bulk dielectric and load caused by an increase in PTFE temperature. Figure 55 shows the op-amp with connecting tracks (left) and the cured encapsulant surrounding the 741 op-amp chip (right). The alignment markers, displayed in Figure 55, correspond to the position of the outer corners of the cavity. It was observed that, once cured, the chip continued to function as expected with no change in operating Gain.

Although a simple and rugged trial, the experiment demonstrates the potential of the system for localised curing of chip packages on a circuit board. It is not expected that packages that are sensitive to electro-static charge will be cured using a continuous wave source. Rather, in this context the viability of operating both a single frequency pulsed source and a VFM source will form much of the future work within this area. Further more, work is ongoing to fully characterise the degree of cure with the encapsulant having cured using the open oven system.

7.5 Polymer Complex Permittivity

A wide range of thermosetting polymer materials, such as encapsulants, underfills and conductive adhesives are utilised in modern microelectronics packaging [131]. These materials are applied as fluids and are hardened through a cure process, requiring heating to initiate or expedite curing. Currently technologies such as infrared, ultra-violet and convection heating are used for this purpose, but can take several hours to perform [132], slowing throughput and contributing a significant portion of the cost of manufacturing.

A problem highlighted within multi-physics modelling is the lack of readily available data from epoxy manufacturers regarding the electromagnetic behaviour of their materials across both frequency, temperature and degree of cure. In particular, data describing the complex permittivity of commercially available epoxy and encapsulants is often limited to a single frequency and a generic pre- and post-cure state. The multi-physics model, described in [123], requires the variation of the complex permittivity of the curing material as a function of both frequency and temperature / degree of cure. In order to fully validate the multi-physics model, an understanding of the material properties during cure is therefore required.

A method of measuring the complex permittivity of encapsulant materials is presented using a commercially available dielectric probe measurement system from Agilent Technologies. The *85070E Dielectric Probe Kit* measurement system, incorporating automatic electronic error compensation, is used to measure the complex permittivity of dielectric materials over a wide frequency range. Within this experimental investigation, the complex permittivity is measured over a frequency range of 500MHz - 18GHz. Inclusion of the optional electronic calibration kit *ECal N469xA Series* enables errors due to *system drift* and *cable instability* to be virtually eliminated while processes can be monitored over long periods (including the testing of materials that vary in both temperature and pressure over time [133]).

The probe is set up and calibrated according to the manufacturer's guidelines, as suggested in [133], using an *air / short / de-ionised water* process. The specified minimum sample size has both radius and depth of 5mm. The encapsulant is contained within aluminium caps, sized to correspond with the minimum sample dimensions. Heating of the sample is achieved through the use of a hot-plate with a potential maximum temperature of 400°C. A calibrated thermocouple probe is used to measure the temperature of the en-

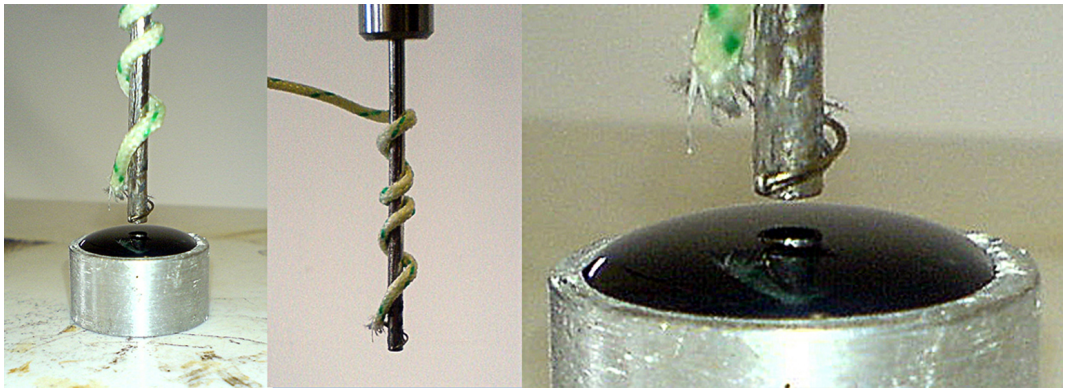

Figure 56: Dielectric probe with wire thermocouple.

capsulant close to the point at which the probe is inserted within the sample. During the course of previous measurements, the encapsulant surrounding the metal probe cured at a slower rate than the bulk of the sample suggesting a lower temperature; in effect, the probe itself acts as a heat sink conducting heat away from the region where the dielectric probe measurement is most sensitive. Observations also suggested that only a very small sample (much less than the size prescribed within the data sheets) could be used within the measurement without significantly altering the results. These factors, coupled together, require that the temperature probe be located as close as possible to the end of probe without being in a position to perturbed the fields as shown in Figure 56. The probe is then inserted up to 2mm within the paste material.

A commercially available encapsulant (*Henkel EO1080*) is utilised as the material under test (MUT). As the encapsulant is slowly heated by the hot-plate, the temperature of the MUT is recorded using the thermocouple and the complex permittivity recorded using the dielectric probe kit. This enables the electromagnetic characteristics of the MUT to be found over frequency, temperature and time. The sample is characterised over a frequency range of 500MHz to 18GHz and a temperature range of 25°C to approximately 160°C.

The relative dielectric constant, loss tangent and measured MUT temperature versus time at a frequency of 8.2GHz are plotted in Figures 57. The temperature of the hot-plate (the source of heating) is slowly increased at an approximately linear rate from 0s to 1150s. Both the relative dielectric constant and loss tangent increase from 5.08 and 0.257 at 0s to 5.9 and 0.36 at 1150s. The measured temperature increases from 25°C at 0s to 96°C at 1150s. At this point in time, the source temperature is held approximately constant for 250s. During this period both the dielectric constant and loss tangent continue to vary

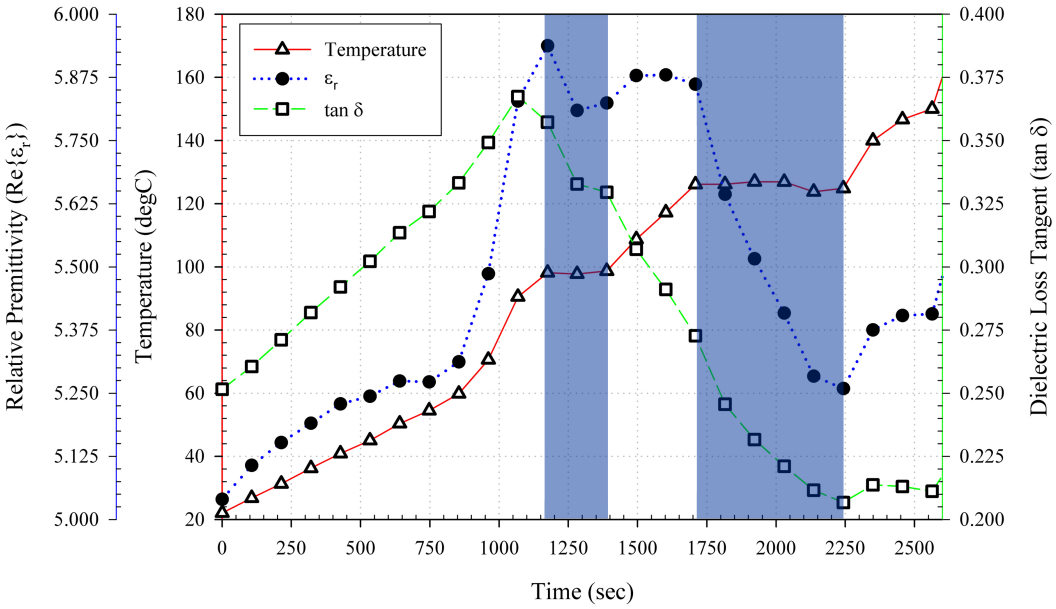

Figure 57: Variation of measured relative permittivity ε_r and temperature of EO1080 encapsulant versus time at a frequency of 8.2GHz.

with respect to time. This process is repeated for a further 550s starting at 1700s. During the second period, where the temperature of the sample is held constant at 110°C, both the relative dielectric constant and loss tangent continue to vary with time reducing from approximately 5.8 to 5.3 and 0.275 to 0.210, respectively.

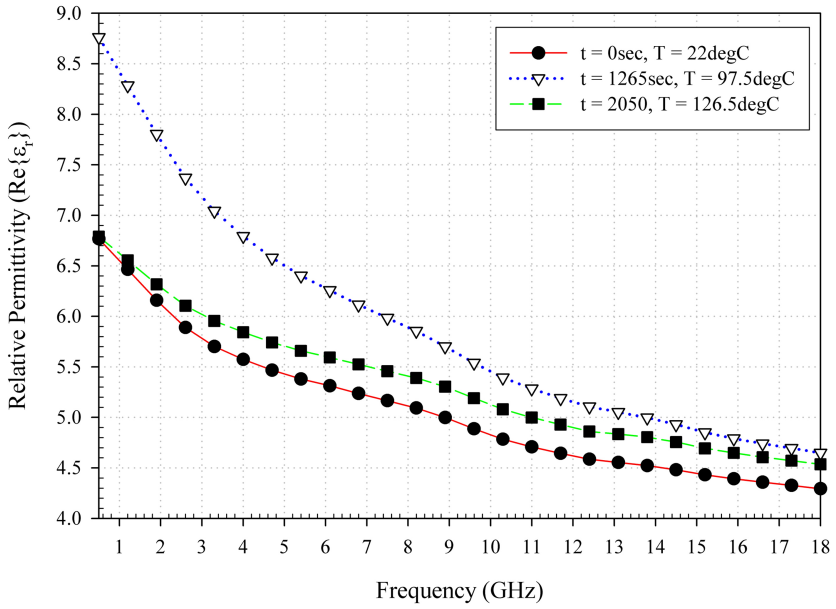

Figure 58: Dielectric constant versus frequency at $t = 0s$, $t = 1265s$ and $t = 2050s$.

The variation in dielectric properties of a polymer material is considered to be a function of both temperature and degree of cure. The rate of variation of the dielectric properties with temperature $\delta\varepsilon_r'/\delta T$ and $\delta\varepsilon_r''/\delta T$ appears to change significantly within the 1250s to

2250s time range. It would seem likely that the material undergoes a significant degree of curing in this time range, with variation in $\delta\varepsilon_r'/\delta T$ and $\delta\varepsilon_r''/\delta T$ resulting from microstructure variation within the polymer material. The temperatures at which the source is held constant have been chosen to be below the glass transition temperature of the MUT in order to highlight the dependance of the complex permittivity on the degree of cure.

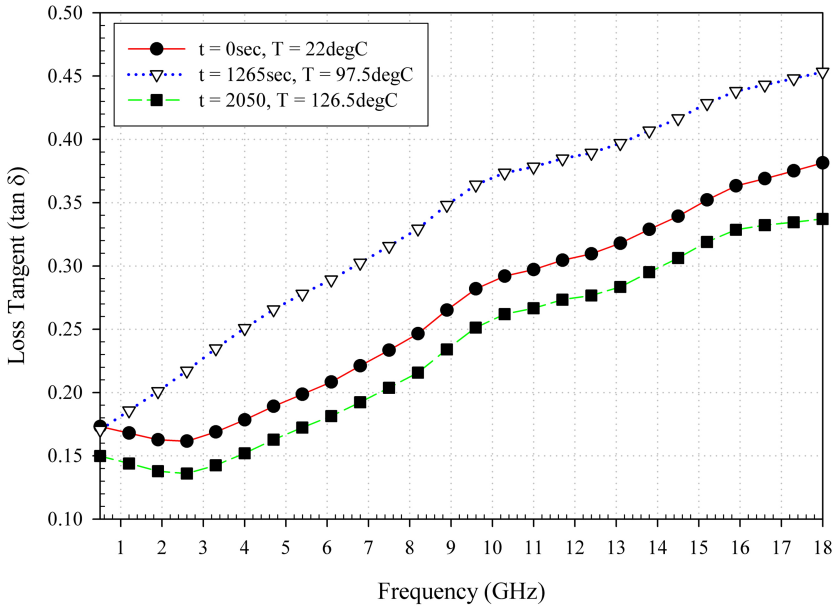

Figure 59: Loss tangent versus frequency at at $t = 0s$, $t = 1265s$ and $t = 2050s$.

The complex permittivity data shown in Figure 57 is measured at 8.2GHz. The experiment has a wide scope in terms of frequency characterisation as MUT complex permittivity can be plotted at any frequency within the measurement range; in this case, 500MHz to 18GHz. The electromagnetic behaviour of the material with respect to frequency is shown in Figure 58 and Figure 59 for three time variations. It can be seen in both plots that complex permittivity is not only dependent on temperature but also frequency. At room temperature (and for t = 0s), the relative dielectric constant varies across the frequency range from 6.8 at 500MHz to 4.3 at 18GHz. The loss tangent varies from 0.17 at 500MHz to 0.38 at 18GHz. Measurement of the complex permittivity over a much wider frequency range, for example 100MHz to 50GHz, may allow for frequency ranges to be identified where the MUT is particularly lossy (in terms of absorbed power) enabling increased level of heating to be obtained.

7.6 Conclusion

This chapter describes the experimental investigation of the open-ended cavity oven. Both SFM_h, SFM_f and VFM excitations are realised within the context of the curing of epoxy and encapuslant paste materials. For SFM_h, it was found that *perfect* electric field distribution of very high order modes was problematic due to the effect of quasi degeneracy of the mode with near-by resonant modes. Although near-by modes are loosely coupled into the cavity, the degradation of the target mode electric field distribution was, in the majority of cases investigated, stark. Rather, it was surmised that low order mode excitation (fundamental mode) would convenient heating of target samples with a predictable and strongly coupled electric field distribution.

A VFM cavity was implemented incorporating temperature feedback control. A closed loop feedback routine was constructed using computer software with appropriate hardware connections allowing a target temperature profile (temperature versus time) to be defined. A thermal imagining camera was used to visually inspect the average temperature within a lossy sample. The closed loop feedback routine allowed for accurate control over the sample temperature. The temperature distribution within the sample was observed to be approximately uniform.

An improved prototype that makes use of a SFM_f operating mode is proposed and includes a thin layer of lowloss, high permittivity dielectric material located at the dielectric-air interface in the open end of the oven has been described. Adjustment of the relative dielectric constant and the thickness is shown to provide an elegant and cost effective method of maximising the evanescent electric field in the open end. Experimental results demonstrate a tenfold reduction in the time required to reach a target temperature and a threefold increase in the temperature achieved in the first 10s. A simple curing trial based on encapsulant of a 741 op-amp chip is conducted. The chip was covered with an encapsulant paste material and irradiated for 2min. The encapsulant was found to have hardened indicated some degree of cure. In addition, the 741 op-amp continued to function after the heating cycle.

The open cavity design and feed circuitry was successful in providing heating of encapsulant samples to temperatures well above the glass transition temperature (typically $125°$C) and with moderate input power levels (up to 35W). Limits of the travelling wave tube, used as the microwave power source, did not permit temperatures higher than $190°$C

within the samples tested. There is no technical reason why higher input power levels could not provide temperatures needed for the reflow of lead-free solder material for example.

Finally, the dielectric properties of an encapsulant material were measured as a function of both temperature and frequency as the material was heated on a hot-plate. It was found that the complex permittivity of the encapsulant material was, not only a function of temperature and frequency, but also a function of the degree of cure. Further investigation is required to produce results highlighting complex permittivity versus degree of cure [123].

CHAPTER EIGHT

CONCLUSION

8.1 Discussion of Results

This thesis describes novel applicators specifically designed to make use of both degenerate and [in one case] non-degenerate mode heating to target microwave energy into small volumes. A systematic approach has been taken in the design of each applicator. Conceptual developments, theoretical descriptions, key benefits and possible limitations are described in detail. A review of the current literature has been conducted and the basic theory which has been developed in the course of the investigation is presented in full.

An innovative applicator for hyperthermia treatment is presented in Chapter 4 based on modal degeneracy. A preliminary examination of modal superposition in a multimode, degenerate mode cavity is conducted. By careful selection of higher order mode sets, it is possible to develop an electric field peak within the centre of the transverse plane leading to a greater selectivity or differential between heating of cancerous tissue and healthy tissue. Forced degeneracy within both rectangular and cylindrical cavities is investigated. It was found that, using the principle of modal degeneracy, useful levels of field focusing can be produced with a small number of higher order modes.

A new configuration of microwave oven is presented within Chapter 5, that utilises both SFM and VFM excitation methods. The applicator is focussed towards the curing of microchip packages. It is intended that the open-ended rectangular cavity (forming the oven) be mounted on a precision alignment machine, enabling the curing of chip packages at the alignment stage of the manufacturing process. Heating within the context of SFM and VFM is described along with the general conditions required to achieve a TM resonance within the oven. A range of frequencies are identified that provide electric field patterns that maintain a strong normal electric field component as compared to the transverse field.

The rate of attenuation of the evanescent field within the cut-off section of cavity is presented. An analysis of the absorbed power within a lossy pellet or phantom material is described. The relationship between the cavity design and the absorbed power is highlighted. The functionality of the proposed open oven is described in the context of curing of ECA and solder bumps on die and chip packages. An investigation into the electromagnetic field distribution of the SFM and VFM excitations is conducted with reference to degenerate and non-degenerate mode heating. It is hypothesised that excitation of a single higher order mode, where the electric field peaks are spatially aligned with ECA bumps, may lead to an even greater selectivity within the heat deposition. A VFM field analysis is described based on well known frequency *hopping* or *stepping* methods. The average field pattern can be expressed as a weighted summation of the individual mode field patterns, where the weighting of each field pattern is dependent of the coupling and resident time. It is further hypothesised that, in practice, the average field pattern would consist of a weighted summation of degenerate mode *sets*. An example cavity is simulated based on excitation with a large number of modes each with ideal coupling. It was found that an average uniform electric field was produced within the centre of the transverse cross-section of the cavity.

Chapter 6 describes the analysis of an efficient and cost effective method for optimising of the evanescent fringing field at the dielectric-air interface of the open-ended cavity oven. A thin additional section of low loss dielectric material is introduced at the bulk dielectric-air interface. Adjustment of the length and relative permittivity of the insert enables the reflection phase at the interface to be adjusted. An effective short-circuit boundary condition can be introduced leading to a maximisation of the normal electric field at the open end. This, in turn, leads to maximisation of the electric field strength of the evanescent fringing field. An eigenmode formulation is used to calculate the resonant frequency of various modes under consideration. The reflection phase is calculated through the use of both a plane-wave analysis and transmission line analysis. It was found that the optimum boundary condition occurred for a dielectric insert guide wavelength of approximately one quarter. The normalised power density within an idealised lossy sample is simulated at various points through the evanescent region. The results suggest an almost sixfold improvement in absorbed power for the optimised insert cavity as compared to the cavity with no insert present.

To underscore the practicability of the focussed heating concept outlined in the thesis, an experimental investigation into the degenerate and non-degenerate mode heating within

the open-ended cavity oven is presented within Chapter 7. For SFM_h, it was found that *perfect* electric field distribution of very high order modes was problematic due to the effect of quasi degeneracy of near-by resonant modes at the design frequency. A VFM excitation was implemented incorporating temperature feedback control. The temperature is monitored through using a thermal imaging camera. A closed loop feedback routine allows the source power to be altered, thus controlling the temperature within the lossy sample. The temperature distribution within the sample was approximately uniform. The cavity including the optimised insert is experimentally verified. Results demonstrate a tenfold reduction in the time required to reach a target temperature and a threefold increase in the temperature achieved in the first 10s. A simple curing trial based on encapsulant of a 741 op-amp chip is conducted. Heating of encapsulant samples to temperatures well above the glass transition temperature was achieved. The dielectric properties of an encapsulant material were measured using a commercially availably dielectric probe kit. It was found that the complex permittivity of the encapsulant material was, not only a function of temperature and frequency, but also a function of the degree of cure.

8.2 Contribution of the Thesis

Degenerate and non-degenerate mode heating has been proposed and verified through theoretical and experimental analysis. The hyperthermia resonator describes a novel method for heating cancerous cells within the human body. It is hypothesised that the tuning of a higher order mode set, such that all modes are forced into degeneracy, will allow for control over the electric field pattern within the resonator. A degenerate mode model, based on summation of the modal field patterns, indicates that the central focus of the electric field is approximately 5 times greater in magnitude as compared to the nearest off-centre field maxima. The central focus has a diameter of 6.25cm within a 2m diameter cavity [according to the standard defined within this thesis]. An experimental model has yet to be fabricate in order verify the theoretical results.

Instead, quasi degenerate and non-degenerate mode heating has been presented in the context of a novel open-ended waveguide cavity oven. It is intended that the oven be attached to the arm of a precision alignment machine such that the bonding and curing steps, within the micro-electronics manufacturing industry, can be performed simultaneously. A plane-wave analysis has been performed to predict field pattern behaviour at

the dielectric interface. A range of frequencies are identified that describe resonance of a high order TM_{33} mode set. Within the defined range of frequencies, the normal field is maximised through the interface. Various parameters that hold relevance to the design of the cavity are quantified.

Quasi degenerate mode heating is presented through a VFM coupling scheme. A model is described based on calculation of the root mean square of the electric field through the course of a frequency sweep. It is proposed that the average field is a weighted summation of the individual modal field patterns. The degree of weighting is dependent on the resident time and amplitude of each mode. It is further hypothesised that, in practice, the modal summation will consist of a number of quasi degenerate mode sets, rather than individual higher order mode patterns. It was found, during the investigation of the non-degenerate mode heating scheme, that excitation of a single, high order mode within a resonant cavity was problematic due to loose coupling of near-by modes. The near-by modes serve to disrupt the idealised pattern of the mode under consideration. Both the forced degenerate mode set and the VFM coupling scheme share a similar field summation behaviour. The net field pattern is a weighted summation of the constituent field patterns.

A method of optimising the evanescent field is described. A quarter-wave matching section is included within the cavity volume. Both VFM and non-degenerate mode heating are confirmed through experimental verification. The open-ended oven technology has formed the basis of a patent [134], [135]. The patent describes the preferred embodiments of the technology, the general cavity geometry, a variety of optimisation methods (including introduction of the optimised wafer dielectric described within this thesis), the proposed benefits and applications to other areas within the micro-electronics industry.

8.3 Future Work - Open Oven Heating Applicator

Several steps are involved to get from the proof-of-concept oven multi / single mode oven demonstrator to a final product. It is anticipated that many of the design parameters will be driven by the physical characteristics of package as well as the type of cure to be performed. For example, the physical size of the package will dictate the cross-sectional dimensions of the oven. The relative permittivity of the bulk dielectric and coupled mode order will, in turn, dictate the frequency of operation. As discussed previously, the atten-

uation of the evanescent field and magnitude of the source power will affect the depth of heating. The designer must account for these factors within the cavity design.

8.3.1 Mode of Operation

Depending on the nature of the devices to be cured, the open-oven is proposed to operate on either a pulsed mode or a frequency swept mode set (VFM). A major area of investigation is the electromagnetic sensitivity requirements of the package. It is key that charge build-up is minimised to reduce the potential for arcing within the package. In the case of pulsed operation for SFM, the key research effort is to identify the pulse repetition rate as well as the pulse duration that will ensure efficient heating of the sample but ensure minimum charge build-up. For the frequency swept mode set, the challenge is to identify suitable modal patterns, also considering degeneracy and excitation of the cavity itself.

8.3.2 Cavity Coupling

A major research and design task is required to identify optimum frequencies and modes of operation. The excitation mechanism is strongly dependent on the order of the operating mode as well as the frequency. Higher order mode excitation is likely to require a more complex feeding, possibly a combination of probes, which need to be customised for each open oven.

Frequency swept operation requires a broadband matching arrangement capable of exciting all desired modes. This poses significant challenges in the design of the coupling devices. In order to maintain a high system efficiency, the coupling from feed network to cavity must be wideband and exhibiting a return loss level that ensures optimum use of available power. An alternative method of coupling to the cavity is through slotted apertures from waveguide. Aperture coupling offers the possibility of efficiently coupling a greater number of high order modes. However, waveguide is rather less flexible as compared to coaxial cable making the potential for integrating the oven into a placement system for a curing application more problematic.

A *concept* coupling geometry is presented in Figure 60 where an open cavity is fed by four slotted waveguide transmission lines. The slots within each transmission line could be optimised to provide maximum coupling at a number of frequencies not unlike the performance of a wideband waveguide to waveguide directional coupler. The source power is

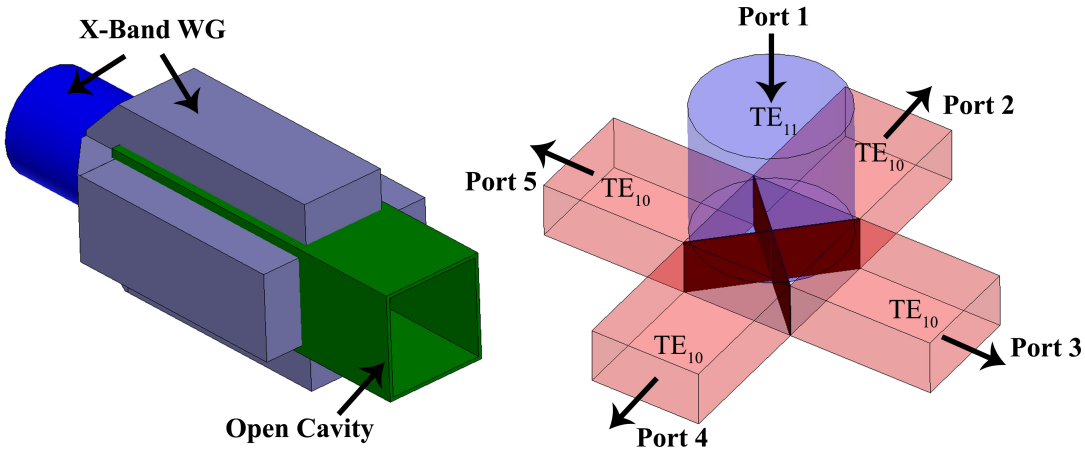

Figure 60: Schematic of 4-way splitter for wideband aperture coupling into the open oven.

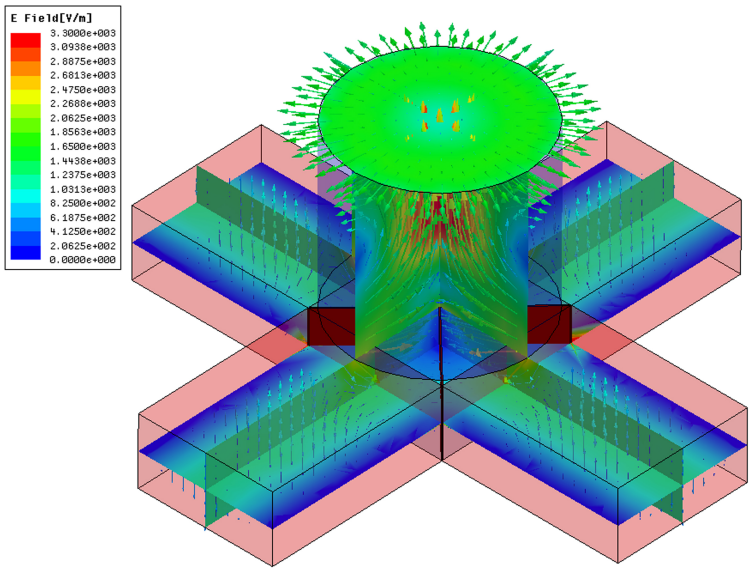

Figure 61: Average electric field distribution within the splitter.

split four ways through implementation of a cylindrical waveguide to rectangular waveguide transition. A thin metal cross provides a means of coupling the TE_{11} mode [within the cylindrical waveguide] to the TE_{10} mode [within each of the rectangular waveguides (Figure 60)]. Although the structure is only presented as a concept device, it is clear that further investigation of the geometry is merited in order to fully characterise its potential as a wideband feed mechanism for VFM coupling.

A full-wave electromagnetic simulation program (Ansoft HFSS) is used to model the performance of the four-way waveguide splitter. If the TE_{11} mode is incident within the cylindrical cavity, then the incident wave is evenly split between the four rectangular waveguide coupling transmission lines, as can be seen in Figure 61. Figure 62 displays the frequency response of the coupling device from 8GHz to 12GHz and 8.5GHz to 10.5GHz,

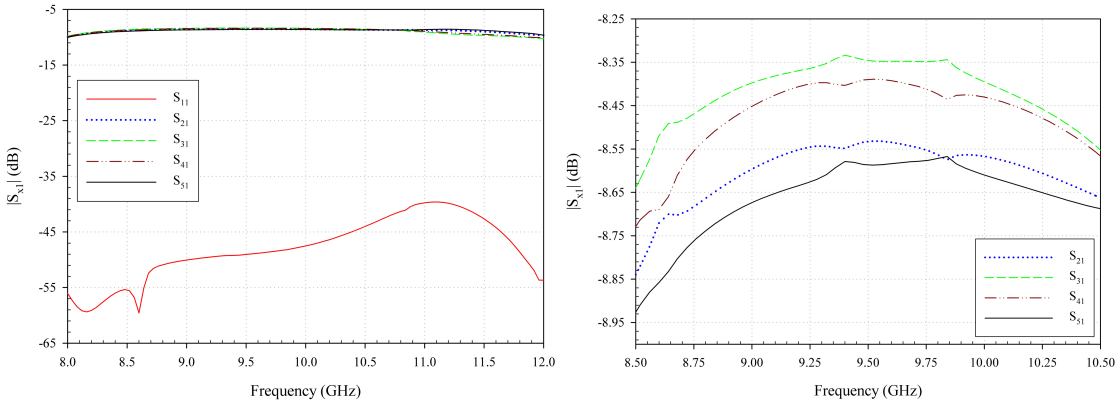

Figure 62: $|S_{11}|$, $|S_{21}|$, $|S_{31}|$, $|S_{41}|$ *and* $|S_{51}|$ *versus frequency.*

respectively. $|S_{11}|$ is less than 37.5dB across the X-band frequency range indicating very good impedance matching. $|S_{21}|$ through to $|S_{51}|$ are approximately equal, suggesting an even power split between each port, varying from -9dB to -8.35dB through 8.5GHz to 10.5GHz. A perfect 4-way power splitter would have a -6dB split from the incident port to each of the coupling ports. The degradation in the coupled split can be attributed to losses within the cavity walls and the thickness to the metal vain at the transition between the cylindrical waveguide and rectangular waveguide.

8.3.3 Quality Factor Considerations

The quality factor of the bulk dielectric filling material is critical in determining the efficiency of the open oven. Thermal losses in the bulk dielectric suggest temperature increase, which can lead to variation of its complex permittivity properties. Significantly, for long continuous operation, heat build up in the bulk dielectric can raise the temperature of the cavity itself beyond prescribed levels. For SFM_h excitation, inclusion of a lossy bulk dielectric material increases the likelihood of pattern degradation due to coupling of unwanted nearby modes. To account for these factors, the investigation should focus on possible solutions to maximize the Q-factor at resonance. These include the introduction of low-loss dielectrics. Alternatively, the utilisation of an air-filled cavity, with tapered cross-section dimensions, could provide a suitable solution.

8.3.4 Lightweight Version

A lighter version of the open oven is planned that would be suitable for mounting on the arm of a precision machine. The device should be as lightweight as possible in order to reduce the inertia of the cavity while in motion. A high inertia, introduced through either

a heavy cavity or high arm acceleration, increases the strain on the placement system. Reduced weight will permit increased arm speeds thus enhancing overall throughput within the manufacturing process.

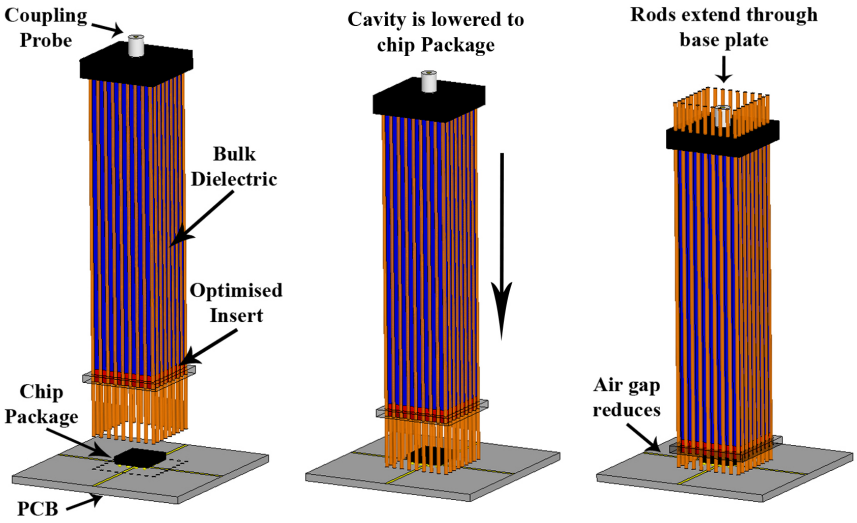

Figure 63: Proposed operation of the concept needle cavity.

A concept device is suggested here based on the open-ended cavity design described within Chapter 5 and Chapter 6. A *needle cavity* is proposed. The design is based on thin rods protruding from a base plate, as shown in Figure 63. The rods are mounted such that they extend *through* the base plate (where the coupling mechanism is located) when lowered onto a circuit board. Structural stability is provided through inclusion of a further metal frame located towards the open end of the cavity. The cavity is filled with a bulk filling material and an optimised insert. As the cavity is lowered into place, the rods will extend through the base plate thus reducing the length of the air filled recess. In effect, the package will be moved through the evanescent fringing field. The continuity of the rods through the longitudinal direction ensure the magnetic current flow is not disrupted. As such, a TM resonance is created within the interior of the cavity with no field present on the outside. This arrangement significantly reduces the weight the original design.

A needle cavity is designed to mimic the performance of a 18mm x 18mm x 100mm SFM_f cavity. 32 rods with a diameter of 1mm are placed in a rectangular arrangement around the outside of the bulk dielectric with an equidistant gap of 1.25mm. The rods have an overall length of 102.5mm. The bulk dielectric material has a relative dielectric constant of 2.0355. An optimised insert is introduced at the bulk dielectric-air interface. The synthesis procedure outline in Section 6.2 is used to calculate the length of insert that corresponds with optimum fringing field strength. The insert itself has a relative permit-

tivity of 6. It was assumed that the performance of the needle cavity matches that of a solid wall cavity.

The first two TM modes are simulated using a full-wave simulation package (HFSS). Figure 64 displays the frequency response of the cavity from 8.6GHz to 9.5GHz. The length of the coupling probe is altered such that maximum coupling is achieved. The coupling probe is 12.25mm in length. The first TM mode is resonant at 8.762GHz while the second mode resonant at 9.181GHz. The electric field distribution of the second TM mode shown in Figure 65. It is clear that the electric field is confined to the interior of the cavity. An electric field is present at the interface between the bulk dielectric and insert dielectric indicating an optimum field penetration into the cut-off section of waveguide.

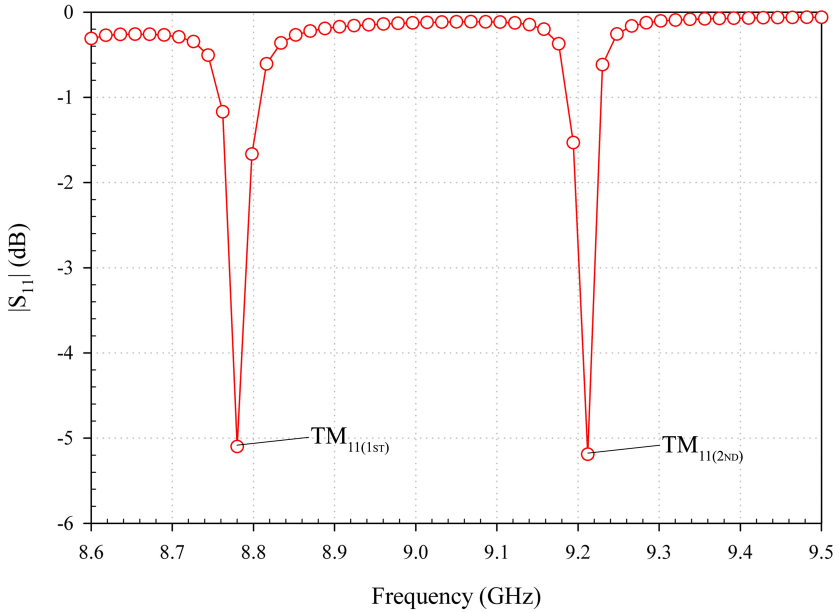

Figure 64: Simulated frequency response for the first two TM_{11} modes.

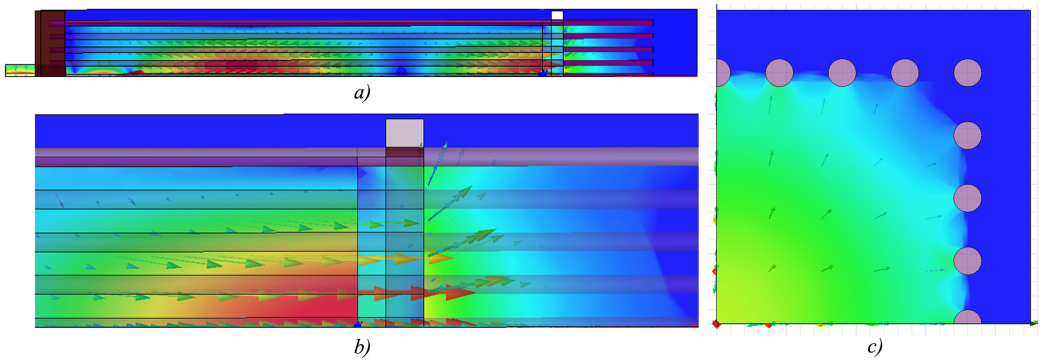

Figure 65: Simulated electric field magnitude and vector for the second TM_{11} mode.

8.3.5 Spectroscopic Assessment of Curing

Fourier transform infra-red (FTIR) spectroscopy is proposed for the comparison between the microwave cure achieved by the open-ended oven and the cure based on conventional thermal heating processes. In addition, a number of tests should be done in order to fully characterise the quality of bond between chip and die and the effect on the performance of the IC package itself. These test include hardness test using nanoindenter, the Scotch tape test, the scratch test and the shear test. In addition to this, it is proposed that the packaged dies in a thermal cycling oven (temperature cycle) be submitted to assess the reliability of the bonds.

APPENDIX A

Table 19: VFM Mode Set.

TM Mode			Frequency	Magnitude
m	n	l	(GHz)	at Interface
2	2	6	8.0072	0.5799
3	2	6	10.0517	0.5069
1	3	1	8.0841	0.0826
3	1	1	8.0841	0.0826
1	3	2	8.1463	0.1654
3	1	2	8.1463	0.1654
1	3	3	8.2490	0.2487
3	1	3	8.2490	0.2487
1	3	4	8.3906	0.3328
3	1	4	8.3906	0.3328
1	3	5	8.5693	0.4180
3	1	5	8.5693	0.4180
1	3	6	8.7827	0.5045
3	1	6	8.7827	0.5045
2	3	1	9.2666	0.1423
3	2	1	9.2666	0.1423
2	3	2	9.3571	0.2139
3	2	2	9.3571	0.2139
2	3	3	9.4823	0.2860
3	2	3	9.4823	0.2860
2	3	4	9.6410	0.3587
3	2	4	9.6410	0.3587
2	3	5	9.8314	0.4323
3	2	5	9.8314	0.4323
2	3	6	10.0517	0.5069
3	2	6	10.0517	0.5069
1	4	1	10.5292	0.0615
4	1	1	10.5292	0.0615
1	4	2	10.5772	0.1229

Cont. /

4	1	2	10.5772	0.1229
1	4	3	10.6567	0.1847
4	1	3	10.6567	0.1847
1	4	4	10.7669	0.2467
4	1	4	10.7669	0.2467
3	3	1	10.8336	0.0596
3	3	2	10.8802	0.1193
1	4	5	10.9070	0.3092
4	1	5	10.9070	0.3092
3	3	3	10.9575	0.1792
3	3	4	11.0648	0.2393
1	4	6	11.0759	0.3722
4	1	6	11.0759	0.3722
3	3	5	11.2012	0.2998
3	3	6	11.3657	0.3608
2	4	1	11.4180	0.0564
4	2	1	11.4180	0.0564
2	4	2	11.4622	0.1128
4	2	2	11.4622	0.1128
2	4	3	11.5356	0.1694
4	2	3	11.5356	0.1694
2	4	4	11.6376	0.2263
4	2	4	11.6376	0.2263
2	4	5	11.7675	0.2834
4	2	5	11.7675	0.2834
2	4	6	11.9242	0.3410
4	2	6	11.9242	0.3410

APPENDIX B

List of Publications

1. A. J. SANGSTER and K. I. SINCLAIR. Multi-mode degenerate mode cavity for hyperthermia treatment. *IEE Proc.-Microw. Antennas Propag.*, 153(1):75–82, 2006.

2. K. I. SINCLAIR, M. P. Y. DESMULLIEZ, and A. J. SANGSTER. A novel rf-curing technology for microelectronics and optoelectronics packaging. *1st Electronics System-integration Technology Conf. (ESTC)*, 2:1149–1157, Sep. 2006.

3. A. J. SANGSTER, K. I. SINCLAIR, and M. P. Y. DESMULLIEZ. Frequency agile microwave oven bonding system. UK Patent No. GB0711986.0, 2007.

4. T. TILFORD, K. I. SINCLAIR, C. BAILEY, M. P. Y. DESMULLIEZ, A. K. PARROTT and A. J. SANGSTER. Coupled FDTD-FVM simulation of microwave heating of polymer materials for micro-systems packaging applications. *Proceedings of Electronics Packaging Technology Conference, Singapore*, 2007.

5. K. I. SINCLAIR, M. P. Y. DESMULLIEZ, A. J. SANGSTER, G. GOUSETTIS, T. TILFORD, C. BAILEY, and A. K. PARROTT. Open-ended microwave oven for flip-chip assembly. *IEEE Proc. European Microwave Conference*, pp.620–623, Sep. 2007.

6. T. TILFORD, K. I. SINCLAIR, C. BAILEY, M. P. Y. DESMULLIEZ, A. K. PARROTT and A. J. SANGSTER. Multiphysics simulation of microwave curing of polymer materials in microelectronics Packaging Applications. *Proceedings 11th International Conference on Microwave and High Frequency Heating*, Oradea, Romania, pp.189-192, 2007.

7. T. TILFORD, K. I. SINCLAIR, C. BAILEY, M. P. Y. DESMULLIEZ, G. GOUSSETIS, A.K. PARROTT, and A. J. SANGSTER. Multiphysics simulation of microwave curing in micro-electronics packaging applications. *Journal of Soldering and Surface Mount Technology*, 19(3):26–33, 2007.

8. T. TILFORD, K. I. SINCLAIR, C. BAILEY, M. P. Y. DESMULLIEZ, A. K. PARROTT, A. J. SANGSTER. Coupled FDTD-FVM simulation of microwave heating of polymer materials for micro-systems packaging applications. *Proceedings 41st International Microwave Power Institute Symposium, Vancouver, Canada,* pp.7–12, 2007.

9. K. I. SINCLAIR, T. TILFORD, G. GOUSSETIS, C BAILEY, M. P. Y. DESMULLIEZ, A. K. PARROTT, and A. J. SANGSTER. Advanced microwave oven for rapid curing of encapsulant. *2nd Electronics Systemintegration Technology Conference*, pp.551–556, Jan. 2008.

10. A. J. SANGSTER, K. I. SINCLAIR, M. P. Y. DESMULLIEZ, and G. GOUSSETIS. Open-ended microwave oven for flip-chip assembly. *IET Microwave and Antennas Propag.*, 2(1):53–58, Feb. 2008.

11. K. I. SINCLAIR, T. TILFORD, M. P. Y. DESMULLIEZ, G. GOUSSETIS, C. BAILEY, A.K PARROTT, and A. J. SANGSTER. Open ended microwave oven for packaging. *Symposium on Design, Test, Integration and Packaging of MEMS / MOEMS, DTIP 2008, Nice, France*, pp.16–20, Apr. 2008.

12. T. TILFORD, C. BAILEY, A PARROTT, J. RIZVIL, C. YIN, K. I. SINCLAIR, and M. P. Y. DESMULLIEZ. Impact of assembly process technologies on electronic packaging materials. *Electronic Packaging Technology & High Density Packaging, 2008. ICEPT-HDP 2008. International Conference on*, pp.1–6, Jun 2008.

13. K. I. SINCLAIR, T. TILFORD, G. GOUSSETIS, C. BAILEY, M. P. Y. DESMULLIEZ, A. K. PARROTT and A. J. SANGSTER. Advanced microwave oven for rapid cure of encapsulants. *Proceedings ESTC 2008, Greenwich, London,* pp.551-556, Sept. 2008.

14. T. TILFORD, K. I. SINCLAIR, G. GOUSSETIS, C. BAILEY, M. P. Y. DESMULLIEZ, A. K. PARROTT and A. J. SANGSTER. Numerical analysis of thermal stresses induced during VFM encapsulant curing. *Proceedings International Spring Seminar on Electronics Technology, Budapest, Hungary*, pp.176–177, 2008.

15. K. I. SINCLAIR, G. GOUSSETIS, M. P. Y. DESMULLIEZ, A. J. SANGSTER, T. TILFORD, C. BAILEY and A. K. PARROTT. Polymer curing within an open-ended microwave oven. *European Microwave Week (Amsterdam)*, Oct. 2008.

16. T. TILFORD, K. I. SINCLAIR, G. GOUSSETIS, C. BAILEY, M. P. Y. DESMULLIEZ, A. K. PARROTT and A. J. SANGSTER. Comparison of encapsulant curing with convection and microwave systems. *33rd International Electronics Manufacturing Technology Conference, Penang, Malaysia*, 2008.

17. T. TILFORD, K. I. SINCLAIR, G. GOUSSETIS, C. BAILEY, M. P. Y. DESMULLIEZ, A. K. PARROTT and A. J. SANGSTER. Numerical simulation of encapsulant curing within a variable frequency microwave processing system. *Proc.*

International Conference on Thermal, Mechanical and Multi-Physics Simulation and Experiments in Micro-Electronics and Micro-systems, pp.447–454, 2008.

18. K. I. SINCLAIR, G. GOUSSETIS, M. P. Y. DESMULLIEZ, A. J. SANGSTER, T. TILFORD, C. BAILEY, and A. K. PARROTT. Optimization of an open-ended microwave oven for microelectronics packaging. *IEEE Trans. Microw. Theory and Techniq.*, 56(11):2635–2641, Nov. 2008.

19. K. I. SINCLAIR, A. J. SANGSTER, M. P. Y. DESMULLIEZ, and G. GOUSSETIS. Frequency agile microwave oven bonding system. UK Patent No. GB0819335.1, 2008.

20. K. I. SINCLAIR, T. TILFORD, M. P. Y. DESMULLIEZ, G. GOUSSETIS, C. BAILEY, A. K. PARROTT, and A. J. SANGSTER. Open ended microwave oven for packaging. *Journal of Design, Test, Integration and Packaging of MEMS / MOEMS*, Currently Under Review - Submitted July 2008.

References

[1] D. M. POZAR. *Microwave Engineering*, pages 314–319. John Wiley and Sons, Inc., 2nd edition edition, 1998.

[2] A. J. FENN. Focused microwaves fight cancer cells instead of missiles. *Electronic Design*, Feb. 2001.

[3] A. BOAG and Y. LEVIATAN. Optimal excitation of multi-applicator systems for deep regional hyperthermia. *IEEE Trans. Microw. Theory and Tech. Digest*, pages 307–310, 1998.

[4] A. J. FENN, A. Y. CHEUNG, and C. HONGREN. Adaptive focusing experiments for minimally invasive monopole phased arrays in hyperthermia treatment of breast cancer. *IEEE Conf. Engineering in Medicine and Biology Soc.*, 2:766–767, Nov. 1994.

[5] F. K. STORM. Hyperthermia. *IEEE Microw. Symp. Digest MTT-S*, 81(1):473–475, Jun. 1982.

[6] G. M. HAHN. Hyperthermia for the engineer: A short biological primer. *IEEE Trans. Biomedical Engineering*, BME-21(1):3–8, Jan. 1984.

[7] K. I. SINCLAIR, M. P. Y. DESMULLIEZ, and A. J. SANGSTER. A novel rf-curing technology for microelectronics and optoelectronics packaging. *1st Electronics System-integration Technology Conf. (ESTC)*, 2:1149–1157, Sep. 2006.

[8] WIKIPEDIA. http://en.wikipedia.org/wiki/waste_electrical_and_electronic_equipment_directive, Online Jan. 2009.

[9] WIKIPEDIA. http://www.rohs.gov.uk/, Online Jan. 2009.

[10] B. GEISLER, B. ADAMS, and I. AHMAD. Variable frequency microwave curing. *Advanced Packaging*, pages 17–19, 2002.

[11] A. A. A. DE SALLES. Biological effects of microwave and rf. *SBMO/IEEE MTT-S, APS and LEOS - IMOC '99*, 1:51–56, Aug. 1999.

[12] C. POLK and E. POSTOW. *Handbook of Biological Effects of Electromagnetic Fields*. CRC Press: Boca Raton, 2nd edition, 1995.

[13] H. MOSELEY. *Non-Ionising Radiation*, volume 18, pages 38–61.

[14] J. H. BERNHART. Non-ionising radiation safety: Radiofrequency radiation, electric and magnetic fields. *Physics on Medicine and Biology*, 37(4):807–844, 1992.

[15] L. J. GRANT. Practical aspects of non-ionising radiation protection. *The Hospital Physicists' Assoc. Leeds*, 1981.

[16] J. D. BRONZINO. *The Biomedical Engineering Handbook*. CRC Press and IEEE Press, 1st edition, 1995.

[17] J. C. LIN. Scientific literature on biological effects of radio frequency radiation: Criteria for evaluation. *IEEE Antennas and Propagation Magazine*, 44(2):140–142, 2002.

[18] AMERICAN NATIONAL STANDARDS INSTIUTUE (ANSI). Ieee c95.1-1991: Ieee standard for safety levels with respect to human exposure to radio frequency electromagnetic fields, 3khz to 300ghz.

[19] ICNIRP Guidelines. Guidelines for limiting exposure to time-varying electric, magnetic and electromagnetic fields (up to 300ghz). *International Commission on Non-Ionising Radiation Protection*, 74(4):494–522, 1988.

[20] C. C. JOHNSTON and A. W. GUY. Non-ionising electromagnetic wave effects in biological materials and systems. *Proc. IEEE*, 60(6):692–718, 1972.

[21] A. Y. CHUENG and D. W. KOOPMAN. Experimental development of simulated biomaterials for dosimetry studies of hazardous microwave radiation. *IEEE Trans. Microw. Theory and Techniq.*, MTT-24:669–673, Oct. 1976.

[22] P. LIU, C. M. RAPPAPORT, and S. SRIDHAR. Simulated biological materials at microwave frequencies for the study of electromagnetic hyperthermia. *IEEE Engineering in Medicine and Biology Society*, 1:272–273, 1992.

[23] G. HARTSGROVE, A KRASZEWSKI, and A. SUROWIEC. Simulated biological materials for electromagnetic radiation absorption studies. *Bioelectromagnetics*, 8(29-36), 1987.

[24] P. J. DIMBYLOW. Fine resolution and calculation of energy absorption in the human voxel model, norman. *Proc. 17th ACES Conference*, pages 109–119, 2001.

[25] P. GHANDI and J. Y. CHEN. Numerical dosimetry at power-line frequency using anatomically based models. *Bioelectromagnetic. J. Supp.*, 1(43-60), 1992.

[26] E. GJONAJ, M. BARTSCH, M. CLEMENS, S. SCHUPP, and T. WEILAND. High-resolution human anatomy models for advanced electromagnetic field computations. *IEEE Trans. on Magnetics*, 38(2), Mar. 2002.

[27] TECHNISCHE UNIVERSITAT DARMSTADT. http://www.temf.de/index.php?id=67&l=1, Online Nov. 2008.

[28] R. W. Y. HABASH. Simulation of heating in living biomass under microwave hyperthermia. *IEEE Int. Symp. on Electromagnetic Compatibility*, pages 919–923, Aug. 1999.

[29] A. GOURDENNE. Possible use of the microwave in polymer science. *Int. Conf. on Reactive Processings of Polymers Proc.*, pages 23–30, 1982.

[30] E. KARMAZSIN and P. SATRE. Use of continuous and pulsed microwave for quick polymerization of epoxy resins. *Thermochimica Acta*, 93:305–308, 1985.

[31] L. K. WILSON and J. P. SALERNO. Microwave curing of epoxy resins. *Technical Report*, AD-A067 732, Sep. 1978.

[32] N. S. STRAND. Fast microwave curing of thermoset part. *Modern Plastics*, 57(10):64–67, 1980.

[33] R. J. LAUF, D. W. BIBLE, A. C. JOHNSTON, and C. A. EVERLEIGH. 2 to 28 ghz broadband microwave heating system. *MIcrowave Journal*, pages 24–34, Nov. 1993.

[34] A. RAMANOORTHY and P. F. MEAD. Investigation of variable frequency microwaves for cure of flip chip underfills. *Proc. of InterPack '99: Pacific RIM/ASME Int. Intersociety Elec. Photonic Packaging Conf.*, 26(2):1569–1572, 1999.

[35] H. S. NOH, K. S. MOON, A. CANNON, P. J. HESKETH, and C. P. WONG. Wafer bonding using microwave heating of parylene intermediate layers. *Journal of Micromechanics and Microengineering*, 14:625–631, 2004.

[36] J. B. WEI, Z. FATHI, B. PAN, C. K. NAB, and S. L. CHAN. Use of microwave technology for rapid cure of chip-on-board glob top encapsulants. *IEEE Electronics Packaging Tech. Conf.*, pages 181–185, 2000.

[37] Y. J WANG, Y. FU, M. BECKER, and J. LIU. Microwave cure of metal-filled electrically conductive adhesive. *IEEE Electronic Components and Technology Conference*, pages 593–597, Jun. 2001.

[38] T. WANG, Y. FU, M. BECKER, and J. LIU. Heating and reliability characterstics of electrically conductive adhesives using variable frequency microwave cure. *IEEE Electronics Packaging Tech. Conf.*, pages 373–377, 2000.

[39] K. D. FARNSWORTH, R. N. MANEPALLI, S. A. BIDSTRUP-ALLEN, and P. A. KOHL. Variable frequency microwave curing of photosensitive polyimides. *IEEE Trans. Components and Packaging Technologies*, 24(3):474–481, Sep. 2001.

[40] R. V. TANIKELLA, S. A. BIDSTRUP-ALLEN, and P. A. KOHL. Novel low-temperature processing of polymer dielectrics on organic substrates by variable frequency microwave processing. *IEEE 8th Int. Symp. on Advanced Packaging Materials*, pages 254–259, 2002.

[41] R. V. TANIKELLA, T. SUNG, S. A. BIDSTRUP-ALLEN, and P. A. KOHL. Rapid curing of positive tone photosensitive polybenzoxazole based dielectric resin by variable frequency microwave processing. *IEEE Trans. on Components and Packaging Tech.*, 29(2):411–419, Jun. 2006.

[42] P. F. MEAD, A. RAMANOORTHY, S. PAL, Z. FATHI, and I. AHMAD. Variable frequency processing of underfill encapsulants for flip-chip applications. *Transactions of the ASME*, 125:302–307, Jun. 2003.

[43] S. LI and J. LIU. Development and characterisation of single mode microwave cured adhesives for electronics packaging application. *IEEE Electronic Components and Technology Conference*, pages 1147–1150, 2002.

[44] G. P. GLINSKI and C. BAILEY. Microwave cure of conductive adhesives for flip-chip & microsystems applications. *IEEE InterSociety Conf. on Thermal Phenomena*, pages 848–853, 2002.

[45] K. S. MOON, Y. LI, J. XU, and C. P. WONG. Lead-free interconnect by variable frequency microwave (vfm). *IEEE Elec. Components and Tech. Conf.*, pages 1989–1995, 2004.

[46] K. S. MOON, Y. LI, and C. P. WONG. A novel technique for lead-free soldering process using variable frequency microwave. *IEEE 9th Int. Symp. on Advanced Packaging Materials*, pages 118–125, 2004.

[47] LAMBDA TECHNOLOGIES. http://www.microcure.com/fr_21002.htm, Online Jul. 2007.

[48] H. S. NOH, K. S. MOON, A. CANNON, P. J. HESKETH, and C. P. WONG. Wafer bonding using microwave heating of parylene for mems packaging. *IEEE Electronics Packaging Tech. Conf.*, pages 924–930, 2004.

[49] L. LIU, S. YI, L. S. ONG, and K. S. CHIAN. Finite element analysis for microwave cure of underfill in flip chip packaging. *Thin Soild Film*, pages 436–445, 2004.

[50] L. LIU, S. YI, L. S. ONG, K. S. CHIAN, S. OSIYEMI, S. J. LIM, and F. SU. Chemothermal modeling and finite-element analysis for microwave cure process of underfill in flip-chip packaging. *IEEE Trans. Elec. Packaging Manuf.*, 28(4):355–363, 2005.

[51] S. YI, L. LIU, and S. K. PARK. Cure of underfills in flip chip using microwave. *IEEE Polytronic*, pages 92–98, 2004.

[52] F. FONTANA, E. BALEN, D. CASATI, K. HICKS, and I. AHMAD. Variable frequency microwave (vfm) curing of die attach and underfill materials. *EMPC European Medical Portal Conference*, pages 348–354, Jun. 2005.

[53] D. M. POZAR. *Microwave Engineering*, pages 9–10. John Wiley and Sons, Inc., 2nd edition, 1998.

[54] H. JIANG, K. S. MOON, Z. ZHANG, S. POTHUKUCHI, and C. P. WONG. Variable frequency microwave synthesis of sliver nanoparticles. *Journal of Nanoparticale Research*, 8:117–124, 2006.

[55] B. E. ERLANDSSON, H. TERIO, J. G. SJODIN, P. ASK, M. KARLSON, and D. LOYD. The risk of thermal injury during microwave treatment of the prostate analysed in model experiments and computer simulations. *IEEE-EMBC and CMBEC*, pages 1417–1418, 1995.

[56] A. BOAG and Y. LEVIATAN. Optimal excitation of multi-applicator systems for deep regional hyperthermia. *IEEE Trans. Biomedical Engineering*, 37(10):987–995, Oct. 1990.

[57] R. F. HARRINGTON. *Field Computation by Moment Methods*. New York: Macmillan, 1968.

[58] M. D. SAWYER and J. EDRICH. Non-invasive control of microwave hyperthermia by retro-focusing. *Biomedical Sciences Instrumentation*, 26:127–135, 1990.

[59] M. D. SAWYER, M. MARIETTA, and J. EDRICH. Microwave hyperthermia using retro-focusing. *Antennas and Propagation Society International Symposium*, pages 1224–1227, 1990.

[60] C. M. RAPPAPORT and J. G. PEREIRA. Optimal microwave source distributions for heating off-centre tumours in spheres of high water content tissue. *IEEE Trans. Microw. Theory and Techniq.*, MTT-40(10):1979–1982, Oct. 1992.

[61] A. J. FENN and G. A. KING. Experimental investigation of an adaptive feedback algorythm for hot spot reduction. *IEEE Trans. Biomedical Engineering*, 43(3):273–280, Mar. 1996.

[62] D. DUNN, C. M. RAPPAPORT, and A. J. TERZUOLI JR. Fdtd verification of deep-set brain tumour hyperthermia using a spherical microwave source distribution. *IEEE Trans. Microw. Theory and Techniq.*, MTT-44(10):1769–1777, Oct. 1996.

[63] S. JACOBSON and P. R. STAUFFER. Multifrequency radiometric determination of temperature profiles in a lossy homogenous phantom using dual-mode antenna with integral water bolus. *IEEE Trans. Microw. Theory and Techniq.*, MTT-50(7):1737–1746, Jul. 2002.

[64] M. E. KOWALSKI and J. M. JIN. Determination of electromagnetic phased-array driving signals for hyperthermia based on a steady-state temperature criterion. *IEEE Trans. Microw. Theory and Techniq.*, MTT-48(11):1864–1873, Nov. 2000.

[65] M. E. KOWALSKI and J. M. JIN. A temperature-based feedback control system for electromagnetic phased-array hyperthermia: Theory and simulation. *Physics in Medicine and Biology*, 48:633–651, 2003.

[66] J. LOANE, H. LING, and S. W. LEE. Experimental investigation of a retro-focusing microwave hyperthermia applicator: Conjugate-field matching scheme. *IEEE Trans. Microw. Theory and Techniq.*, MTT-34:490–494, May 1986.

[67] D. DESPRETZ, J. C. CAMART, MICHEL C., J. J. FABRE, B. PREVOST, J. P SOZANSKI, and M. CHIVE. Microwave prostate hyperthermia: Interest of urethral and rectal applicators combination – theoretical study and animal experimental results. *IEEE Trans. Microw. Theory and Techniq.*, MTT-44(10):1762–1768, Oct. 1996.

[68] J. C. LIN, S. HIRIA, C. L. CHIANG, W. L. HSU, J. L. SU, and Y. J WANG. Computer simulation and experimental studies of sar distributions of interstitial arrays of sleeved-slot microwave antennas for hyperthermia treatment of brain tumours. *IEEE Trans. Microw. Theory and Techniq.*, MTT-48(11):2191–2198, Nov. 2000.

[69] J. ERB, R. ENGELBRECHT, and G. SCHALLER. Em field simulation of minimal invasive mw antenna for thermal therapy. *Proc. 22nd Annual EMBS Int. Conf.*, pages 288–291, Jul. 2000.

[70] Y. NIKAWA, T. KATSUMATA, M. KIKUCHI, and S. MORI. An electric field converging applicator with heating pattern controller for microwave hyperthermia. *IEEE Trans. Microw. Theory and Techniq.*, MTT-34(5):631–635, May 1986.

[71] H. R. UNDERWOOD, A. F. PETERSON, and R. L. MAGIN. Electric-field distribution near rectangular microstrip radiators for hyperthermia heating: Theory versus experiment in water. *IEEE Trans. Biomedical Engineering*, 39(2):146–153, Feb. 1992.

[72] M. KRAIRIKSH, T. WAKABAYASHI, and W. KIRANON. A spherical slot array applicator for medical application. *IEEE Trans. Microw. Theory and Techniq.*, MTT-43(1):78–86, Jul. 2000.

[73] R. V. SABARIEGO, L. LANDESA, and F. OBELLERIO. Synthesis of an array antenna for hyperthemria applications. *IEEE Trans. on Magnetics*, 36(4):1696–1699, Jul. 2000.

[74] Y. KANAI, T. TSUKAMOTO, K. TOYAMA, Y. SAITOH, M. MIYAKAWA, and T KASHIWA. Analysis of a hyperthermia treatment in a re-entrant resonant cavity applicator by solving time-dependent electromagnetic-heat transfer equations. *IEEE Trans. on Magnetics*, 37(3):1661–1664, May 1996.

[75] LAMBDA TECHNOLOGIES. http://www.bsdmc.com/, Online Nov. 2008.

[76] LAMBDA TECHNOLOGIES. http://www.bsdmc.com/bsd2000_3d.htm, Online Nov. 2008.

[77] LAMBDA TECHNOLOGIES. http://www.bsdmc.com/bsd-2000_3d_mr.htm, Online Nov. 2008.

[78] CELSION. http://www.celsion.com/, Online Feb. 2003.

[79] CELSION. http://www.celsion.com/breastcancertrials.htm, Online Feb. 2003.

[80] A. J. FENN, J. MON, and D. SMITH. Monopole phased array thermotherapy applicator for deep tumor therapy. *US Patent*, (US 2004 / 0044385 A1), Mar. 2004.

[81] Epoxy resins and composites. *Advanced Polymer Science*, pages 72–75, 1985.

[82] J. JOW, M. FINZEL, J. ASMUSSEN, and M. C. HAWLEY. Dielectric and temperature measurements during microwave curing of epoxy in a sweeping resonant cavity. *IEEE MTT-S Digest*, pages 456–468, 1987.

[83] J. W. LANE and J. C. SAFERIS. Dielectric modelling of the curing process. *Polymer Engineering and Science*, 26:346–353, 1986.

[84] D. KRANBUEHL, S. DELOS, E. YI, J. MAYER, and T. JARVIE. Dynamic dielectric analysis: Nondestructive material evaluation and cure cycle monitoring. *Polymer Engineering and Science*, 26:338–345, 1986.

[85] N. F. SHEPPARD and D. SENTURIA. Chemical interpretation of the relaxed permittivity during epoxy resin cure. *Polymer Engineering and Science*, 26:354–357, 1986.

[86] D. DAY. Effects of stoichiometric mixing ratio on epoxy cure-dielectric analysis. *Polymer Engineering and Science*, 26:362–366, 1986.

[87] W. LEE and S. SPRINGER. Interaction of electromagnetic radiation with organic matrix composites. *Journal of Composite Materials*, 18:357–386, 1984.

[88] J. BAKER-JARVIS. Dielectric and magnetic measurement methods in transmission lines: An overview. Technical report, AMTA Workshop, 1992.

[89] L. LIGHTHART. A fast computational technique for accurate permittivity determination using transmission line methods. *IEEE Trans. Microw. Theory and Techniq.*, 31:249–254, 1983.

[90] C. J. REDDY, M. D. DESHPANDE, and G.A. HANIDU. Learning tool for estimation of complex permittivity of dielectric material. *Frontiers in Education Conference*, 3(1195-1196), Nov. 1996.

[91] E. A. ELKHAZMI, M. N. ZAINAL ABIDIN, and N. J. McEWAN. Complex permittivity measurements of moulding plastic using hybrid time and frequency methods. *High Frequency Postgraduate Student Colloquium*, 1997.

[92] W. B. WESTPHAL. *Dielectric measuring technique*, pages 63–122. John Wiley and Sons, Inc., 1954.

[93] N. N. HOANG, H. RMILI, A. MOUHSEN, J. L. WOJKIEWICZ, and J. L. MIANE. Nondestructive complex permittivity measurement of conducting materials using open-ended coaxial probes. *Communications and Electronics*, pages 486–489, Oct. 2006.

[94] J. KRUPKA, D. KRZYSZTOF, A. ABRAMOWICZ, M. TOBAR, and R. GEYER. Complex permittivity measurements of extremely low loss dielectric materials using whispering gallery modes. *IEEE Trans. Microw. Theory and Tech. Digest*, 3:1347–1350, 1997.

[95] J. MAZIERSKA, J. KRUPKA, V. MOHAM, and D. LEDENYOV. Complex permittivity measurements at variable temperatures of low loss dielectric substrates employing split post and single post dielectric resonators. *IEEE Trans. Microw. Theory and Tech. Digest*, 3:1825–1828, 2004.

[96] B. G. COLPITTS. Temperature sensitivity of coaxial probe complex permittivity measurements: Experimental approach. *IEEE Trans. Microw. Theory and Techniq.*, 41(2):229–233, 1993.

[97] E. MARAND, K. R. BAKER, and J. D. GRAYBEAL. Comparison of reaction mechanisms of epoxy resins undergoing thermal and microwave cure from in situ measurements of microwave dielectric properties and infrared spectroscopy. *Macromolecules*, 25:2243–2252, 1992.

[98] J. C. MAXWELL. *A Treatise on Electricity and Magnetism*. Dover, 1954.

[99] O. HEAVISIDE. *Electromagnetic Theory*. London: Benn, 1893.

[100] J. J. THOMPSON. *Notes on Recent Researches in Electricity and Magnetism*, pages 344–347. Oxford: Clarendon, 1893.

[101] J. LARMOR. Electric vibrations in condensing systems. *Proc. London Math. Soc*, 26:119, 1894.

[102] LORD RAYLEIGH. On the passage of electric waves through tubes or the vibrations of dielectric cylinders. *Phil. Mag.*, XLIII:125–132, 1897.

[103] K. S. PACKARD. The origin of waveguides: A case of multiple rediscovery. *IEEE Trans. Microw. Theory and Techniq.*, MTT-32:961–969, Sep. 1984.

[104] D. M. POZAR. *Microwave Engineering*, page 104. John Wiley and Sons, Inc., 2nd edition, 1998.

[105] R. E. COLLIN. *Field Theory of Guided Waves*, page 4. The IEEE Press Series on Electromagnetic Wave Theory, 2nd edition, 1991.

[106] D. M. POZAR. *Microwave Engineering*, page 6. John Wiley and Sons, Inc., 2nd edition, 1998.

[107] D. M. POZAR. *Microwave Engineering*, page 106. John Wiley and Sons, Inc., 2nd edition, 1998.

[108] WIKIPEDIA. http://en.wikipedia.org/wiki/helmholtz_equation, Online Nov. 2008.

[109] J. D. KRAUS. *Electromagnetics*, page 671. McGraw-Hill, 4th edition.

[110] D. M. POZAR. *Microwave Engineering*, pages 120–130. John Wiley and Sons, Inc., 2nd edition, 1998.

[111] D. M. POZAR. *Microwave Engineering*, chapter 3. John Wiley and Sons, Inc., 2nd edition, 1998.

[112] R. E. COLLIN. *Field Theory of Guided Waves*, chapter 5. Wiley Interscience, 2nd edition, 1991.

[113] J. D. KRAUS. *Electromagnetics*, chapter 14. McGraw-Hill, 4th edition.

[114] D. A. OLVER. *Microwave and Optical Transmission*, chapter 10. Wiley, international student edition, 1992.

[115] D. M. POZAR. *Microwave Engineering*, pages 300–303. John Wiley and Sons, Inc., 2nd edition, 1998.

[116] D. M. POZAR. *Microwave Engineering*, pages 132–141. John Wiley and Sons, Inc., 2nd edition, 1998.

[117] R. E. COLLIN. *Field Theory of Guided Waves*, pages 400–402. The IEEE Press Series on Electromagnetic Wave Theory, 2nd edition, 1991.

[118] D. M. POZAR. *Microwave Engineering*, pages 374–379. John Wiley and Sons, Inc., 2nd edition, 1998.

[119] D. M. POZAR. *Microwave Engineering*, pages 340–346. John Wiley and Sons, Inc., 2nd edition, 1998.

[120] A. J. SANGSTER and K. I. SINCLAIR. Multi-mode degenerate mode cavity for hyperthermia treatment. *IEE Proc.-Microw. Antennas Propag.*, 153(1):75–82, 2006.

[121] A. J. SANGSTER, K. I. SINCLAIR, M. P. Y. DESMULLIEZ, and G. GOUSSETIS. Open-ended microwave oven for flip-chip assembly. *IET Microwave and Antennas Propag.*, 2(1):53–58, Feb. 2008.

[122] J. K. PLOURDE and C. L. REN. Application of dielectric resonators in microwave components. *IEEE Trans. Microw. Theory and Techniq.*, MTT-29(8):754–770, 1981.

[123] T. TILFORD, K. I. SINCLAIR, C. BAILEY, M. P. Y. DESMULLIEZ, G. GOUSSETIS, A.K. PARROTT, and A. J. SANGSTER. Multiphysics simulation of microwave curing in micro-electronics packaging applications. *Journal of Soldering and Surface Mount Technology*, 19(3):26–33, 2007.

[124] R. G. CARTER. *Electromagnetic Waves*, chapter 2. Chapman and Hall, 1990.

[125] R. E. COLLIN. *Field Theory of Guided Waves*, chapter 3. Wiley Interscience, 1991.

[126] K. I. SINCLAIR, M. P. Y. DESMULLIEZ, A. J. SANGSTER, G. GOUSETTIS, T. TILFORD, C. BAILEY, and A. K. PARROTT. Open-ended microwave oven for flip-chip assembly. *IEEE Proc. European Microwave Conference*, pages 620–623, Sep. 2007.

[127] K. I. SINCLAIR, G. GOUSSETIS, M. P. Y. DESMULLIEZ, A. J. SANGSTER, T. TILFORD, C. BAILEY, and A.K PARROTT. Optimization of an open-ended microwave oven for microelectronics packaging. *IEEE Trans. Microw. Theory and Techniq.*, 56(11):2635–2641, Nov. 2008.

[128] D. M. POZAR. *Microwave Engineering*, page 205. John Wiley and Sons, Inc., 2nd edition, 1998.

[129] D. M. POZAR. *Microwave Engineering*, pages 149–150. John Wiley and Sons, Inc., 3rd edition, 2005.

[130] NATIONAL INSTRUMENTS. http://www.ni.com/labview/, Dec. 2008.

[131] K. I. SINCLAIR, T. TILFORD, M. P. Y. DESMULLIEZ, G. GOUSSETIS, C. BAILEY, A.K PARROTT, and A. J. SANGSTER. Open ended microwave

oven for packaging. *Symposium on Design, Test, Integration and Packaging of MEMS/MOEMS, DTIP 2008, Nice, France*, pages 16–20, 2008.

[132] LAMBDA TECHNOLOGIES. Flip chip underfill cure. Technical Report MC98-201, Lambda Technologies.

[133] AGILENT TECHNOLOGIES. 85070e dielectric probe kit (200 mhz to 50 ghz). Technical report, AGILENT TECHNOLOGIES, 2008.

[134] A. J. SANGSTER, K. I. SINCLAIR, and M. P. Y. DESMULLIEZ. Frequency agile microwave oven bonding system. UK Patent No. GB0711986.0, 2007.

[135] K. I. SINCLAIR, A. J. SANGSTER, M. P. Y. DESMULLIEZ, and G. GOUSSETIS. Frequency agile microwave oven bonding system. UK Patent No. GB0819335.1, 2008.